A Dissertation Submitted for a Doctorate in Materials Science

Plasmonic Nanoengineering in Hollow Metal Nanostructures: An Electron Energy-Loss Spectroscopy Study

Aziz Genç

Supervisor: Prof. Jordi Arbiol i Cobos

Tutor: Dr. Xavier Granados i García

Universitat Autònoma de Barcelona
Department of Physics, Faculty of Sciences

Institut de Ciència de Materials de Barcelona (ICMAB-CSIC)
Institut Català de Nanociència i Nanotecnologia (ICN2)

July 2015

Chapter 5

Three-Dimensional Plasmonic Properties of Complex AuAg Nanostructures

5.1 Introduction

In this chapter, we present some angle resolved EELS experiments conducted on several cuboid AuAg nanostructures corresponding to the early stages of the galvanic replacement reaction [69]. As there were many uncertain issues about the three-dimensional (3D) morphology of the hollow AuAg nanostructures presented in the Chapter 3, which are effecting the local plasmonic properties dramatically, we have decided to proceed with 3D plasmonic analyses of similar AuAg nanostructures. There have been several studies showing the power of STEM-EELS technique for 3D characterization of different materials [90, 244–247, 265, 266]. Most of these studies about EELS tomography have dealt with the core-loss signals. On the other hand, 3D plasmon-field tomography has been shown theoretically by Hörl et al. [267]. More recently, Nicoletti et al. [90] reported the 3D EELS mapping of localized surface plasmon resonances of a 100 nm Ag nanocube. With these studies paving the way to the 3D characterization of LSPRs in solid metal nanostructures, we have decided to apply the technique to hollow metal nanostructures and coupling between two nanostructures. In our case, the difficulty falls on the size of the nanostructures (∼50 nm) and their complex morphology (hollow structures with inner walls and holes). Previous works presented in literature studied solid nanostructures which had perfectly defined symmetrical shapes and sizes about or larger than 100 nm.

We have obtained low-loss EELS maps of several AuAg nanostructures (Fig. 5.1) with high tilt angles ($\sim \pm 60^o$, which may differ from sample to sample). Fig. 5.1 shows $+40^o$, 0^o, -40^o tilted HAADF STEM micrographs of a 68 nm solid Ag@Au core-shell nanocube, a 50 nm partially hollow AgAu nanocube, a 47 nm AuAg nanoframe, two Ag@Au core-shell nanocubes with sizes of 59 nm and 53 nm standing with ∼22 nm separation and a 63 nm Ag@Au core-shell nanocube and a 53 AuAg nanoframe standing with ∼14 nm separation. 3D plasmonic properties of these nanostructures are presented in the following. The samples are deposited on 18 nm thick SiO_2 grids as it was not possible to tilt higher than $\pm 45^o$ by using 15 nm thick Si_3N_4 grids due to shadowing of the e-beam. Although they are slightly thinner than the SiO_2 grids, Si_3N_4 grids have 9 independent 0.1 mm x 0.1 mm windows and they are not suitable for high tilt tomography. On the other hand, SiO_2 grids have a 0.5 mm x 0.5 mm single window, allowing us to tilt $\pm 60^o$. The EELS SI maps are obtained by using a monochromated STEM operated at 80 kV with typical energy resolutions around 120 meV and spatial resolution between 1.2 and 2.0 nm. Due to high number of tilt series and, more importanty, e-beam induced transformation of the nanostructure morphologies after long aquisition times (which are modaretaly visible at the -40^o tilted HAADF STEM micrographs of Fig. 5.1), we had to optimize the acquisition times to about 5 min per EELS maps. The signal-to-noise ratios of the obtained EELS data are somewhat lower than those presented in previous chapters for 2D experiments, yet they contain the necessary information to generate components related to different LSPR modes for each tilt angle. We have used spectral unmixing with vertex component analysis (VCA) to process the EELS data, where we have identified individual components from different tilt angles and used the obtained spectra of the components to generate corresponding abundance maps, similar to the Ref. [90]. We have obtained 5 different tomography sets but tomography reconstructions of all datasets and relevant modelling studies are in progress and will be completed in the near future, due to the complexity of the processing routines and time limitations for my PhD studies.

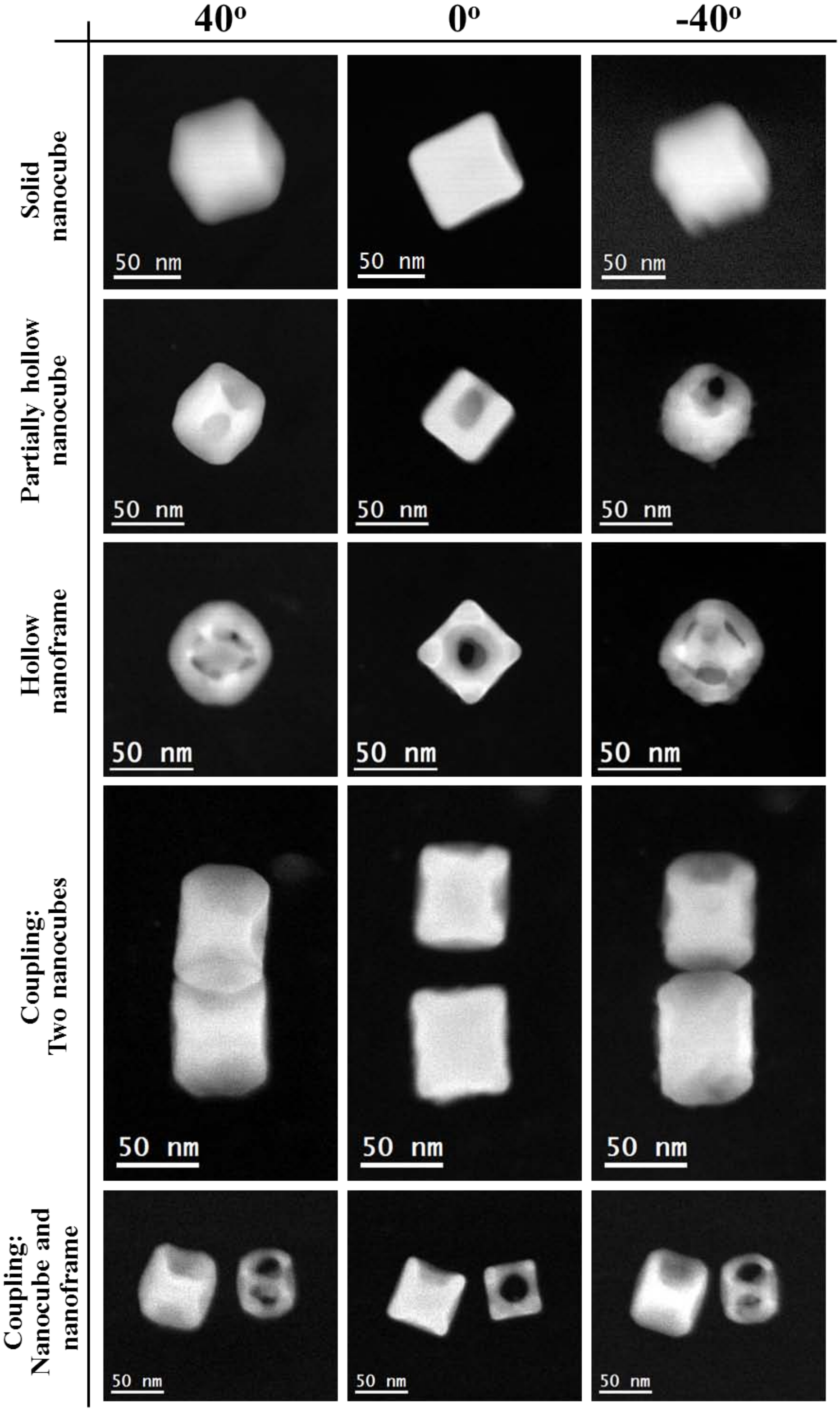

FIGURE 5.1: HAADF STEM micrographs of different AuAg nanostructures that 3D EELS maps are obtained: +40^o, 0^o, -40^o tilts of a solid Ag@Au core-shell nanocube, a partially hollow AuAg nanocube, an AuAg nanoframe, two Ag@Au core-shell nanocubes standing with ~ 22 nm separation and an Ag@Au core-shell nanocube and an AuAg nanoframe standing with ~ 14 nm separation.

5.2 Ag@Au core-shell nanocube

5.2.1 Structural characterization

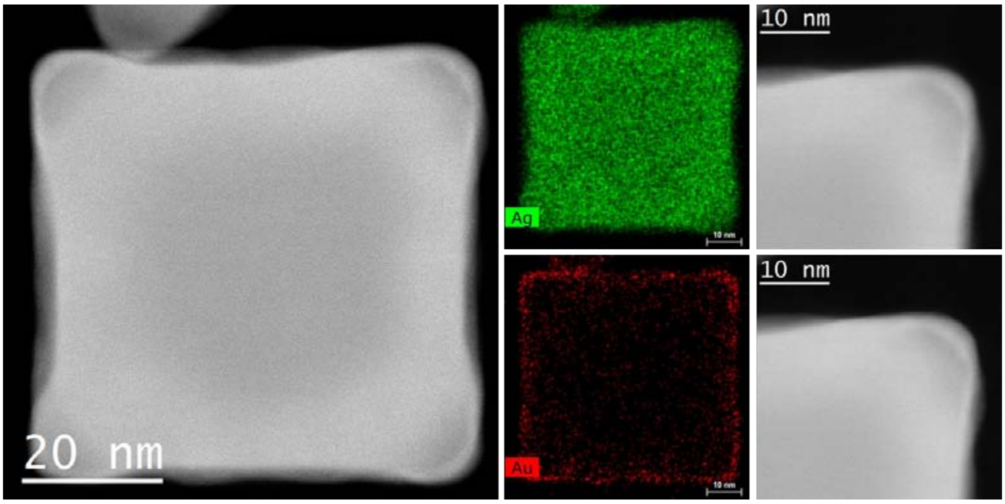

FIGURE 5.2: High resolution HAADF STEM micrograph of a 63 nm Ag@Au core-shell nanocube. STEM-EDX maps of Ag (in green) and Au (in red). Detail of the upper right corner with two different focus revealing the shell in different focus.

Fig. 5.2 shows high resolution HAADF STEM micrograph of a 63 nm Ag@au core-shell nanocube. This nanocube is not the same where we have obtained 3D EELS maps but it is essentially similar in terms of size and morphology. We could not perform all the characterization studies of STEM-EELS, HR-STEM, and STEM-EDX on the same nanostructures due to the e-beam induced morphological changes during STEM-EELS and/or STEM-EDX measurements. Therefore, we had to choose different yet similar nanostructures for HR-STEM and STEM-EDX studies. HR-STEM reveals the presence of several nanometer thick, inhomogeneously distributed shell with a darker contrast around the nanocube and elemental STEM-EDX maps confirm that the shell is rich in Au compared to the other parts of the nanocube. Thus, we name this nanostructures as Ag@Au core-shell nanocubes. Quantification of the STEM-EDX revealed that the center of the nanocube has a composition of 93±0.5 at.% Ag and 7±0.5 at.% Au, whereas the edges are comprised 61.75±1.45 at.% Ag and 38.25±1.45 at.% Au. The corners have a higher Au content of 49±2.8 at.%, which can be interpreted from the elemental distribution map of Au (in red) where the corners have brighter red contrast. Such an inhomogeneous distribution can also be revealed by the detailed HR-STEM micrographs of the upper right corner presented on the right of the figure. It has been observed that the several atomic layers around the corners have slightly different focus than the rest of the nanocube, which may be due to the freshly deposited Au during the galvanic replacement reaction that did not form an alloy. Lu et al. [306] reported similar segregation behavior in the case of Pt deposition on Pd nanocubes which takes place when the deposition rate is higher than the diffusion rate.

5.2.2 Angle-resolved local plasmonic properties

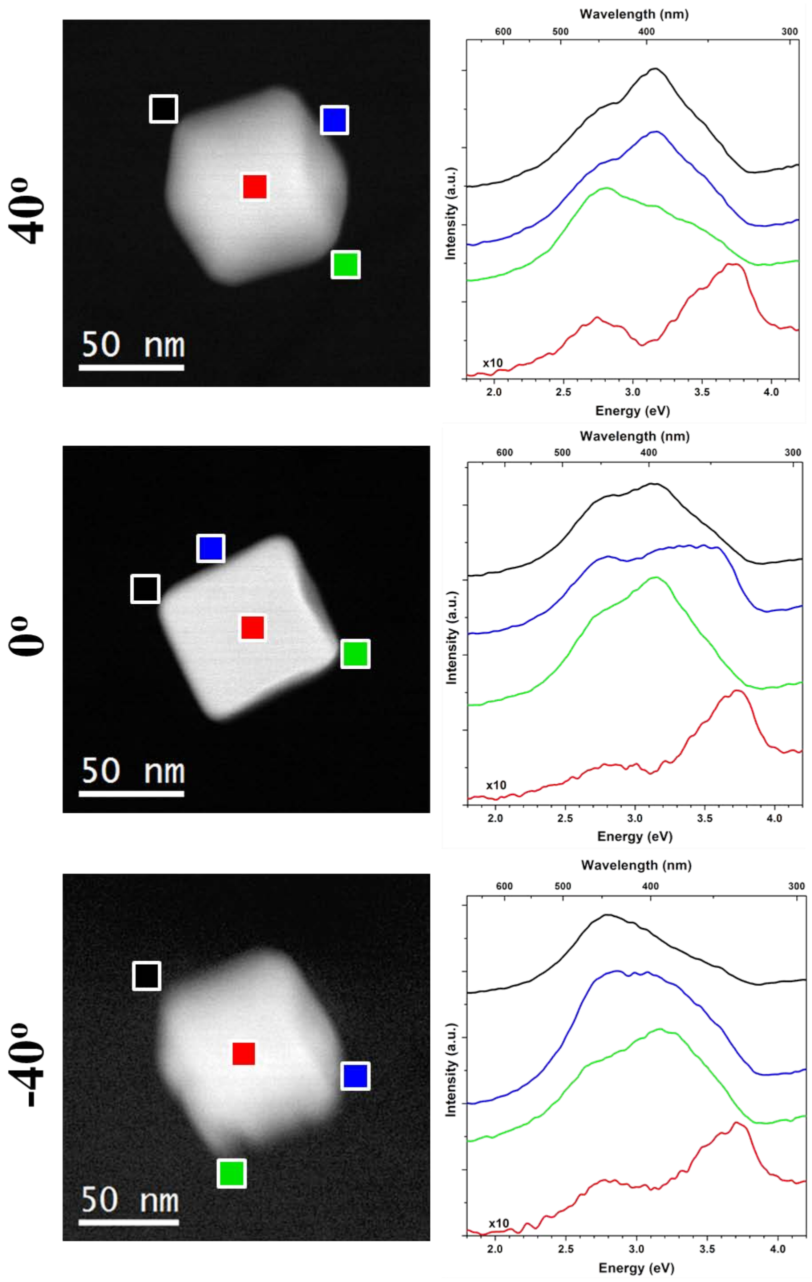

Figure 5.3: HAADF STEM micrographs (left) of the +40^o, 0^o, -40^o tilts of a solid Ag@Au core-shell nanocube and background subtracted local EEL spectra (right) of different locations shown by black, blue, green and red squares. Note that the color of each spectra corresponds to the color of the location indicated in the HAADF STEM micrographs.

Having reported the structural characteristics of the studied core-shell nanocubes, we continue with their 3D plasmonic properties. Fig. 5.3 shows HAADF STEM micrographs obtained from +40^o, 0^o, -40^o tilted 68 nm solid Ag@Au core-shell nanocube and background subtracted local EEL spectra of the different locations such as corners, edges and bulk of the nanocube. The color of each EEL spectra correspond to the color of the selected area in the HAADF STEM micrographs. As mentioned earlier, we have obtained EELS SI in a relatively shorter time and, therefore the signal-to-noise ratio of the data is not as high as the above presented EELS datasets. We have choosen a larger area of 10 pixel x 10 pixel, which was 5 pixel by 5 pixel for the above presented EELS maps, to extract the local EEL spectra from each location. A LSPR peak at around 2.7 eV is observed in the selected area EEL spectra from the corners and edges suggesting that this LSPR mode can be present around the nanocube. Main LSPR peaks from the corners are located ~3.2 eV with slight variations from corner to corner. The selected area EEL spectra from the edges revealed the presence of wide peaks which may contain several LSPR modes including the one located at ~3.6 eV corresponding to the main edge/face mode of the Ag nanocubes. Selected area EEL spectra from the center of the nanocube revealed the presence of bulk plasmon mode of Ag located at ~3.8 eV, where the EELS signals are multiplied by 10 in order to have a better comparison with the other EEL spectra.

It will be revealed unambigously when the tomography reconstructions are completed but one can see the effects of the substrate on the local EEL spectra presented in Fig. 5.3. The local EEL spectra obtained from the corners at 0^o tilt (black and green areas) contain contributions from the proximal and distal modes and look quite similar to one another. When we check the local plasmon response at the corners at +40^o tilt, we see that the EEL spectra of the upper left corner (black) is different than the one of the lower right corner (green). As it is discussed in the previous chapter, the presence of the substrate splits the LSPR modes into proximal (in contact with the substrate) and distal (not in contact with the substrate) modes where the proximal modes have lower energies than their distal counterparts [90, 91]. Keeping this in mind, we can suggest that the lower right corner (green) with a dominant plasmon peak located at ~2.8 eV is in contact with the substrate and this mode is the proximal corner plasmon mode of the core-shell nanocube. Similarly, the upper left corner (black) with a dominant plasmon peak located at ~3.2 eV is not in contact with the substrate and contains the distal corner plasmon mode. This can be confirmed by looking at the local EEL spectra obtained from the -40^o tilt where the upper corner (black) is in contact with the substrate and contains the proximal corner plasmon mode with a dominant peak located at ~2.8 eV. The lower part of the HAADF STEM micrograph is not in contact with the substrate and the local EEL spectra from the green area contains the distal corner plasmon mode at ∼3.2 eV.

5.2.3 Processing of 3D plasmonic properties

Fig. 5.4 shows the HAADF STEM micrographs obtained simultaneously with the EELS SI at different tilt angles between +55^o and -60^o with different intervals. It was possible to tilt up to ±60^o by using the SiO_2 grids with a 0.5 mm x 0.5 mm window. Notice that the tilt degrees can be limited depending on the location of the nanocubes on the grid. We have tried to use lower tilt intervals at higher degrees in order to minimize the so called "missing wedge" [261]. It should be noted here that the sample stability was quite poor at higher tilt angles in both directions in terms of sample drift and e-beam induced "charging" effects, as observed in the HAADF STEM micrographs obtained at +50 and +55 degrees (Fig. 5.4). Even though we obtained the maps at low acquisition time (few minutes), some of the measurements resulted in distortion and damaging of the cubic morphology. We started to obtain EELS maps from the maximum positive (+55) degrees and decreased the tilt until the maximum negative (-60) degrees. As the nanocube is exposed to higher dose of e-beam exposure after certain number of EELS maps obtained at different tilts, e-beam induced morphological changes and nanostructure degradation started to appear as it is clearly visible in the HAADF STEM micrographs between -40 and -60 degrees.

After presenting the structural poperties of the core-shell Ag@Au nanocubes and angle-resolved local plasmonic properties for selected angles, we will continue with the processing of 3D plasmonic properties by means of VCA. In Fig. 5.5, 4 different components obtained by VCA analysis and their corresponding abundance maps for selected tilt angles (+55, +40, +20, 0, -20, -40 and -60 degrees) are presented. Component I has a relatively wide plasmon peak located at ∼2.8 eV with a shoulder at ∼2.7 eV. Its corresponding abundance map at 0^o tilt suggests that this mode has been generated from almost all around the nanocube where the corners have slightly higher intensities compared to edges. It is possible that it is a plasmon mode related to the proximal corner modes, as discussed above in Fig. 5.3, with some contributions from the Au-rich AuAg shell. As seen in this figure, the intensity of this plasmon mode decrease substantially for the higher tilt angles. Since Fig. 5.5 shows a selection of 7 tilt angles among a total of 15, we think it is convenient to present plasmon maps of each mode for all the tilt angle in separate figures for the integrity of the present thesis manuscript. Figures 5.6, 5.7, 5.8 and 5.9 shows the spectra of the components I, II, III and IV in Fig. 5.5, respectively, along with their corresponding abundance maps for each tilt angles. The components II and III are located at ∼3.0 eV and ∼3.2 eV, respectively. Their abundance maps reveals

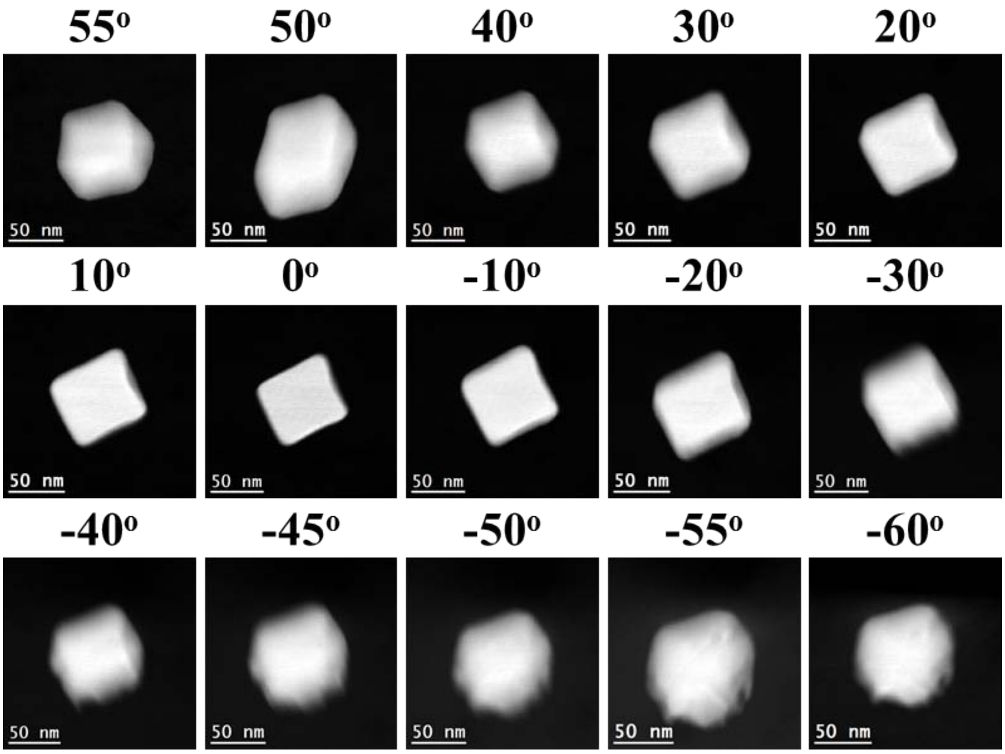

FIGURE 5.4: Series of HAADF STEM micrographs of the Ag@Au core-shell nanocube obtained simultaneously with the EELS SI at different tilt angles between +55^o and -60^o with different intervals.

that both are corner plasmon modes and have quite similar distributions for different tilt angles. As discussed above in Fig. 5.3, these modes are distal corner modes corresponding to Ag related plasmon resonances. These 3 different corner modes are in good aggrement with the literature [90]. Similarly, the presence of multiple corner modes in Ag nanocubes is shown in the previous chapter on the BEM simulations (Fig. 3.11). Component IV is the well-known face plasmon mode of Ag nanocubes and located at ∼3.6 eV. Its corresponding abundance maps clearly reveal the presence of this mode at the faces of the core-shell nanocube at tilt angles between ±40^o, whereas its intensity is decreased drastically for higher tilt angles. As a future work, we will complete the 3D recontruction for all 4 localized surface plasmon resonance modes shown in this section and it will be possible to visualize these corner and edge plasmon modes more clearly in 3D.

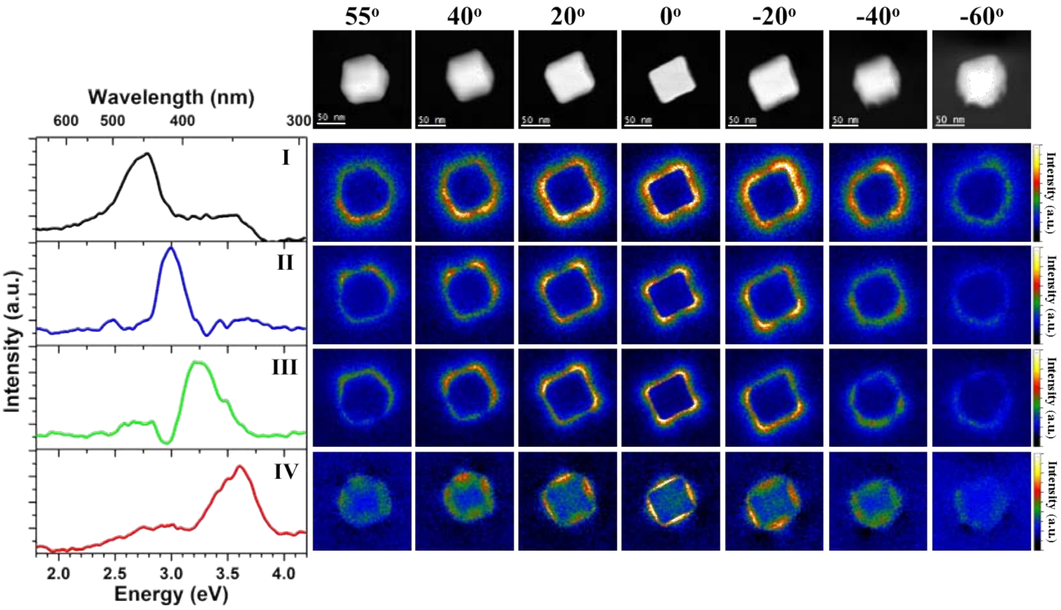

FIGURE 5.5: Spectra corresponding to 4 different components obtained by VCA and their corresponding abundance maps for different tilts. Intensity of the abundance maps are normalized within each component.

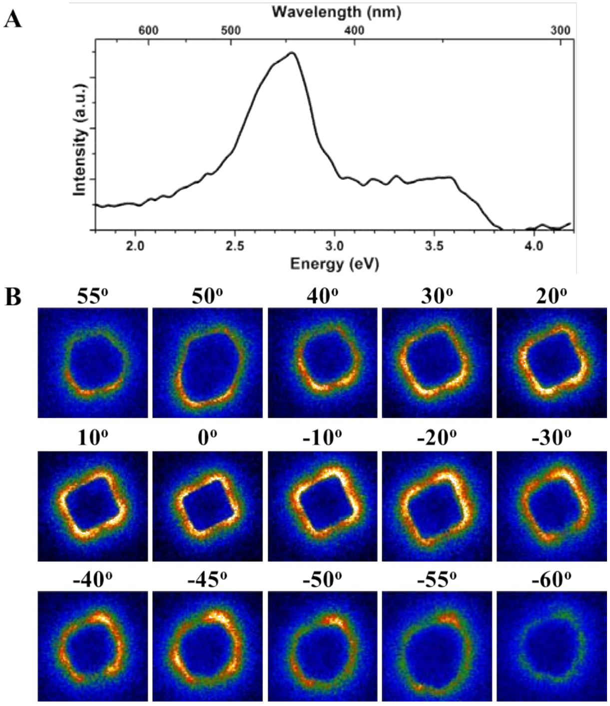

FIGURE 5.6: A. Spectrum of the component I in Fig. 5.5 and its corresponding abundance maps for all tilt angles are shown in B.

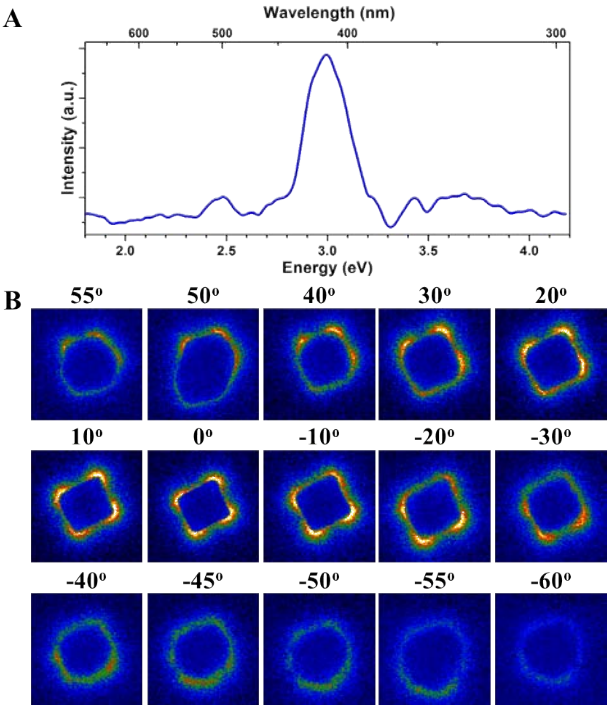

FIGURE 5.7: A. Spectrum of the component II in Fig. 5.5 and its corresponding abundance maps for all tilt angles are shown in B.

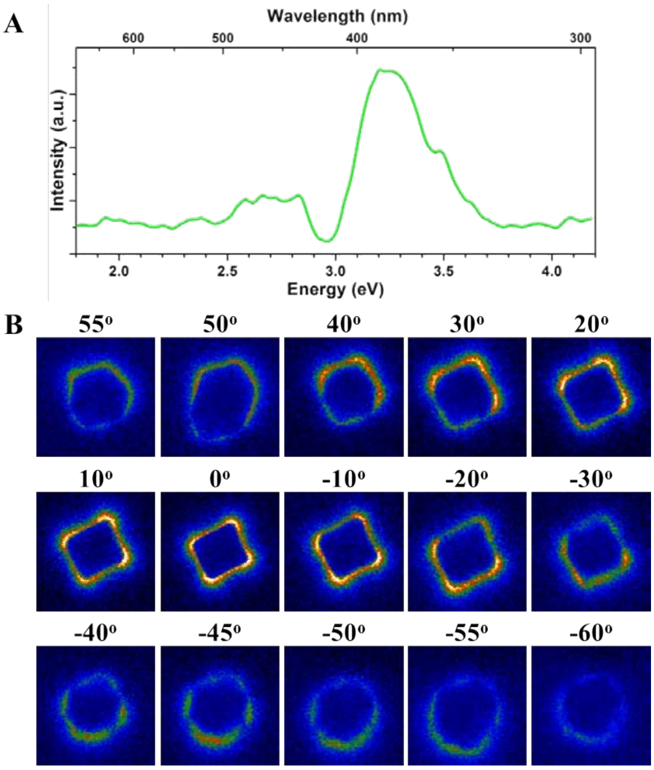

FIGURE 5.8: A. Spectrum of the component III in Fig. 5.5 and its corresponding abundance maps for all tilt angles are shown in B.

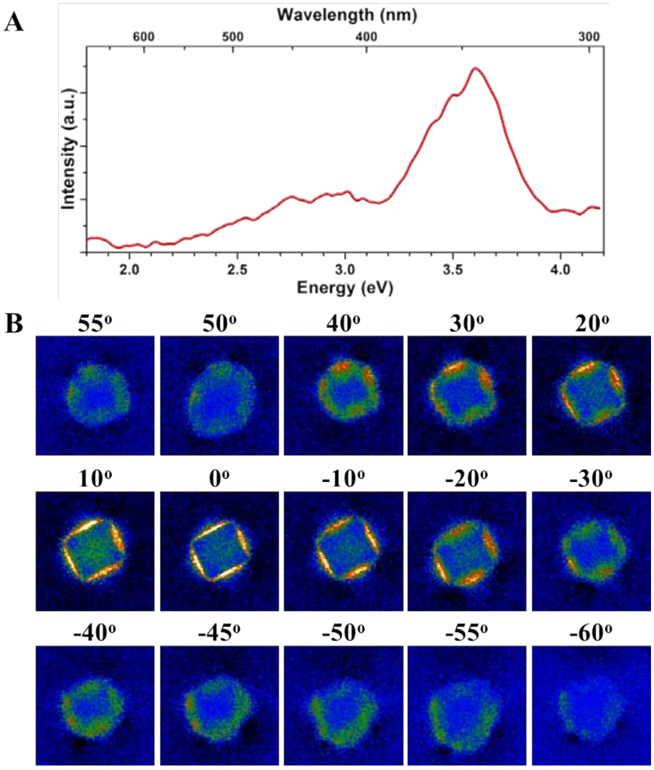

FIGURE 5.9: A. Spectrum of the component IV in Fig. 5.5 and its corresponding abundance maps for all tilt angles are shown in B.

Notice that we have presented only localized surface plasmon resonance modes from the corners, edges and/or faces of the Ag@Au core-shell nanocube in this section. Nevertheless, we mention about the bulk plasmon mode of Ag in the local plasmonic properties of nanocubes presented in Fig. 5.3, where it is indicated that the intensity of this bulk mode is much lower than those of the other surface plasmon modes. The investigated Ag@Au nanocube has been extracted from the very early stage of the galvanic reaction and most of the nanocube is not alloyed with Au. Therefore, this solid nanocube, except the few-nanometer-thick shell, contains the bulk plasmon mode of Ag all around the nanocube. In general, HAADF STEM micrographs are sufficient enough to indicate where the Ag is located in such a solid core-shell nanocube, hence, it can indicate the location of bulk plasmon mode of Ag. Still, we have obtained the component related to bulk plasmon mode of Ag at ∼3.8 eV as a proof of concept for this bulk mode. Its spectrum along with its corresponding abundance maps for all tilt angles are presented in Fig. 5.10. As seen in these maps, as, expected, this mode is present all over the nanocube. It is worth pointing out that its intensity is really low expecially for the higher tilt angles which makes it hard to distinguish from the background contributions.

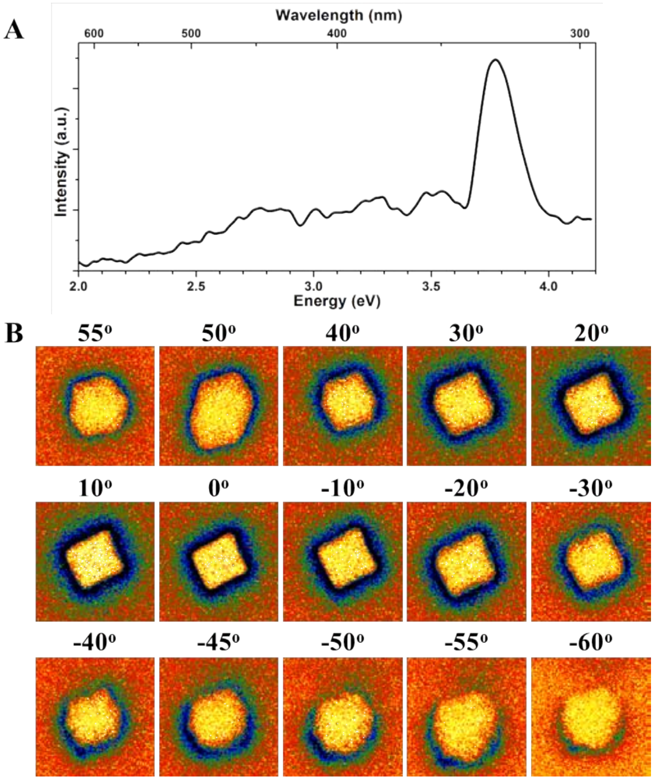

Figure 5.10: A. Spectrum of the component corresponding to the bulk plasmon resonance of Ag at ~3.8 eV and its abundance maps for all tilt angles are shown in B.

5.3 Partially hollow AgAu nanocube

5.3.1 Structural characterization

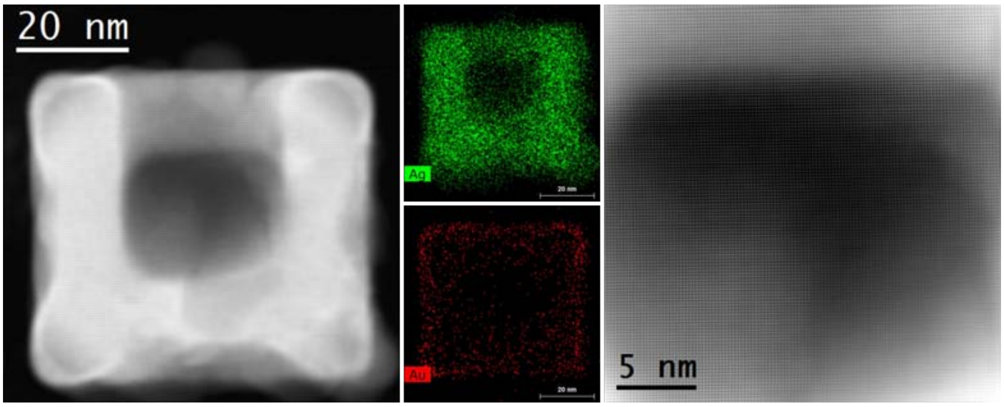

Figure 5.11: High resolution HAADF STEM micrograph of a 57 nm partially hollow AgAu nanocube. STEM-EDX maps of Ag (in green) and Au (in red). Detail of the centeral hollow part.

Fig. 5.11 shows high resolution HAADF STEM micrograph of a 57 nm partially hollow nanocube. This nanocube is choosen as a representative for the partially hollow nanocubes. Even though its hollow part is slightly bigger than the one used for 3D EELS mapping (Fig. 5.1), both possess quite similar structural features. Atomic resolution HAADF STEM reveals the presence of several nanometer thick, inhomogeneously distributed shell with a darker contrast around the nanocube surface in addition to the central part being hollow. E-beam induced damage on the nanocube is observed even during Atomic resolution HAADF STEM analyses. Elemental STEM-EDX maps reveals that the outer part of the nanocube is richer in Au compared to the other parts. Moreover, substantial amount of Au can be observed in the nanocube as well, which was not the case for the above presented Ag@Au core-shell nanocube. Quantification of the STEM-EDX revealed that the alloyed parts have an average composition of 71.5±1.3 at.% Ag and 28.5±1.3 at.% Au. Even after such a progressed galvanic replacement reaction, the nanocubes/hollow nanoboxes keep the mono crystallinity of the initial Ag nanocubes. On the right of Fig. 5.11, an atomic resolution HAADF STEM micrograph from the center of the partially hollow AgAu nanocube is presented, revealing that even on the hollow part of the nanocube, the structural phase projection has a perfect mono crystallinity.

5.3.2 Angle-resolved local plasmonic properties

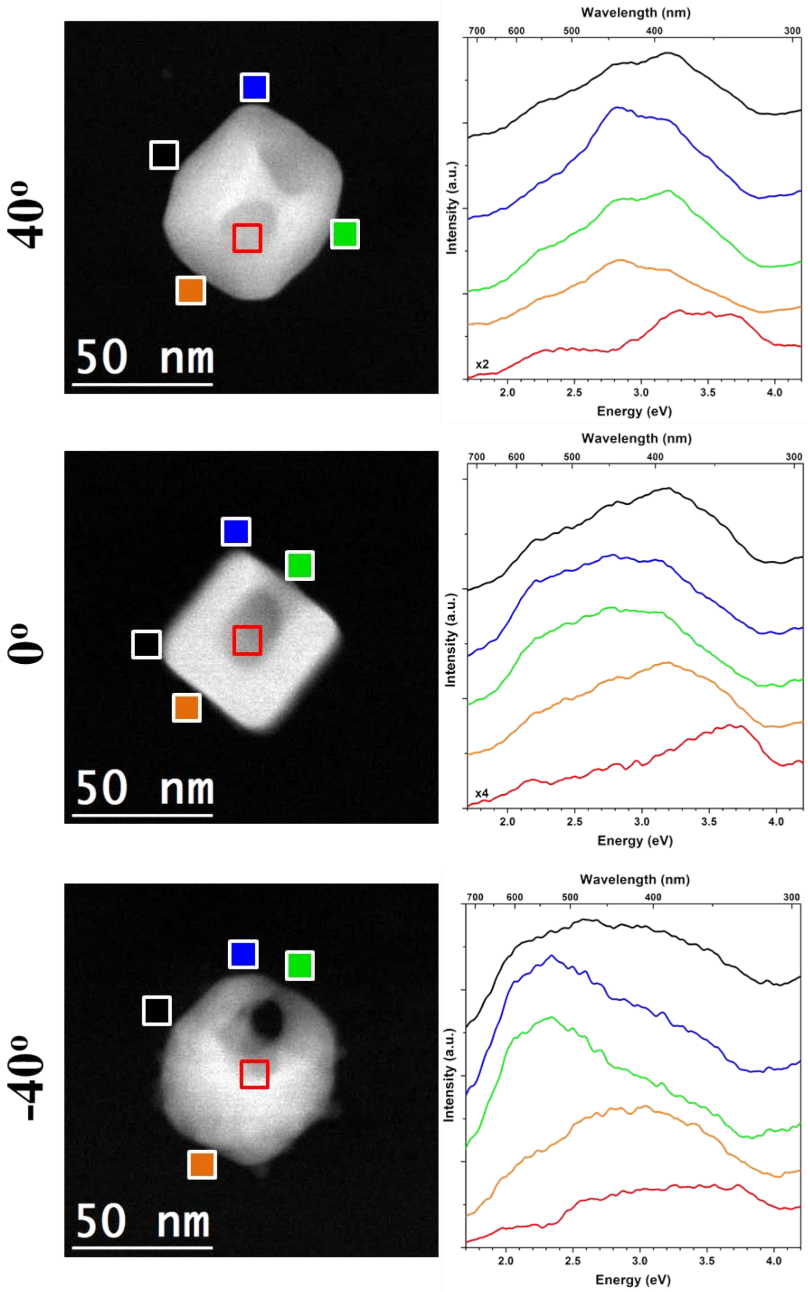

FIGURE 5.12: HAADF STEM micrographs (left) of the +40^o, 0^o, -40^o tilts of a 50 nm partially hollow AgAu nanocube and background subtracted local EEL spectra (right) of different locations shown by black, blue, green, orange and red squares. Note that the color of each spectra corresponds to the color of the location indicated in the HAADF STEM micrographs.

Fig. 5.12 shows HAADF STEM micrographs obtained from +40^o, 0^o, -40^o tilted 50 nm partially hollow AgAu nanocube and background subtracted local EEL spectra of the different locations such as corners, edges and bulk of the nanocube. The color of each EEL spectra correspond to the color of the selected area in the HAADF STEM micrographs. In general, local EEL spectra obtained from the different parts of the partially hollow nanocube reveal the presence of wide peaks containing multiple shoulder peaks which are related to different plasmon modes. Such wide peaks are observed mainly due to the low signal-to-noise ratio of the EELS datasets, as its reasons are explained previously. Several plasmon peaks located at ~2.2 eV, ~2.8 eV, ~3.2 eV, ~3.5 eV and ~3.8 eV can easily be idendified in the first instance. The effects of the hollow region on the local plasmonic properties can be seen by comparing the black and blue, or orange and green regions in the 0 degree tilted EEL spectra, where the dominant plasmon peaks of the hollow part are located at lower energies than those of the solid part. Although its orientation is not letting us observe as clearly as the Ag@Au core-shell nanocube presented in Fig. 5.3, the effects of the substrate can be seen by comparing the local EEL spectra of the blue and green regions of the +40^o tilted nanocube. The dominant plasmon peak of the EEL spectrum obtained from the blue region, which is in contact with the substrate, is located at ~2.8 eV, whereas the dominant plasmon peak of the green region, which is not in contact with the substrate, is located at ~3.2 eV. These two plasmon modes correspond to distal and proximal corner plasmon modes, respectively. The local EEL spectra obtained from the -40^o tilted nanocube mainly reveals the presence of low energy plasmon modes related to the hollow structure as this tilt angle allows the alignment of the void parallel to the e-beam. The effects of this void on the plasmonic properties of the nanocube can be understood by comparing the local plasmon resonances of the above presented Ag@Au core-shell nanocube (Fig. 5.3) and the local plasmon resonances of the partially hollow AgAu nanocube (Fig. 5.12). In aggrement with the conclusions of the previous chapter on plasmonic nanoengineering, LSPR peaks shift to lower energies due to the hollow nanostructure.

5.3.3 Processing of 3D plasmonic properties

Fig. 5.13 shows the HAADF STEM micrographs of the partially hollow AgAu nanocube obtained simultaneously with the EELS SI at different tilt angles between +60^o and -40^o with different intervals. Similar to above presented set for the core-shell nanocube, we started to obtain EELS maps from the maximum positive (+60) degrees and decreased the tilt until the maximum negative degrees. As the nanocube is exposed to higher dose of e-beam radiation after a certain number of EELS maps obtained at different tilts, the e-beam induced morphological changes started to appear and we had to finish the tilt series at a relatively lower angle of -40^o due to high extend of particle melting. 3D morphology of the partially hollow nanocube can be clearly seen in these HAADF STEM micrographs, where the presence of a cylindrical void along two faces of the nanocube is obviously revealed. In the following, the effects of this cylindrical void on the 3D plasmonic properties of the partially hollow AgAu nanocube are presented.

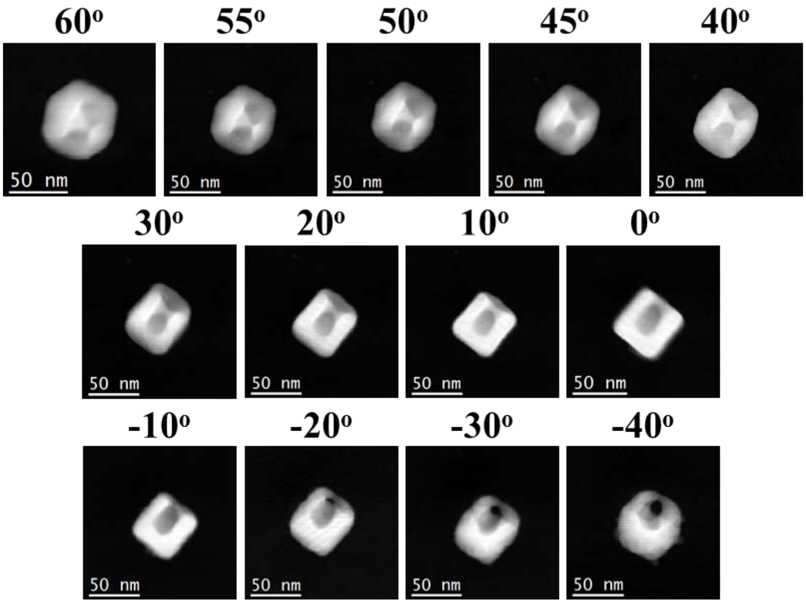

FIGURE 5.13: Series of HAADF STEM micrographs of the partially hollow AgAu nanocube obtained simultaneously with the EELS SI at different tilt angles between +60^o and -40^o with different intervals.

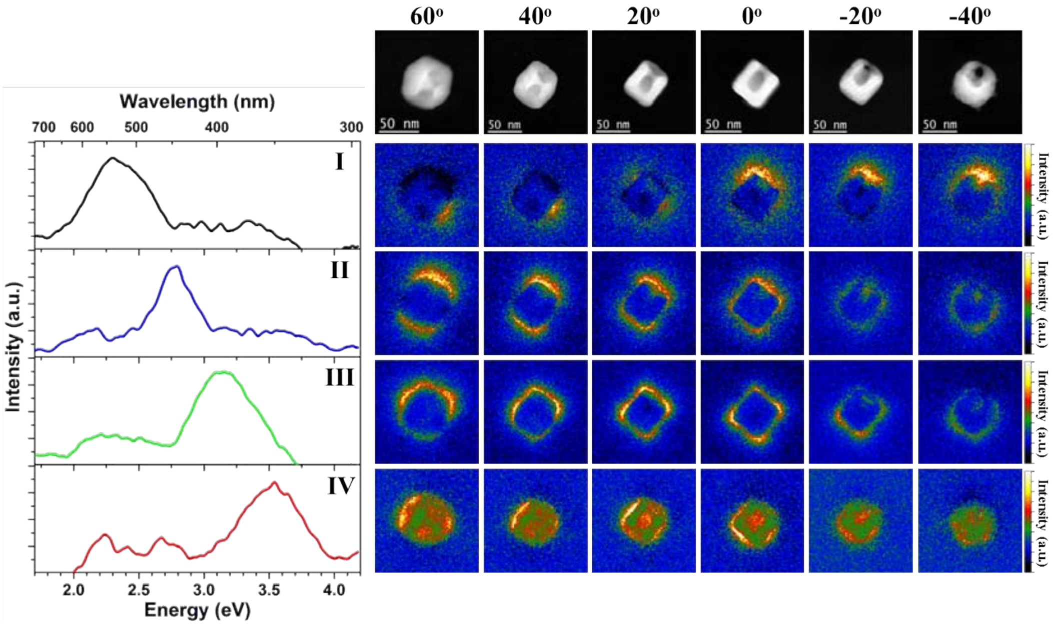

FIGURE 5.14: Spectra of 4 different components of the partially hollow AgAu nanocube, obtained by VCA and their corresponding abundance maps for different tilts. Intensity of the abundance maps are normalized within each component.

VCA processing on the EELS SIs obtained from the partially hollow AgAu nanocube revealed the presence of 4 different components. Their spectra and correponding abundance maps for selected +60, +40, +20, 0, -20 and -40 degrees are presented in Fig. 5.14. First component is a ~0.5 eV wide peak located at ~2.3 eV covering the plasmon resonances generated by the hollow part. Its abundance maps clearly reveal that this mode is highly intense at negative tilt angles in which the void is aligned almost parallel to the e-beam trajectory, which is in good agreement with the above presented local EEL spectra from the -40^o tilt. Similar to previous section, we present the abundance maps for all the 4 components at every tilt angle in the following as separate figures. The spectra and abundance maps for the components I, II, III and IV are presented in Fig. 5.15, Fig. 5.16, Fig. 5.17 and Fig. 5.18, respectively. The component II is located at ∼2.8 eV, which was introduced as the proximal corner mode of the nanocube in Fig. 5.12. Its corresponding abundance maps reveal that it has contributions from the plasmon resonances excited along the edge/face of the hollow part along with the resonances from the corners. The component III, which is located at ∼3.15 eV, is another corner plasmon mode present in along almost all tilt angles with high intensities. The last component presented in this nanocube (component IV) is located at ∼3.5 eV. Its abundance maps reveal that this mode is the Ag related face mode of the partially hollow AgAu nanocube. It is worth pointing out that it is present inside the void similar to the pinholed AuAg nanoboxes of the previous chapter (Figures 3.24 and 3.25).

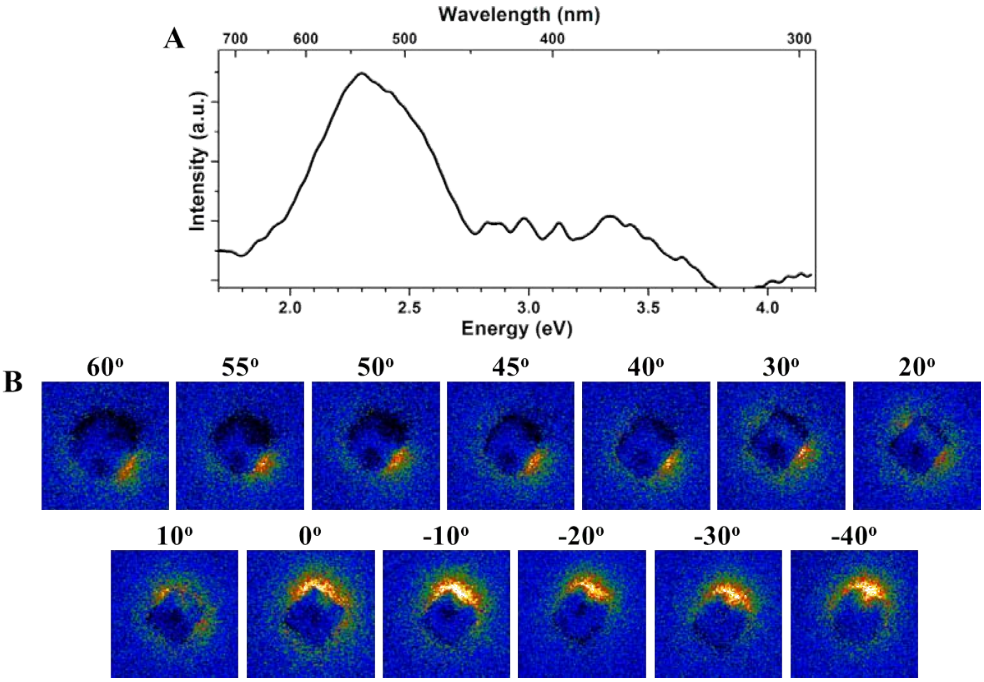

Figure 5.15: A. Spectrum of the component I in Fig. 5.14 and its corresponding abundance maps for all tilt angles are shown in B.

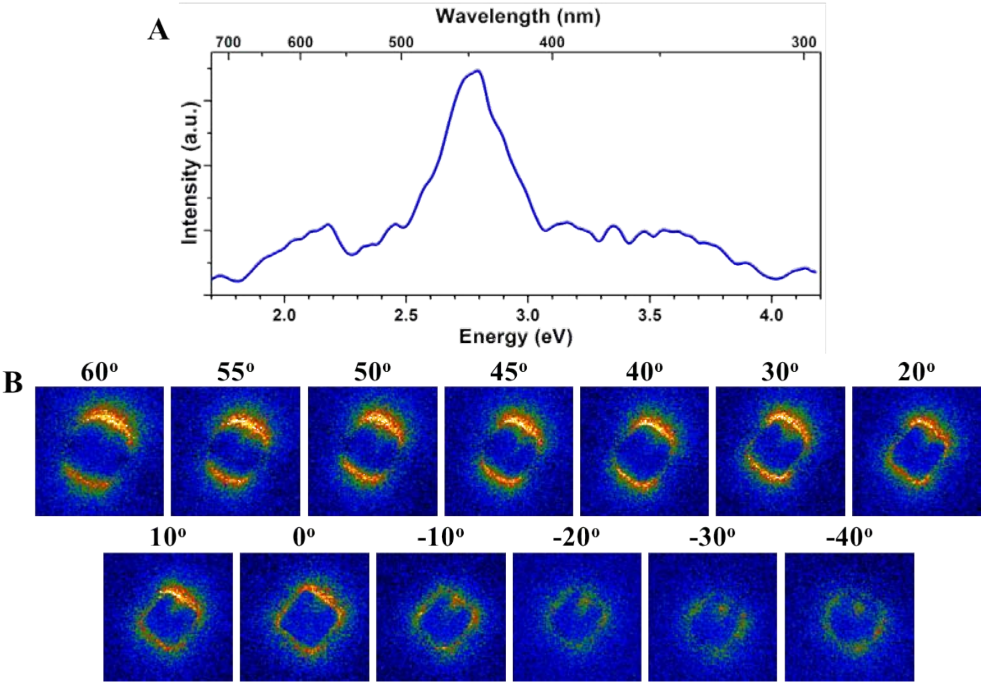

FIGURE 5.16: A. Spectrum of the component II in Fig. 5.14 and its corresponding abundance maps for all tilt angles are shown in B.

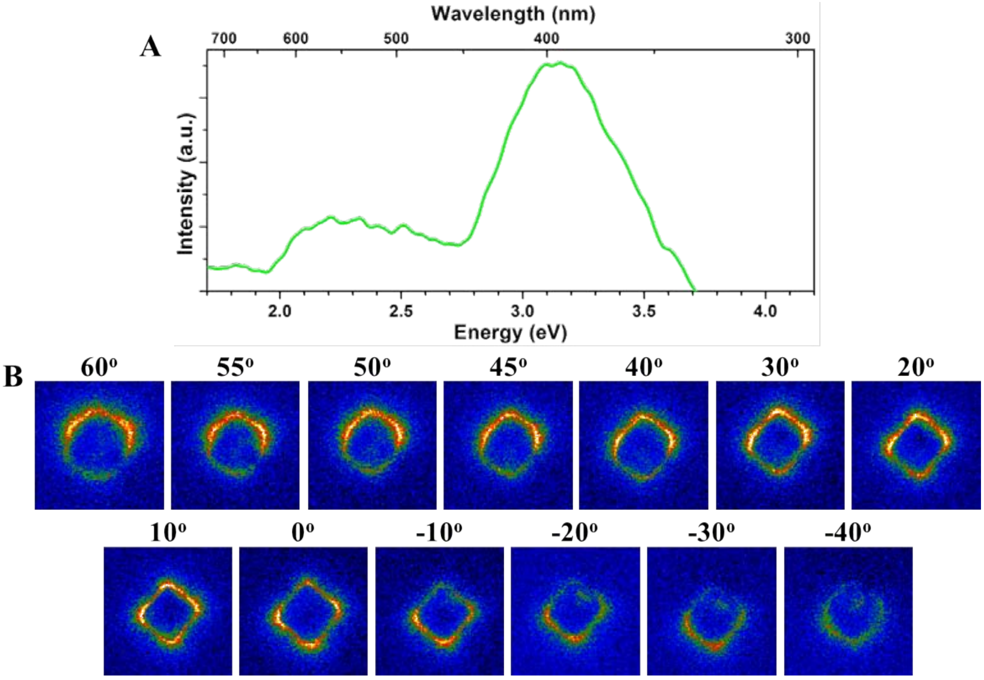

FIGURE 5.17: A. Spectrum of the component III in Fig. 5.14 and its corresponding abundance maps for all tilt angles are shown in B.

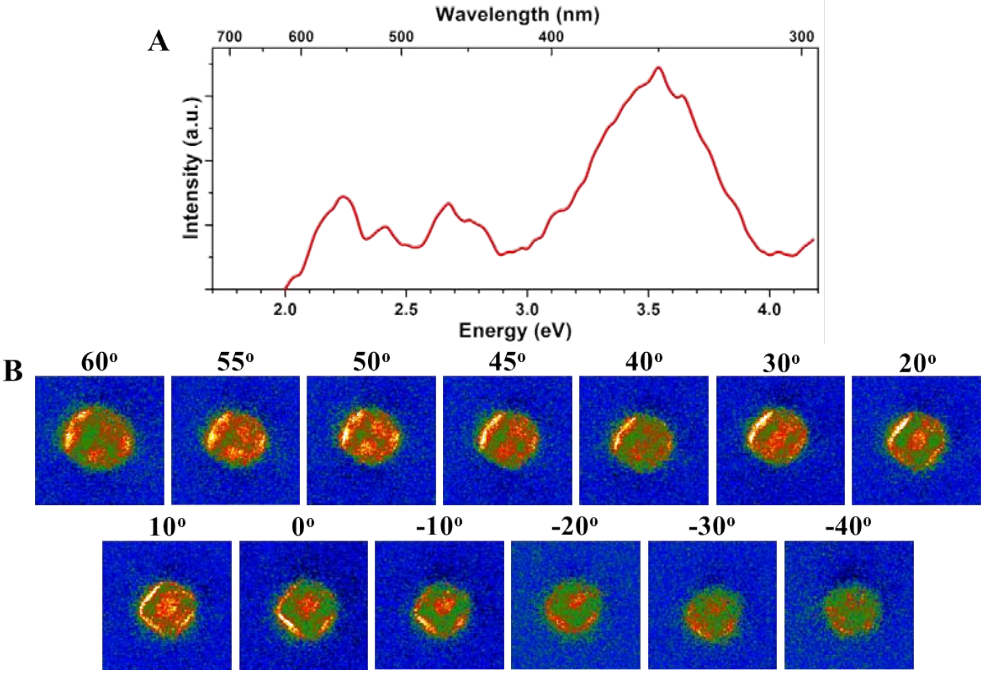

Figure 5.18: A. Spectrum of the component IV in Fig. 5.14 and its corresponding abundance maps for all tilt angles are shown in B.

5.4 Hollow AuAg nanoframe

5.4.1 Structural characterization

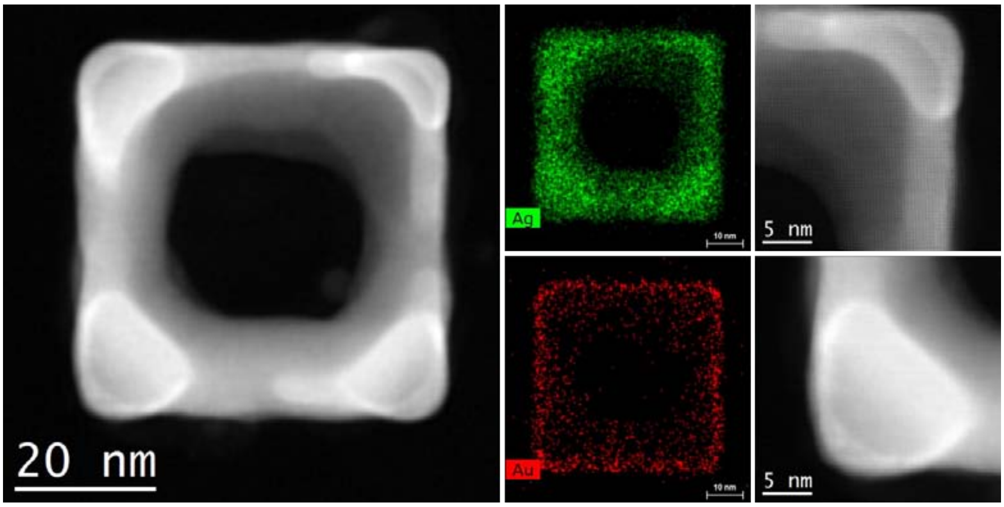

FIGURE 5.19: Atomic resolution HAADF STEM micrograph ~ of a 53 nm hollow AuAg nanoframe. STEM-EDX maps of Ag (in green) and Au (in red). Details of upper right and lower left corners.

Fig. 5.19 shows atomic resolution HAADF STEM micrograph of a 53 nm hollow AuAg nanoframe-like structure.It should be noted here that the synthesis procedure of this nanostructure is different than the one presented in the previous chapter as AuAg nanoframe (Fig. 3.37A). The present nanoframe-like structure is also from the initial stage of the galvanic replacement reaction [69], yet, it get hollow due to the replacement reaction taken fast and inhomogeneously. As seen in the HAADF STEM micrographs, there are still unalloyed parts, with bright contrasts, at the corners of the nanoframe, which was not the case for the nanoframe presented in Chapter 3, synthesized by a slower galvanic replacement reaction. This nanostructure is choosen as a representative for the hollow AuAg nanoframe presented in this chapter (Fig. 5.1). Elemental STEM-EDX maps reveals that the outer part of the nanoframe is richer in Au compared to the other parts, where the parts with brighter contrast are rich in Ag. Overall quantification of the STEM-EDX revealed that this nanoframe is composed of 58.8±1.2 at.% Ag and 41.2±1.2 at.% Au. It is clear from the elemental maps that the Ag and Au are distributed quite inhomogeneously through out the nanoframe. For instance, it is stated that outer parts are rich in Au compared to the inner parts. Quantification of the STEM-EDX from the inner and outer parts of the edges revealed that the outer parts are composed of 52.3±0.7 at.% Ag and 47.7±0.7 at.% Au, whereas the inner parts have a composition of 72.7±0.3 at.% Ag and 27.3±0.3 at.% Au. There is about a 20 at.% difference between the inner and outer part of the same edge, suggesting that the Au deposition takes places faster than the diffusion during the synthesis [306]. On the right, detailed atomic resolution HAADF STEM micrographs taken from the upper left corner of the nanoframe are presented, showing the mono crystallinity of the solid and projected hollow parts. The HAADF STEM micrograph from the lower right corner reveals the different focus of the freshly deposited Au parts with a several atomic layer thickness.

5.4.2 Angle-resolved local plasmonic properties

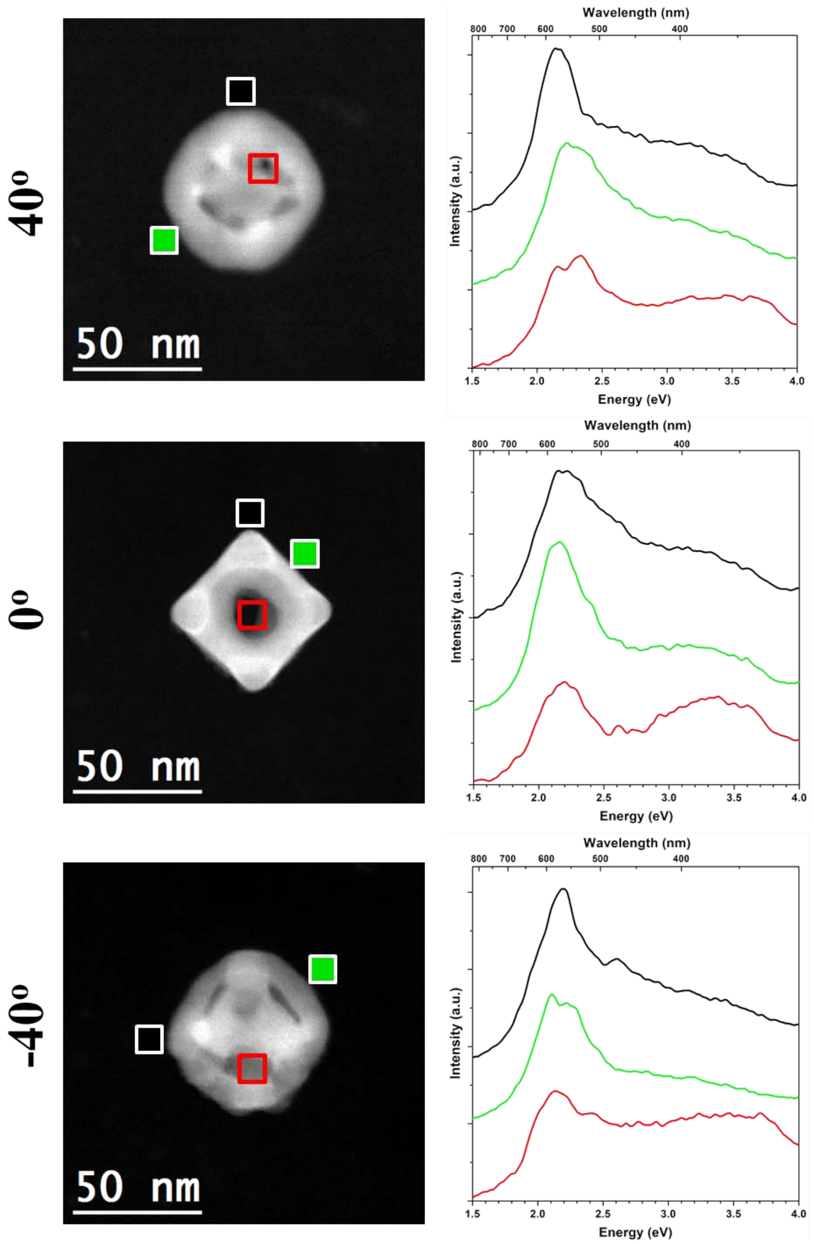

FIGURE 5.20: HAADF STEM micrographs (left) of the +40^o, 0^o, -40^o tilts of a 47 nm hollow AuAg nanoframe and background subtracted local EEL spectra (right) of different locations shown by black, blue, and red squares. Note that the color of each spectra corresponds to the color of the location indicated in the HAADF STEM micrographs.

Fig. 5.20 shows HAADF STEM micrographs obtained from +40^o, 0^o, -40^o tilted 47 nm hollow AuAg nanoframe and background subtracted local EEL spectra of the different locations such as corners, edges and center of the nanoframe. The color of each EEL spectra correspond to the color of the selected area in the HAADF STEM micrographs. It has been revealed in the Chapter 3 that plasmon peaks shift to lower energies as the void size increases in the cuboid AuAg nanostructures. It is also shown that plasmon resonances are distributed homogeneously around the hollow nanostructures such as nanoboxes and nanoframes. The local EEL spectra from the hollow AuAg nanoframe shown here (Fig. 5.20) and its comparison with the above presented local EEL spectra from the Ag@Au core-shell nanocube (Fig. 5.3) and partially hollow AgAu nanocube (Fig. 5.12) concur the conclusions drawn in the previous chapter. In general, local EEL spectra obtained from the different parts of the hollow AuAg nanoframe reveal the presence of plasmon peaks located at ∼2.3 eV with ±0.2 eV local modification depending on the tilt angle and the location. It would be logical to assume the appearance of some Ag-related plasmon resonances in this nanostructure, related to the presence of some unalloyed areas, as observed in the HAADF STEM micrographs of Fig. 5.19. These Ag-related plasmon resonances can be observed in the local EEL spectra obtained from the centeral parts (indicated in red) as wide peaks at higher energies around 3.5 eV. However, as shown in these EEL spectra, their intensities are significantly lower than those of the main localized surface plasmon resonances generated around the hollow parts. It should also be pointed out that, in some regions, two different plasmon resonances with quite similar energies are observed from the same selected area. For instance, the local EEL spectrum obtained from the red squared region of the +40^o tilted nanoframe reveals the splitting of the dominant peak into two peaks located at ∼2.15 eV and ∼2.35 eV.

5.4.3 Processing of 3D plasmonic properties

Fig. 5.21 shows the HAADF STEM micrographs of the hollow AuAg nanoframe obtained simultaneously with the EELS SI at different tilt angles between +60^o and -55^o with different intervals. The 3D morphology of the hollow nanoframe can be clearly observed in the HAADF STEM micrographs, where the presence of voids with different sizes are visible at different faces of the nanoframe. The cubic shape with rounded corners seems to be homogeneous for all tilt angles, where the size of pinhole like voids are differentiating from several nanometer to about 20 nm. Although partial morphological changes are observed at the higher negative tilt angles as -50 and -55 degrees, we could obtain reasonably high quality EELS maps at 16 different angles between +60^o and -55^o. In the following, we present the processing of EELS datasets from each tilt angle obtained by VCA.

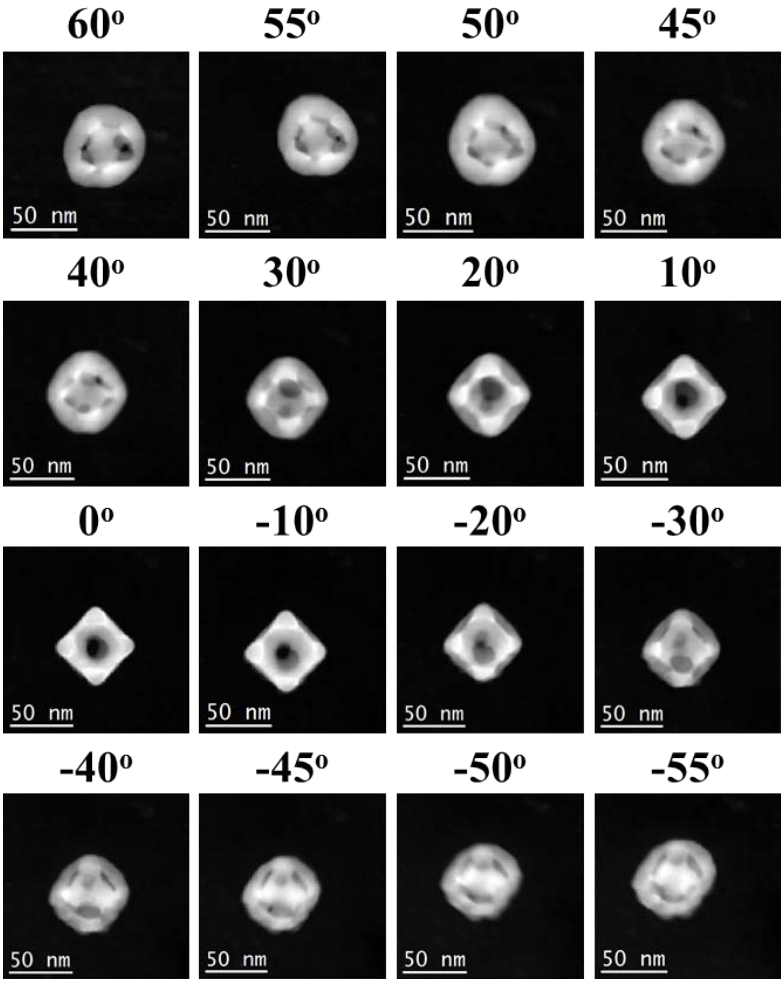

FIGURE 5.21: Series of HAADF STEM micrographs of the hollow AuAg nanoframe obtained simultaneously with the EELS SI at different tilt angles between +60^o and -55^o with different intervals.

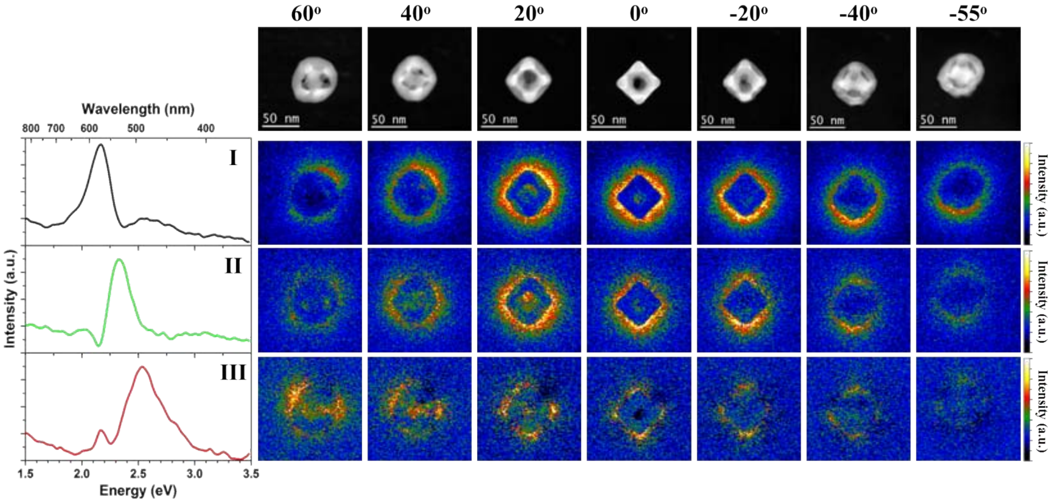

FIGURE 5.22: Spectra of 3 different components of the hollow AuAg nanoframe, obtained by VCA and their corresponding abundance maps for different tilts. Intensity of the abundance maps are normalized within each component.

VCA processing on the EELS SIs obtained from the hollow AuAg nanoframe revealed the presence of 3 different components. Their spectra and correponding abundance maps for selected tilt angles of +60, +40, +20, 0, -20 and -40 degrees are presented in Fig. 5.22. As shown in the above presented local EEL spectra, main plasmon resonances all around the nanoframe are located at similar energies and the spectral unmixing obtained by VCA generated 3 components located at ∼2.15 eV, ∼2.35 eV and ∼2.5 eV. Similar to the previous section, we present the abundance maps of all 3 components for every tilt angle in the following as separate figures. The spectra and abundance maps of components I, II and III are presented in Fig. 5.23, Fig. 5.24 and Fig. 5.25, respectively. Abundance maps of the component I (located at ∼2.15 eV) reveal that this mode is present all around the nanoframe with high intensities. Again, such a distribution in hollow nanostructures is in good agreement with the literature [139, 140] and the experimental and simulation results in Chapter 3. The second component, which is located at a slightly higher energy of ∼2.35 eV, is also distributed intensely around the nanoframe. Both of these localized surface plasmon modes are present along the inner voids of the nanoframe. The third mode located at ∼2.55 eV seems to be a corner mode with low intensities, especially at the negative tilt angles. As mentioned above, VCA processing did not generate any Ag-related plasmon resonance at higher energies above the main plasmon resonances of the hollow nanoframe within the primary components due to their suppressed intensities.

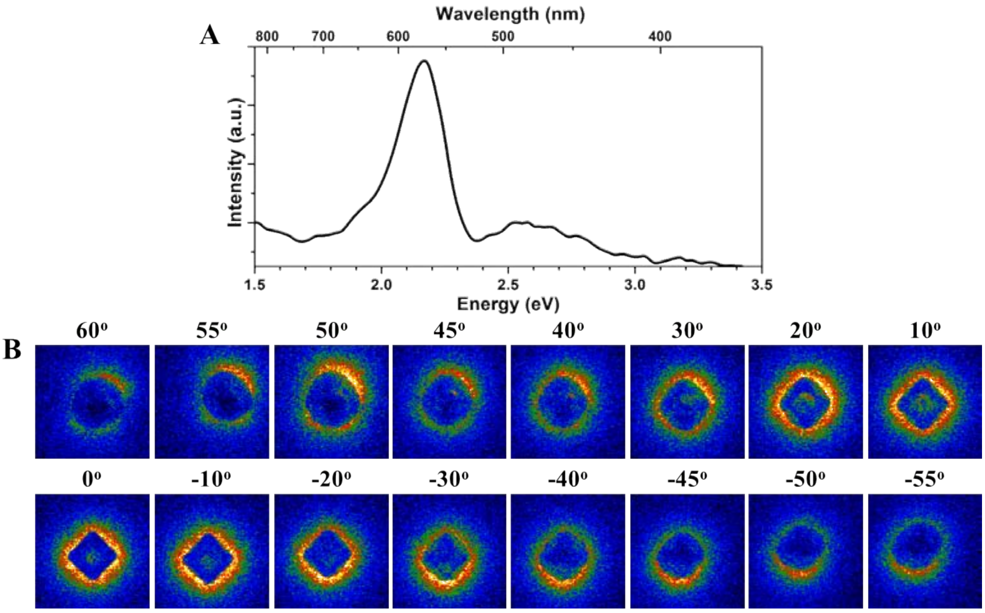

FIGURE 5.23: A. Spectrum of the component I in Fig. 5.22 and its corresponding abundance maps for all tilt angles are shown in B.

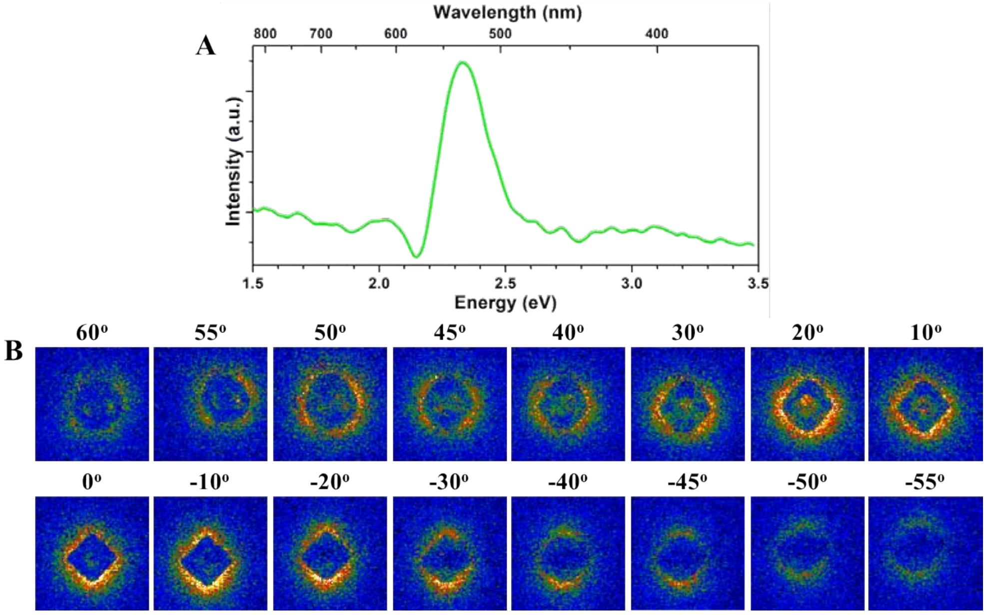

FIGURE 5.24: A. Spectrum of the component II in Fig. 5.22 and its corresponding abundance maps for all tilt angles are shown in B.

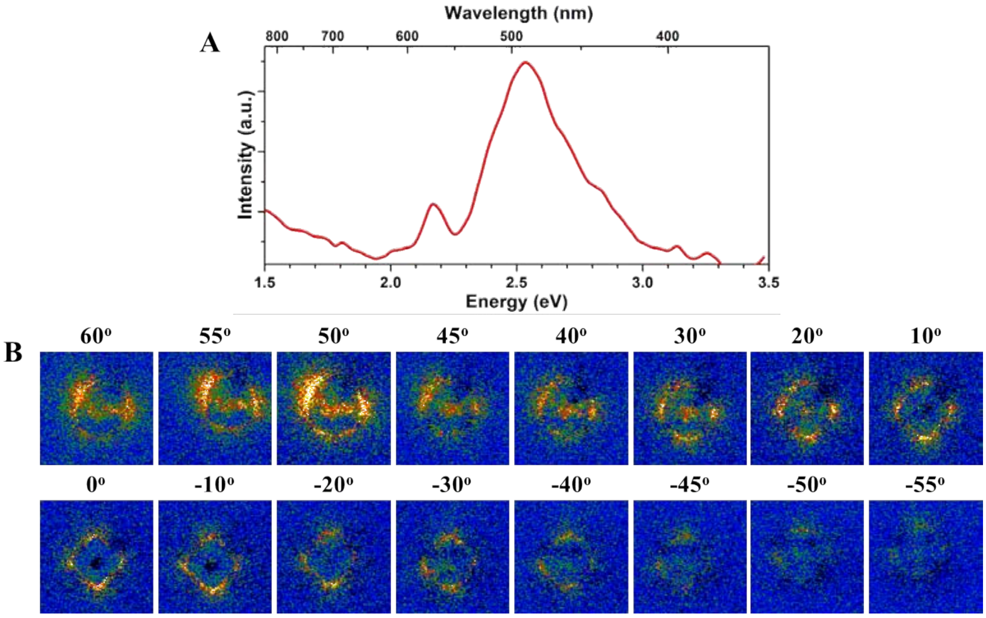

FIGURE 5.25: A. Spectrum of the component III in Fig. 5.22 and its corresponding abundance maps for all tilt angles are shown in B.

5.5 Plasmon coupling between two Ag@Au core-shell nanocubes

5.5.1 Angle-resolved local plasmonic properties

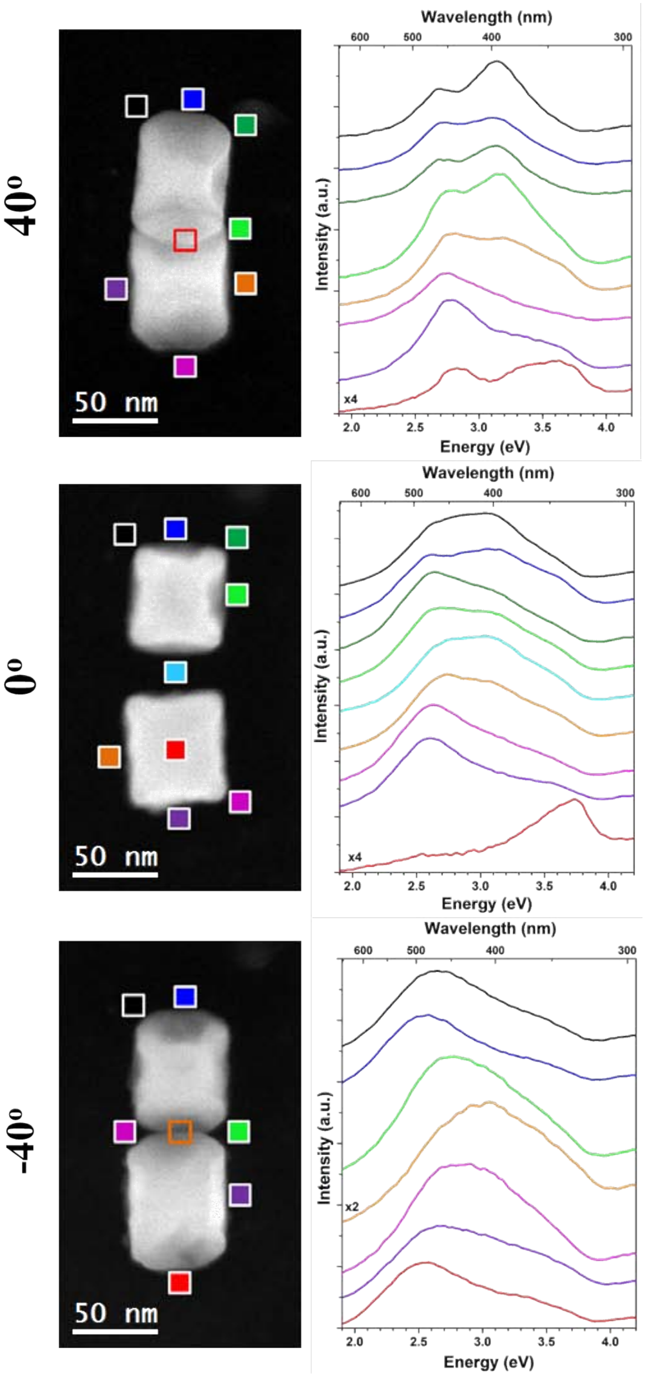

FIGURE 5.26: HAADF STEM micrographs (left) of the +40^o, 0^o, -40^o tilts of a 59 nm and a 53 nm Ag@Au core-shell nanocubes standing with a separation of ∼22 nm. On the right, the background subtracted local EEL spectra of different locations shown by black, blue, dark green, green, turquoise, orange, violet, purple and red squares are shown. Note that the color of each spectra corresponds to the color of the location indicated in the HAADF STEM micrographs.

In this section, we present the 3D EELS study conducted on two Ag@Au nanocubes (59 nm and 53 nm in sizes) standing next to one another with a gap of ~22 nm in order to investigate the coupling of plasmon resonances of two nanocubes in 3D. As these core-shell nanocubes are essentially similar to the ones presented above, the structural information is not presented again. Therefore, we start with the angle resolved plasmonic properties of the selected areas. Fig. 5.26 shows the HAADF STEM micrographs taken from the +40^o, 0^o, -40^o tilted nanocubes and background subtracted local EEL spectra of different locations indicated with colored squares (which are 8 pixel by 8 pixel).

In general, the presence of wide peaks between ~2.5 eV and ~3.5 eV are observed in the local EEL spectra at several locations. The selected area of the upper corners and edge (areas indicated by black, blue and dark green squares) of the 0^o tilted upper nanocube reveals the presence of multiple peaks located at ~2.6 eV, ~3.1 eV and ~3.6 eV, where their relative intensities change from location to location. For instance, the dominant peak of the upper left corner is located at ~3.1 eV, whereas the dominant peak of the upper right corner is located at ~2.6 eV. Another difference between the local EEL spectra of these two corners can be the intensity of a lower energy plasmon peak (located at ~2.4 eV, seems to be hidden by the tail of the main plasmon peaks) being higher at the right corner. These discrepancies can be understood by looking at the HAADF STEM micrograph, where the unalloyed Ag part at the upper right corner of the upper nanocube seems to be "sharper" than the other corners resulting in the lower energy plasmon resonances. This core-shell nanocube is quite similar to the one presented in the previous chapter (Fig. 3.14), where it is also pointed out that such morphological differences lead to different plasmon resonances. The local EEL spectrum obtained from the gap between the two nanocubes also shows the presence of a wide peaks containing multiple plasmon resonances two of which are located at ~2.7 eV and ~3.1 eV. Lower parts of the lower nanocube (the lower right corner in violet and lower edge in purple) reveal the presence of a main plasmon peak at ~2.6 eV. The presence of such low energy plasmon resonances along the edges of the nanocubes as a dominant plasmon resonance (see the EEL spectra from the upper edge of the upper nanocube (in blue) and lower edge of the lower nanocube(in purple)), may be an indication of plasmon coupling between two nanocubes as it was not the case for the above presented Ag@Au core-shell nanocubes. The presence of a coupling resonance mode can be revealed in the following with the VCA processed plasmon components and abundance maps. Moreover, the presence of the bulk plasmon mode related to Ag can be clearly seen in the EEL spectrum (in red) obtained from the center of the lower nanocube.

Local EEL spectra obtained from the +40^o tilted nanocubes revealed the presence of two main plasmon peaks in several locations. The first one is located between 2.7 and 2.8 eV, depending on the location, and it is highly intense at the edges of the lower nanocube. On the other hand, the other peak located between 3.1 eV and 3.2 eV is highly intense at the corners of the upper nanocube and at the region indicated with a green square where the corners of two nanocubes seem to overlap. The local EEL spectra obtained from the -40^o tilted nanocubes show the presence of a relatively dominant peak for every location, whose energy slightly varies locally between 2.5 eV and 3.1 eV. The upper part of the upper nanocube (in blue) and the lower part of the lower nanocube (in red) reveal almost identical local EEL spectra with the main plasmon peak located at ∼2.5 eV, supporting the above mentioned claims about plasmon coupling.

5.5.2 Processing of 3D plasmonic properties

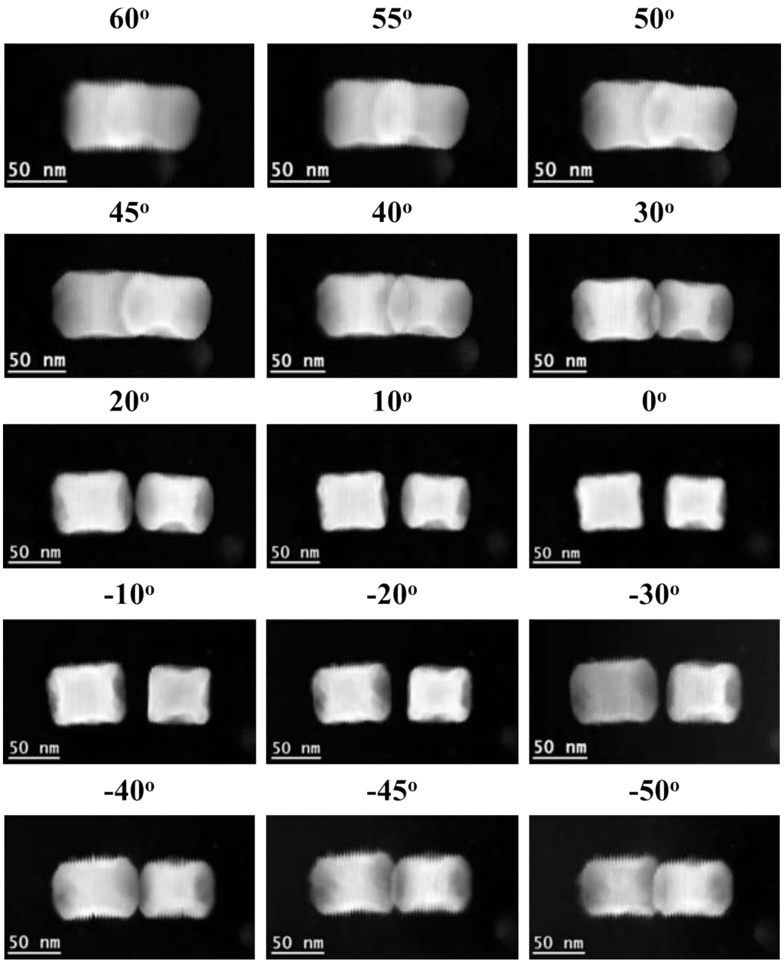

FIGURE 5.27: Series of HAADF STEM micrographs for the two Ag@Au core-shell nanocubes obtained simultaneously with the EELS SI at different tilt angles between +60^o and -50^o with different intervals.

Fig. 5.27 shows the HAADF STEM micrographs of the Ag@Au core-shell nanocubes obtained simultaneously with the EELS SI at different tilt angles between +60^o and -50^o with different intervals. As seen in this figure, we have rotated the HAADF STEM micrographs 90 degrees versus the clockwise direction for convenience when presenting the data. We will also present the abundance maps of different components like these HAADF STEM in the following. We could obtain EELS maps for the 15 tilt angles +60^o and -50^o as indicated in this figure. It can be seen from these HAADF STEM micrographs that the sample was drifting during the acquisition moslty due to the e-beam induced charging. Nevertheless, we could obtained good enough EELS maps allowing us to study the 3D plasmonic properties of these nanocubes. The HAADF STEM micrographs reveal that the smaller nanocube (53 nm in size, on the right) has more alloyed parts than those of the larger nanocube (59 nm in size, on the left), which is related to the Au amount per surface area during the galvanic replacement reaction [69]. Tilt axis of these series seems to be parallel to the alignment of nanocubes.

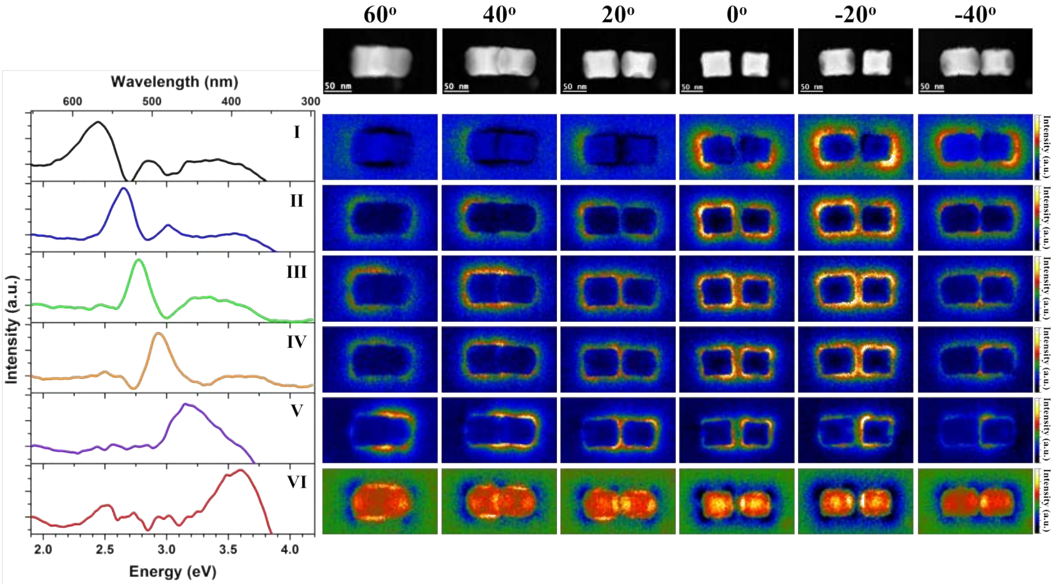

FIGURE 5.28: Spectra of 6 different components of the Ag@Au core-shell nanocubes, obtained by VCA and their corresponding abundance maps for different tilts. Intensity of the abundance maps are normalized within each component.

Spectra of 6 different components obtained from the EELS SIs for the two Ag@Au core-shell nanocubes by VCA and their corresponding abundance maps for selected tilt angles of +60, +40, +20, 0, -20 and -40 degrees are presented in Fig. 5.28. Again, similar to the above presented results on 3D plasmonic properties, we present the components and their corresponding abundance maps for every tilt angles in the following as separate figures, where the abundance maps of the components I, II, III, IV, V and VI are presented in Fig. 5.29, Fig. 5.30, Fig. 5.31, Fig. 5.32, Fig. 5.33 and Fig. 5.34, respectively.

The component I is located ∼2.45 eV. Its abundance maps reveal that it is present mainly at the outer edges of two nanocubes forming a kind of bipolar plasmon mode. We believe that such abundance maps for this mode suggest that it is generated due to the interaction between the plasmon modes of these two Ag@Au nanocubes located

∼22 nm away from one another. The fact that there is no intensity at the gap between two nanocubes reveals that this is a bonding mode [93, 215, 286]. It is also clear that this mode is highly intense at the negative tilt angles where there is a gap between two nanocubes. The second component, located at ∼2.65 eV, is mostly generated from the corners of the nanocubes. Its intensities are lower at higher tilt angles for both positive and negative degrees. The component III is located at ∼2.8 eV and it is mostly present at the corners with some contributions from the edges (see 0^o tilt). The component IV is another corner mode located at ∼2.95 eV. The plasmon resonances generated from these corner modes of both of the nanocubes seem to be interacting with one another. The reconstructions of each mode will reveal the extend of the interaction in 3D. The spectrum of component V shows a relatively wide peak located at ∼3.2 eV. Its corresponding abundance maps, especially the ones at the lower tilt angles, indicated that this mode is an anti-bonding coupling mode [215, 307]. The last plasmon mode obtained from these two Ag@Au core-shell nanocubes, except the bulk plasmon mode of Ag which is not presented, is the Ag-related face mode of the nanocubes located at ∼3.6 eV (component VI). As suggested by the name of the plasmon mode, it is present along the faces of both nanocubes and visible, to some extend, for all tilt angles.

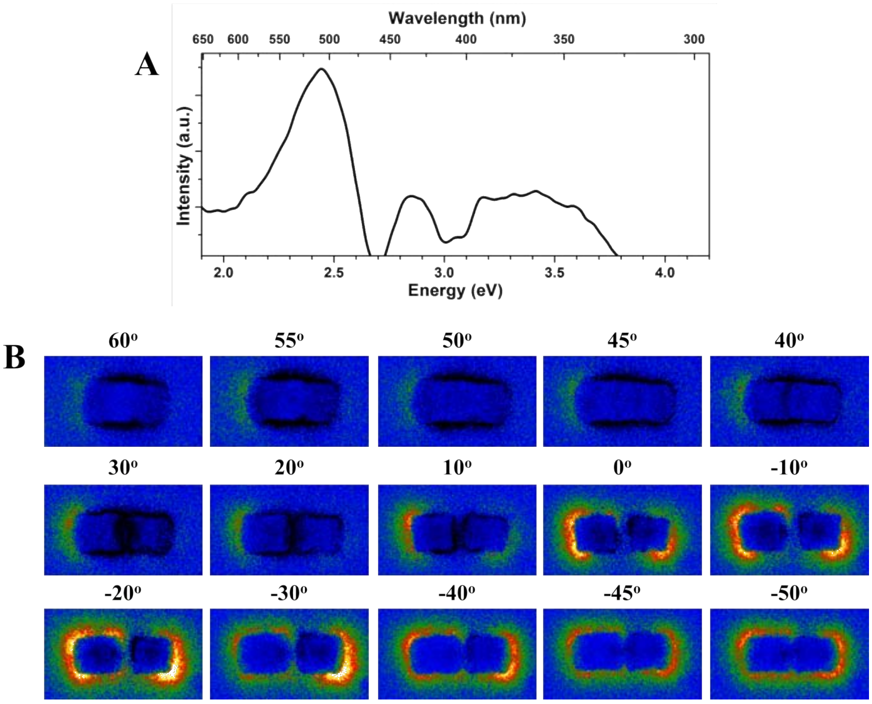

FIGURE 5.29: A. Spectrum of the component I in Fig. 5.28 and its corresponding abundance maps for all tilt angles are shown in B.

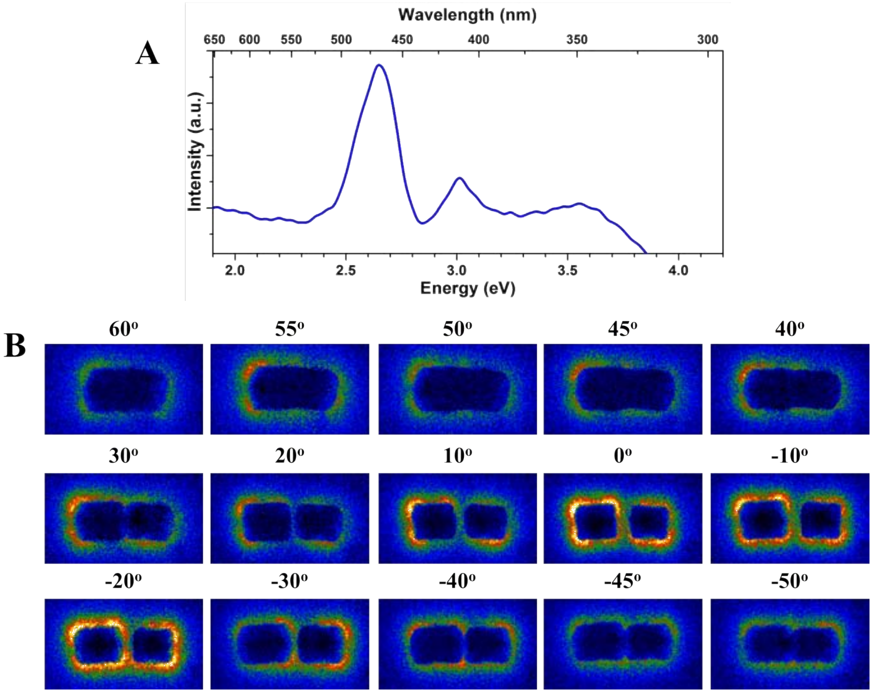

FIGURE 5.30: A. Spectrum of the component II in Fig. 5.28 and its corresponding abundance maps for all tilt angles are shown in B.

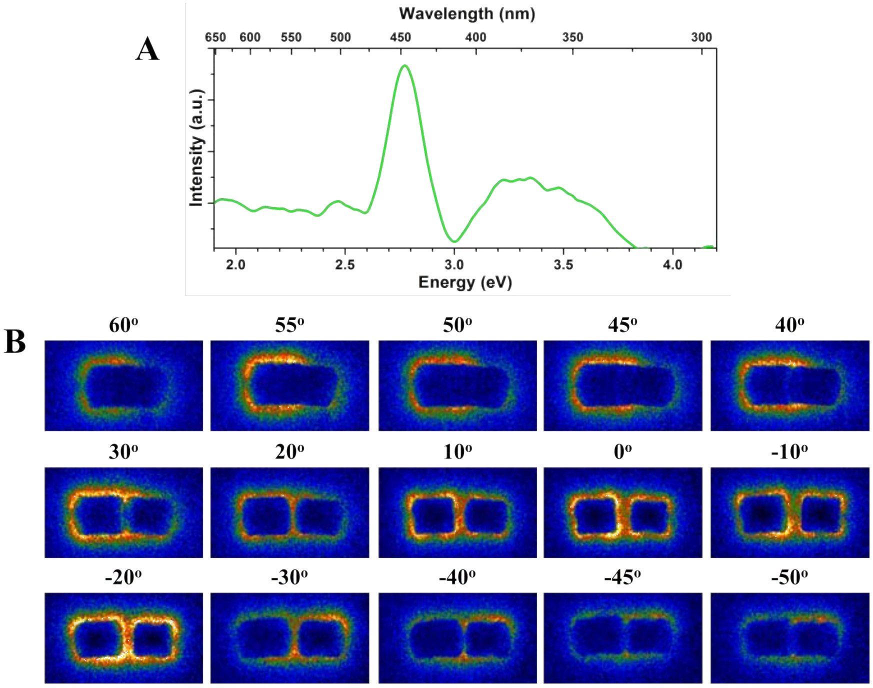

FIGURE 5.31: A. Spectrum of the component III in Fig. 5.28 and its corresponding abundance maps for all tilt angles are shown in B.

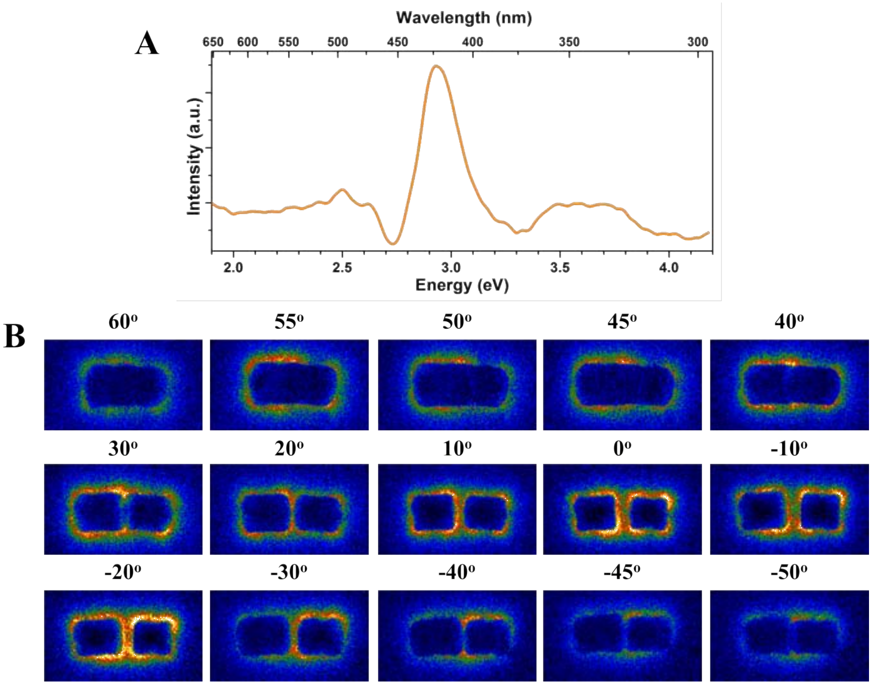

FIGURE 5.32: A. Spectrum of the component IV in Fig. 5.28 and its corresponding abundance maps for all tilt angles are shown in B.

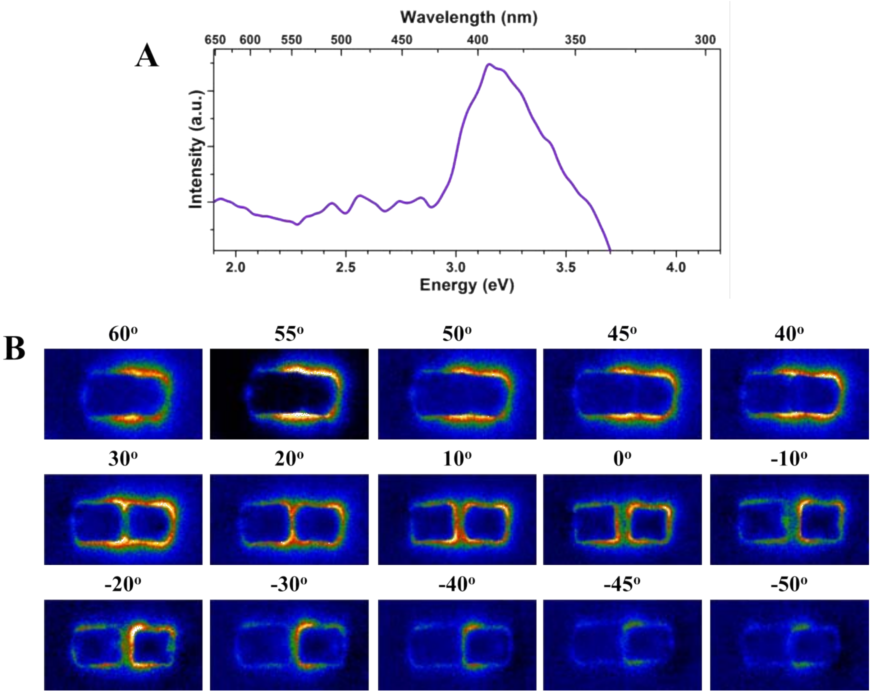

FIGURE 5.33: A. Spectrum of the component V in Fig. 5.28 and its corresponding abundance maps for all tilt angles are shown in B.

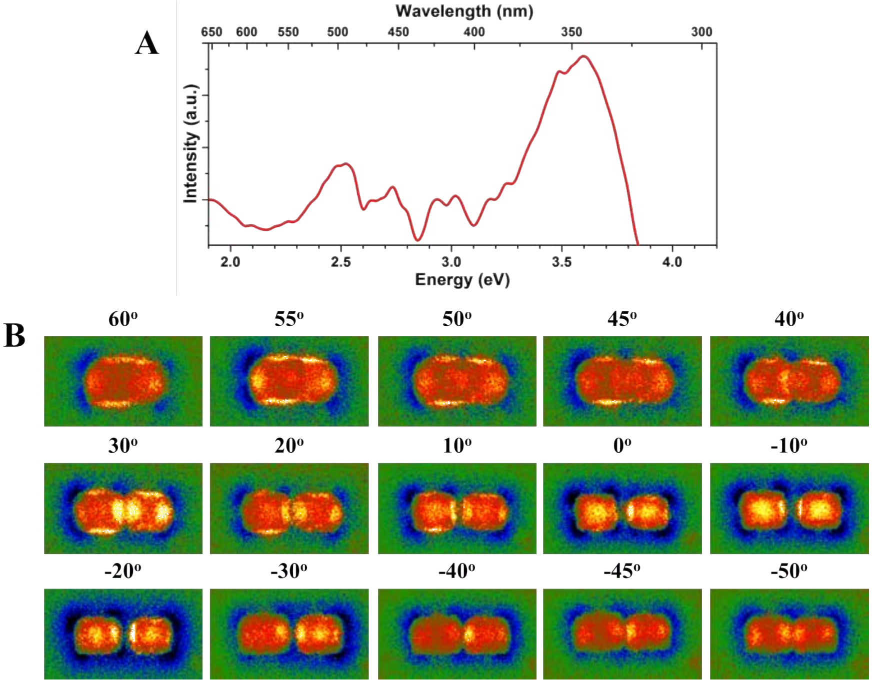

FIGURE 5.34: A. Spectrum of the component VI in Fig. 5.28 and its corresponding abundance maps for all tilt angles are shown in B.

5.6 Plasmon coupling between an Ag@Au core-shell nanocube and an AuAg nanoframe

5.6.1 Angle-resolved local plasmonic properties

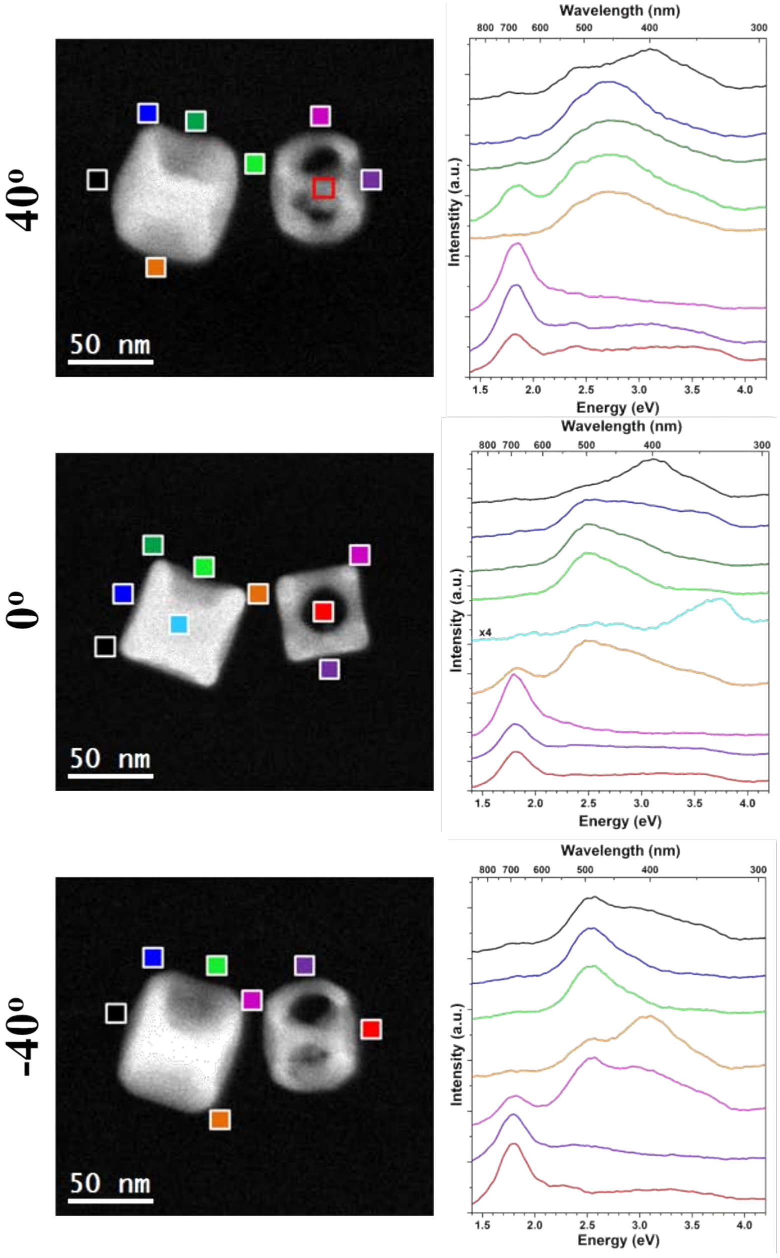

FIGURE 5.35: HAADF STEM micrographs (left) of the +40^o, 0^o, -40^o tilts of a 63 nm Ag@Au core-shell nanocube and a 53 AuAg nanoframe standing with $\sim$ 14 nm separation. On the right, the background subtracted local EEL spectra of different locations shown by black, blue, dark green, green, turquoise, orange, violet, purple and red squares are shown. Note that the color of each spectra corresponds to the color of the location indicated in the HAADF STEM micrographs.

In this section, we present another example of 3D plasmon coupling between a 63 nm Ag@Au core-shell nanocube and a 53 AuAg nanoframe standing with ∼ 14 nm separation. We have obtained 3D EELS study on the Ag@Au nanocube and AuAg nanoframe in order to investigate the coupling of plasmon resonances of a solid nanocube and hollow nanoframe in 3D. Fig. 5.35 shows the HAADF STEM micrographs taken from the +40^o, 0^o, -40^o tilted nanocube and nanoframe couple and background subtracted local EEL spectra of different locations indicated with colored squares (which are 6 pixel by 6 pixel). As seen in these figures, the solid core-shell nanocube and hollow nanoframe have quite distinctive plasmon resonances, whereas the gap between two nanostructures contains plasmon resonances of both. STEM micrographs reveal that the galvanic replacement did not take place homogeneously for the Ag@Au core-shell nanocube where the upper part of the nanocube is alloyed more than the other parts. The AuAg nanoframe has a 27 nm spherical void as revealed by the STEM micrograph taken at 0^o tilt, which may be different along the other faces. The presence of wide peaks at ∼2.5 eV, ∼2.9 eV, ∼3.1 eV and ∼3.6 eV are revealed at selected area EEL spectra taken from different parts of the 0^o tilted core-shell nanocube. The dominant plasmon peak of the upper left corner, which is closer to the alloyed part, is located at lower energy of ∼2.5 eV, in contrary to the dominant plasmon peak of the lower left corner located at ∼3.1 eV. The EEL spectrum from the center of the solid nanocube (in turquoise) revealed the presence of bulk plasmon resonance of Ag at ∼3.8 eV. The selected area EEL spectra from the different parts of the hollow nanoframe revealed the presence of plasmon peaks with similar energies of 1.8±0.1 eV all around the nanoframe. Such a homogeneous distribution of plasmon resonances in hollow nanostructures is consistent with the above presented results. The selected area EEL spectra taken from location with the shortest gap between nanostructures (indicated with orange in 0^o tilted STEM micrograph) contains two major peaks located at ∼1.8 eV, mostly related to the nanoframe, and at ∼2.5 eV, mostly related to the core-shell nanocube. The selected area EEL spectra obtained from the different parts of +40^o tilted core-shell nanocube revealed the presence of different peaks located at ∼2.4 eV, ∼2.7 eV and ∼3.1 eV. These plasmon modes are probably present at the local EEL spectra taken from the 0^o tilted nanocube but they are not as visible as +40^o tilted case amongst the wide plasmon peaks obtained at 0^o tilt. The same is valid for the selected area EEL spectra obtained from the -40^o tilted nanocube which reveal the presence of relatively sharp peaks at ∼2.5 eV and ∼3.1 eV. Proximal and distal modes can be associated with the energy of the plasmon peaks obtained from different corners of the -40^o tilted nanocube where the area in blue is in contact with the substrate and the area in orange is not. The plasmon peaks obtained from different tilts of the nanoframe are located at the same energies (∼1.8 eV).

5.6.2 Processing of 3D plasmonic properties

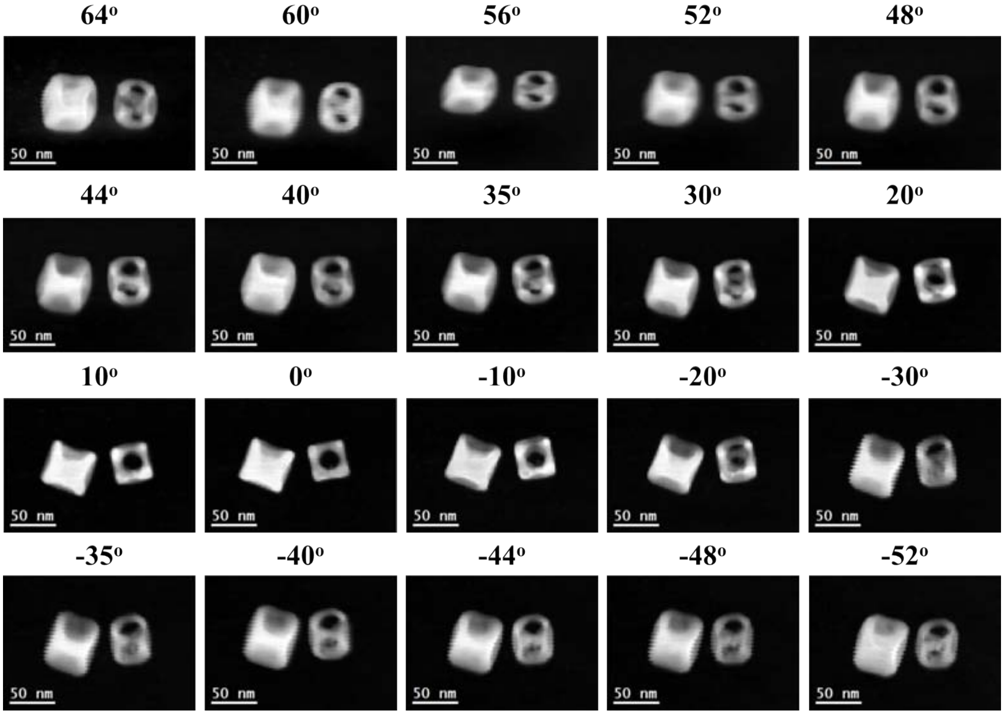

FIGURE 5.36: Series of HAADF STEM micrographs of the Ag@Au core-shell nanocube and AuAg nanoframe obtained simultaneously with the EELS SI at different tilt angles between +64^o and -52^o with different intervals.

Fig. 5.36 shows the HAADF STEM micrographs of the Ag@Au core-shell nanocube and AuAg nanoframe standing with a ∼14 nm gap obtained simultaneously with the EELS SI at different tilt angles between +64^o and -52^o with different intervals. We could obtain EELS maps for the 20 tilt angles +64^o and -52^o, where the tilt interval decreased with increasing tilt angle, i.e. 10^o up to ±30^o, 5^o between 30^o and 40^o and 4^o for tilt angles higher than ±40^o, as shown in this figure. The tilt axis was, more or less, parallel to the alignment of the two nanostructures. These STEM micrographs clearly reveals the inhomogeneously alloyed Ag@Au core-shell nanocube and voids among the faces of the AuAg nanoframe.

We have obtained 7 different components from the EELS SIs of the Ag@Au core-shell nanocube and AuAg nanoframe standing next to one another by VCA. Spectra of these 7 components and their corresponding abundance maps for selected tilt angles of +64, +52, +40, +20, 0, -20, -40 and -52 degrees are presented in Fig. 5.37. We also present the components and their corresponding abundance maps for all 20 tilt angles as separate figures in the following. Figures 5.38, 5.39, 5.40, 5.41, 5.42, 5.43 and 5.44 show the spectra and abundance maps for all tilt angles for the components I, II, III, IV, V, VI and VII, respectively.

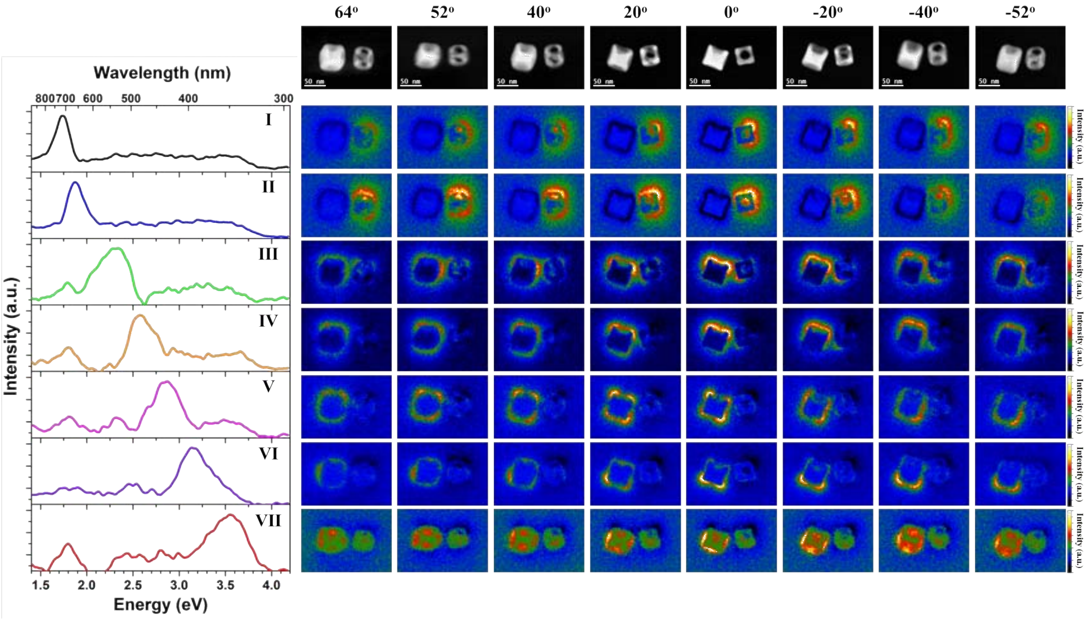

FIGURE 5.37: Spectra of 7 different components of the Ag@Au core-shell nanocube and AuAg nanoframe, obtained by VCA and their corresponding abundance maps for different tilts. Intensity of the abundance maps are normalized within each component.

As presented above, the plasmon resonances generated by the AuAg nanoframe have lower energies than those of the Ag@Au core-shell nanocube. Components I and II are located at ∼1.75 eV and ∼1.9 eV, respectively. Their abundance maps reveal that these two plasmon modes are typical LSPR modes of the hollow nanoframes being present all around the nanostructure. It should be noted that they are highly intense at some local points such as the component I has higher intensities at the upper right corner of the AuAg nanoframe, whereas the component II has higher intensities at the upper part in general as well as the void of the nanoframe. Both of the components are related to the plasmon resonances from the inner and outer parts of the nanoframe indicating the interaction between inner and outer plasmon modes of the hollow nanostructures. These two components and their distribution along the nanoframe are qualitatively similar to the plasmon modes observed for the above presented individual AuAg nanoframe (Fig. 5.22).

The component III is relatively wide peak located at ∼2.3 eV. Its abundance maps show that it is generated by the alloyed upper part of the core-shell nanocube along with the lower right corner of the hollow nanoframe. The plasmon resonances of the nanocube and nanoframe for this mode seem to be interacting with each other. Similar to the component III, component IV (located at ∼2.6 eV) is mostly related to the upper part of the core-shell nanocube with fewer contributions from the nanoframe. Abundance maps of the components V and VI reveal that these two components are two different corner plasmon modes of the core-shell nanocube, which are located at ∼2.85 eV and

~3.15 eV, respectively. Some really weak contributions from possibly Ag-rich parts of the nanoframe are observed at the abundance modes of different tilt angles for both components. The final component obtained by VCA for the Ag@Au nanocube and AuAg nanoframe couple standing with a ~14 nm separation is located at ~3.55 eV and its abundance maps reveal that this mode is the face plasmon mode of the nanocube. Interestingly, it is substantially generated by the nanoframe as well especially from the lower part of the nanoframe. It may suggest the presence of Ag-rich segregation around this part which shall be revealed more clearly after the tomographic reconstructions.

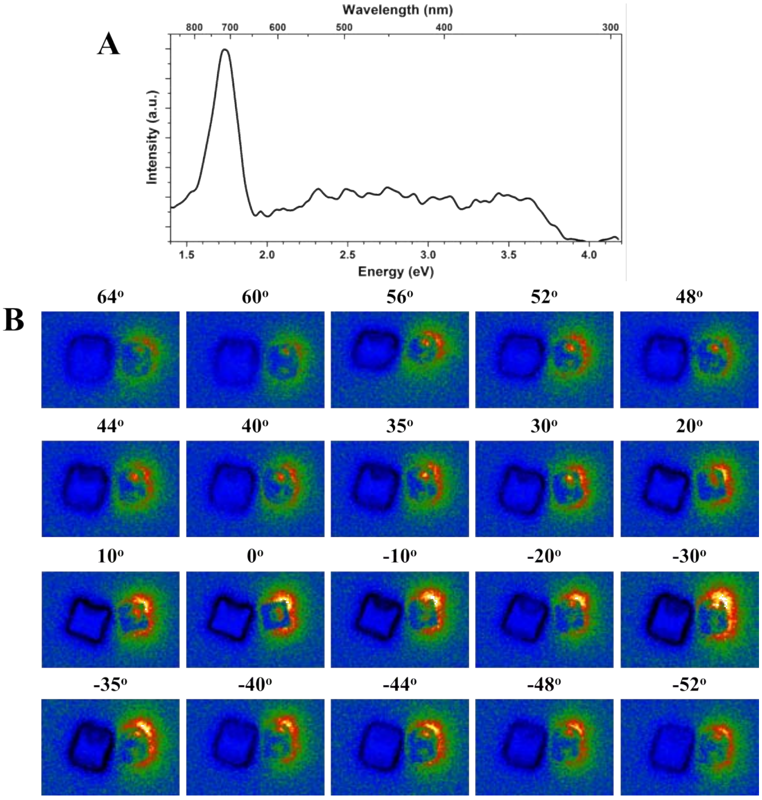

FIGURE 5.38: A. Spectrum of the component I in Fig. 5.37 and its corresponding abundance maps for all tilt angles are shown in B.

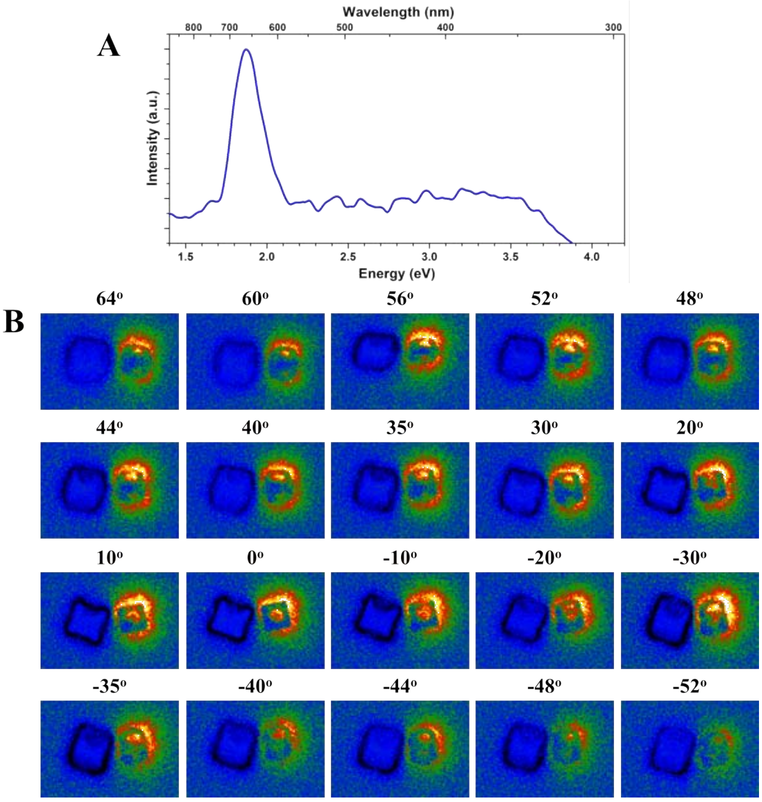

FIGURE 5.39: A. Spectrum of the component II in Fig. 5.37 and its corresponding abundance maps for all tilt angles are shown in B.

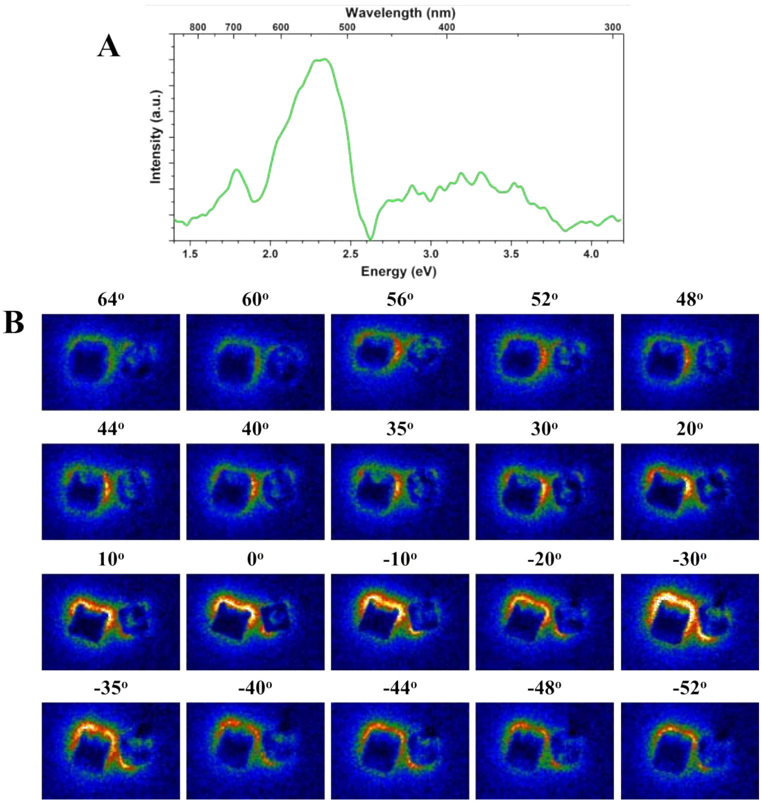

FIGURE 5.40: A. Spectrum of the component III in Fig. 5.37 and its corresponding abundance maps for all tilt angles are shown in B.

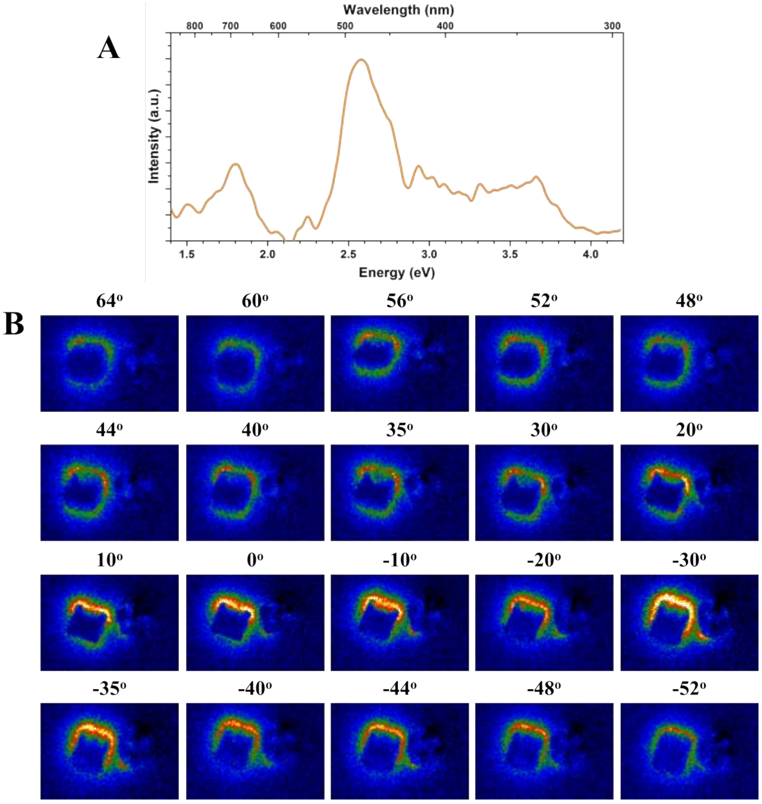

FIGURE 5.41: A. Spectrum of the component IV in Fig. 5.37 and its corresponding abundance maps for all tilt angles are shown in B.

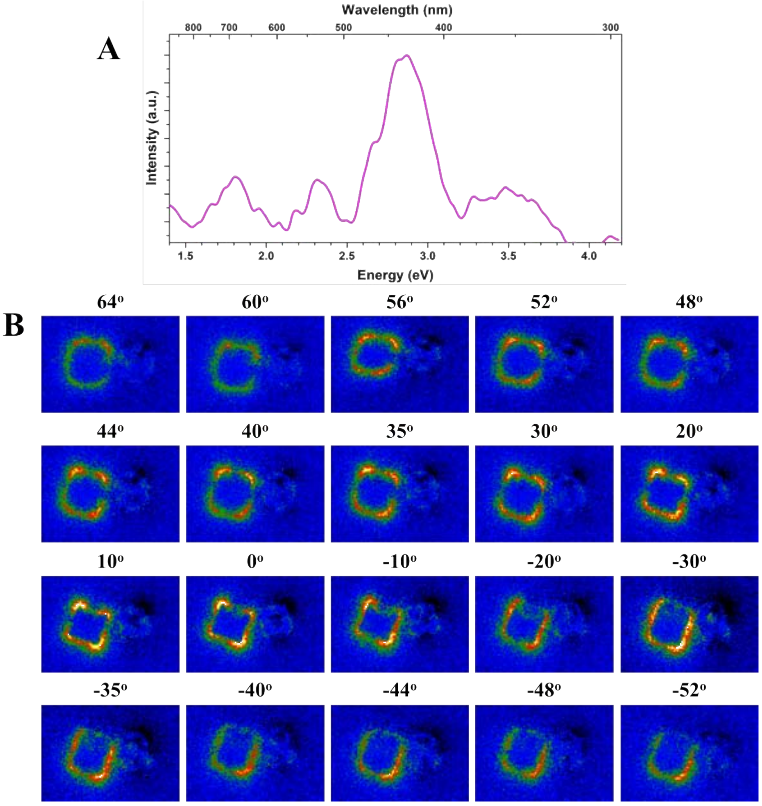

FIGURE 5.42: A. Spectrum of the component V in Fig. 5.37 and its corresponding abundance maps for all tilt angles are shown in B.

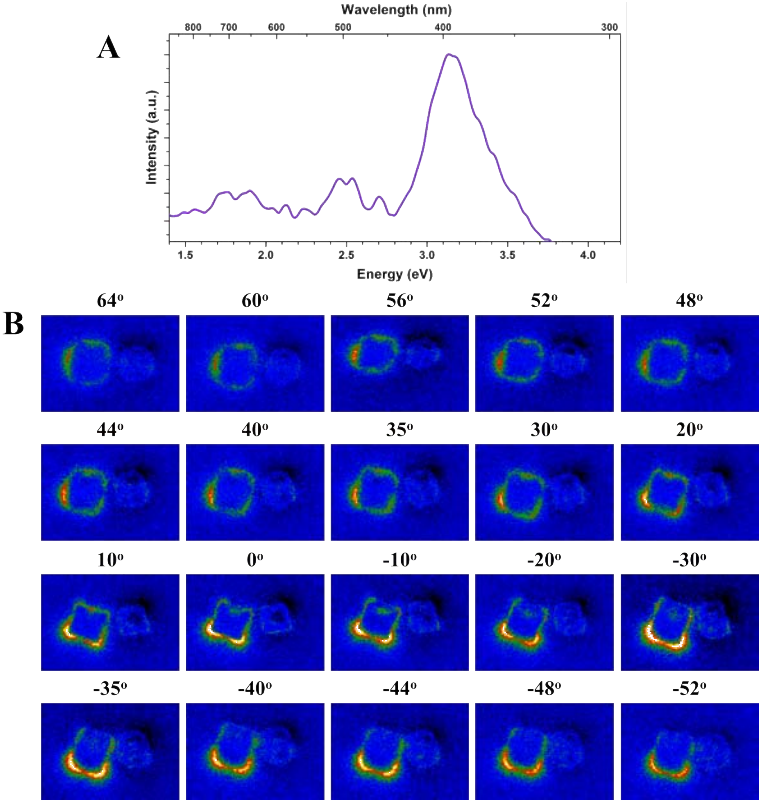

FIGURE 5.43: A. Spectrum of the component VI in Fig. 5.37 and its corresponding abundance maps for all tilt angles are shown in B.

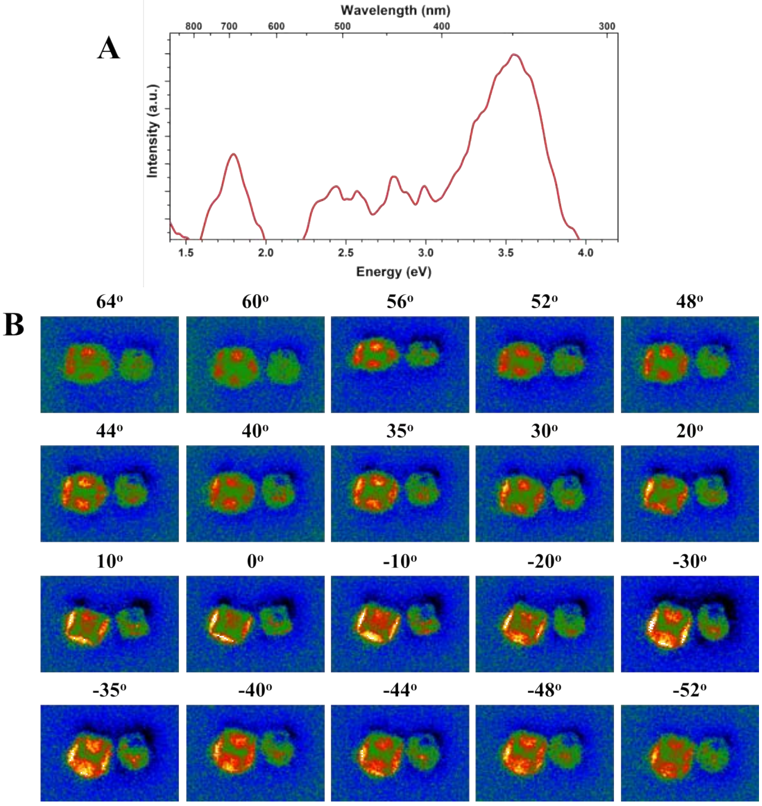

FIGURE 5.44: A. Spectrum of the component VII in Fig. 5.37 and its corresponding abundance maps for all tilt angles are shown in B.

5.7 Summary and conclusions

In this chapter, we have shown the three dimensional localized surface plasmon resonance properties of several complex cuboid AuAg nanostructures: solid Ag@Au core-shell nanocube, partially hollow AgAu nanocube and AuAg nanoframe. Moreover, we have shown the 3D LSPR properties of two nanostructures standing next to one another in order to reveal the couplings of plasmon resonances in 3D, where we have investigated two Ag@Au core-shell nanocubes with sizes standing with ∼22 nm separation and an Ag@Au core-shell nanocube and an AuAg nanoframe standing with ∼14 nm separation.

In Chapter 3 we initially studied the plasmonic properties of complex, cuboid AuAg hollow nanostructures synthesized by galvanic replacement reaction by using EELS mapping along 2D projections. It was then concluded that the local chemical and morphological differences affect the local plasmonic properties dramatically. By the nature of their synthesis process, the AuAg cuboid nanostructures are not perfectly symmetrical in morphology, as well as they may be chemically inhomogeneous. Therefore, one needs to know the 3D morphology of these chemically synthesized hollow nanostructures in order to have a complete understanding on their LSPR properties. During the previous chapters, we have studied the possible effects of chemical and morphological differences on the LSPR properties of cuboid and 1D hollow AuAg nanostructures. By doing so, we have gained valuable information about the plasmonic properties of different stages of galvanic replacement reaction from Ag nanocubes to AuAg nanoboxes/nanoframe and the influences of the local morphological differences. Moreover, we have optimized the processing routine of the EELS datasets. We have shown that the components generated by vertex component analysis have good fits with the BEM simulations, after comparing the Gaussian fitting, blind source separation and vertex component analysis during the processing of the EELS data obtained on the hollow nanobox/nanoframe and nanotube structures.

With all these previous information, we have conducted angle resolved EELS experiments for several cuboid AuAg nanostructures corresponding to the early stages of the galvanic replacement reaction. As mentioned above, we have choosen three different nanostructures of a nm solid Ag@Au core-shell nanocube, a partially hollow AgAu nanocube and an AuAg nanoframe, where we have conducted low-loss EELS maps with high tilt angles ($\sim \pm 60^o$) in order to reveal the progressing galvanic replacement reaction on the morphology, thus, the LSPR properties of AuAg nanostructures. In addition to the 3D plasmonic properties of individual nanostructures, we have shown the 3D plasmonic properties of two Ag@Au core-shell nanocubes with sizes standing with ∼22 nm separation and an Ag@Au core-shell nanocube and an AuAg nanoframe standing with ∼14 nm separation. The samples are deposited on 18 nm thick SiO_2 grids which has a 0.5

mm x 0.5 mm single window, allowing us to tilt ±60^o. The EELS SI maps are obtained by using a monochromated STEM operated at 80 kV with typical energy resolutions around 120 meV and spatial resolution between 1.2 and 2.0 nm. Due to high number of tilt series and, more importanty, e-beam induced transformation of the nanostructure morphologies after long aquisition times, we had to optimize the acquisition times to about 5 min per EELS maps. The signal-to-noise ratios of the obtained EELS data are somewhat lower than those presented in previous chapters for 2D experiments, yet they contain the necessary information to generate components related to different LSPR modes for each tilt angle. We have used spectral unmixing with VCA to process the EELS data, where we have identified individual components from different tilt angles and used the obtained spectra of the components to generate corresponding abundance maps. We have only presented plasmon maps of each component for every tilt angle, yet, tomography reconstructions of all datasets and relevant modelling studies are in progress and will be completed in the near future, due to the complexity of the processing routines and time limitations for my PhD studies.

After obtaining 3D plasmonic maps of different AuAg nanostructures, the following general conclusions can be drawn:

1- The presence of different proximal and distal plasmon modes and their distribution in 3D are shown for Ag@Au core-shell nanocubes and partially hollow AgAu nanocubes.

2- 3D HAADF STEM micrographs of the partially hollow AgAu nanocube revealed that the galvanic replacement can take place randomly in certain parts of the nanocube. 2D projection of the partially hollow AgAu nanocube at 0 degree tilt suggested a central part being hollow, which turned out to be a cylindrical void along two neighbor faces of the nanocube after 3D tilt series.

3- Such a confined void generated lower energy plasmon resonances only around the hollow part due to plasmon hybridization, whose relative intensities are strictly defined by the alignment of the hollow part with respect to the e-beam projection.

4- Homogeneous distribution of plasmon resonances in AuAg nanoframe are revealed in 3D. Along with the above mentioned partially hollow AgAu nanocube, these are the first examples of 3D plasmonic properties on hollow nanostructures.

5- The presence of bonding and anti-bonding coupling modes between two Ag@Au core-shell nanocubes standing with ∼22 nm separation is shown in 3D. Moreover, 3D plasmonic properties of an Ag@Au core-shell nanocube and an AuAg nanoframe standing with ∼14 nm separation revealed the presence of interacting plasmon resonances. To the best of our knowledge, there is no reported literature about the plasmon coupling in 3D, and first examples are shown here in the present thesis manuscript.

Chapter 6

General Conclusions and Future Work

This work presents a comprehensive investigation about the plasmonic properties of hollow AuAg nanostructures at the nanoscale by using electron energy-loss spectroscopy in monochromated STEM. We have tuned the plasmonic properties of metallic nanostructures by engineering their morphologies from solid Ag nanocubes to hollow multi-walled AuAg nanoboxes, or from Ag nanowires to novel AuAg nanotubes. The main purpose of this thesis, thus, was the correlation of the effects of local morphological and chemical variations on the plasmonic properties hollow metal nanostructures. Here, we present the general conclusions obtained during this study. Moreover, we indicate some future works on the topic, some of which are already on-going and some will be possible after certain developments.

General Conclusions

In Chapter 3, we have shown the localized surface plasmon resonance properties of several complex metal nanostructures: Ag nanocube, Ag@Au core-shell nanocube, pinholed AuAg nanobox, single-walled AuAg nanobox, AuAg nanoframe and double-walled AuAg nanobox. We have compared the results obtained by three different data processing techniques: Gaussian fitting, independent component analysis by using blind source separation algorithm and spectral unmixing via vertex component analysis. We have used BEM simulations in order to be able to better elucidate our experimental results as well as for a further discussion about the shape and environmental effects. As a proof-of-concept experiment for the enhanced plasmonic properties in the hollow nanostructures, we have conducted a sensing experiment where we have compared the response of highly sensitive spherical Au nanoparticles and single-walled AuAg nanoboxes to conjugation events with Bovine Serum Albumin (BSA) and its antibodies (anti-BSA, Ab). We have discussed the sensitivity of different Au nanostructures for the results obtained by BEM simulations, taking the universal merit of sensitivity factor into account. Thanks to the detailed experimental and computational studies presented in this chapter, we could draw the following conclusions:

- The LSPR peaks of the Ag nanocube shifted to lower energies with the Au alloying and/or increasing of void size due to both compositional and morphological effects. It was concluded that morphological changes are more dominant than the chemical modifications while determining the plasmonic properties of the nanostructures.
- The corner rounding in the experimentally investigated Ag nanocube resulted the merging of corner and edge modes and the extend of its influence was discussed throughly by using BEM simulations.

- Galvanic replacement reaction took place unevenly during the inital stage of the reaction, i.e. for the case of Ag@Au core-shell nanocubes and pinholed AuAg nanoboxes, which resulted in the local modifications of plasmonic properties.

- Rather homogeneous distribution of plasmon resonances for the single- and double-walled AuAg nanoboxes and AuAg nanoframe was observed experimentally and supported by BEM simulations for the single-walled nanobox and nanoframe.

- Interaction of inner and outer plasmon resonances in such hollow nanostructures was revealed experimentally for the first time, which was more obvious for the case of nanoframe.

- Almost perfect correlation between the experimental findings and BEM simulations was obtained for the single-walled nanobox and nanoframe.

- Among the three different processing routines, VCA provided more reliable plasmonic components.

- Single-walled AuAg nanoboxes showed 5 fold more sensitivity than the solid Au nanoparticles against conjugation events with BSA and its antibodies.

In Chapter 4, we have presented the plasmonic properties of hollow 1D nanostructures, namely a completely hollow AuAg nanotube and a hybrid (a sequence formation of solid Ag core with AuAg shell and hollow AuAg parts) AuAg nanotubes, respectively. The completely hollow AuAg nanotube had a length of 655 nm and a diameter of 84 nm with 10 nm thick walls, whereas the hybrid AuAg nanotube was 1.24 μm long and had a diameter of 89 nm. Presence of different Fabry-Perot type resonator modes and LSPR modes were revealed experimentally by using Gaussian fitting and VCA routines. BEM simulations on the 1D Ag nanostructures are conducted in order to investigate the plasmonic properties of solid and hollow 1D nanostructures and the effects of the substrate on the plasmonic properties of hollow 1D nanostructures. Finally, we have simulated an AuAg nanotube composed of 60 at.% Au and 40 at.% Ag with the same sizes as the experimentally investigated hollow AuAg nanotube. On the basis of experimental and computational results obtained in this chapter, following conlusions can be drawn:

- Presence of different Fabry-Perot type resonator modes along with LSPR modes was revealed by both Gaussian fitting and VCA routines. VCA indicated the presence of Fabry-Perot modes up to fourth order, where the first order mode was located at 0.5 eV.

- It was revealed that both Fabry-Perot and LSPR modes were present intensely inside the hollow nanotube.
- It is worth noting that the presence of a dark plasmonic breathing-like mode located at ~0.3 eV has been observed during the simulations of Ag nanowire standing in vacuum as well as some signatures suggesting its presence in the simulated AuAg nanotubes standing on the substrate.
- An accurate fit between the results obtained by VCA and BEM simulations was obtained.
- Hybrid AuAg nanotube revealed the presence of Fabry-Perot modes up to fourth order and LSPR modes distinctive to the hollow AuAg parts and solid Ag parts, including the bulk plasmon resonance of Ag.
- The presence of first order Fabry-Perot located at ~0.44 eV was revealed thanks to VCA, which could not be observed by Gaussian fitting as the background subtraction at this energy range was not possible.

In Chapter 5, we have shown the 3D LSPR properties of several complex cuboid AuAg nanostructures: solid Ag@Au core-shell nanocube, partially hollow AgAu nanocube and AuAg nanoframe. Moreover, we have shown the 3D LSPR properties of two nanostructures standing next to one another in order to reveal the couplings of plasmon resonances in 3D, where we have investigated two Ag@Au core-shell nanocubes with sizes standing with ~22 nm separation and an Ag@Au core-shell nanocube and an AuAg nanoframe standing with ~14 nm separation. The need for 3D characterization of plasmonic properties became clear in the previous chapters as the cuboid AuAg nanostructures were not perfectly symmetrical in morphology, as well as they had chemical inhomogeneities. Therefore, we have mapped the plasmonic properties at different tilt angles of $\sim \pm 60^o$ and on the basis of angle-resolved EELS maps revealing the 3D plasmonic properties of different AuAg nanostructures, the following general conclusions can be drawn:

- It was revealed that the hollow part could be randomly distributed in certain parts of the nanostructures. For instance, 2D projection of the partially hollow AgAu nanocube at 0 degree tilt suggested a central part being hollow, which turned out to be a cylindrical void along two neighbor faces of the nanocube after 3D tilt series. The plasmon resonances generated by this void were confined around the void and located at lower energies compared to those generated by solid parts.
- The presence of different proximal and distal plasmon modes and their distribution in 3D were shown for Ag@Au core-shell nanocubes and partially hollow AgAu nanocubes.

- Homogeneous distribution of plasmon resonances in AuAg nanoframe were revealed in 3D.
- The presence of bonding and anti-bonding coupling modes between two Ag@Au core-shell nanocubes standing with ∼22 nm separation was shown in 3D. Moreover, 3D plasmonic properties of an Ag@Au core-shell nanocube and an AuAg nanoframe standing with ∼14 nm separation revealed the presence of interacting plasmon resonances.

Future Work

As mentioned throughout the manuscript, some aspects of this study requires future works. Moreover, we anticipate several future directions on the basis of the conclusions obtained during this study. Here we present them in the order that they are suggested through the manuscript.

- Developments in the synthesis process are needed in order to produce AuAg nanoframes and multi-walled AuAg nanoboxes with high abundancies, as these particular nanostructures are thought to have highly enhanced sensing properties on the basis of their LSPR properties obtained by EELS, results also supported by the BEM simulations.
- Similarly, if the sequence of the solid and hollow parts in the hybrid AuAg nanotubes would be controlled with improved synthesis routines, these novel nanostructures would have many different applications as they hold the key to manipulate light over a wide range of energy, spanning over the infrared to UV regions.
- Simulations of the hybrid AuAg nanotubes are needed in order to have a better understanding about the interaction between solid and hollow parts. As these nanostructures are typically have lengths of several microns, their computation requires long processing times and high memories. We are on the process of obtaining first simulation results but a systematical study would require some more time.
- The tomographic reconstructions are needed for each component in order to reveal the 3D plasmonic properties clearly. These studies are already on-going but as they need careful processing, they will be fully obtained in the near future.
- We have reported the coupling between randomly located nanostructures. If we could be able to control the assembly of the hollow nanostructures, the geometries that would result in highly enhanced plasmonic properties could be engineered. We are planning to apply polymer-assisted self assembly processes to control the

assembly of the hollow nanoboxes presented in this study. Furthermore, if they are done directly on the TEM grids, we could obtain EELS analyses both in 2D and 3D on these coupled nanoboxes. As a result of the characterization of the plasmonic resonances with different coupling geometries, these nanostructures can be engineered specifically for desired applications.

- It is possible to create multifunctional plasmonic nanostructures by locating different nanostructures into hollow nanoboxes. We plan to extend our studies into the direction of multifunctionality. For instance, it would be possible to have magnetic resonance imaging and cancer therapy with the same magnetoplasmonic nanostructures.

Bibliography

[1] D. K. Gramotnev and S. I. Bozhevolnyi. Plasmonics beyond the diffraction limit. *Nature Photonics*, 4(2):83–91, 2010.

[2] S. A. Maier. *Plasmonics: Fundamentals and Applications*. Springer, 2007.

[3] S. A. Maier, M. L. Brongersma, P. G. Kik, S. Meltzer, A. A. G. Requicha, and H. A. Atwater. Plasmonics: A Route to Nanoscale Optical Devices. *Advanced Materials*, 13:1501–1505, 2001.

[4] E. Ozbay. Plasmonics: Merging Photonics and Electronics at Nanoscale Dimensions. *Science*, 311:189–194, 2006.

[5] M. Pelton, J. Aizpurua, and G. Bryant. Metal-nanoparticle plasmonics. *Laser and Photonics Reviews*, 2(3):136–159, 2008.

[6] S. Enoch and N. Bonod, editors. *Plasmonics: From Basics to Advanced Topics*. Springer, 2012.

[7] C. Kittel. *Introduction To Solid State Physics*. John Wiley & Sons, 8th ed. edition, 2005.

[8] J. C. Maxwell. A Dynamical Theory of the Electromagnetic Field. *Philosophical Transactions of the Royal Society of London*, 155:459–512, 1865.

[9] N. C. Lindquist. *Engineering Metallic Nanostructures for Surface Plasmon Resonance Sensing*. PhD thesis, University of Minnesota, 2010.

[10] J. J. Greffet. Introduction to Surface Plasmon Theory. In S. Enoch and N. Bonod, editors, *Plasmonics: From Basics to Advanced Topics*, chapter 4, pages 105–148. Springer, 2012.

[11] P. Drude. Zur Elektronentheorie der Metalle. *Annalen der Physik*, 306:566–613, 1900.

[12] P. Drude. Zur Elektronentheorie de Metalle: II. Teil, Galvanomagnetische und thermomagnetische Effecte. *Annalen der Physik*, 308:369–402, 1900.

[13] P. B. Johnson and R. W. Christy. Optical Constants of the Noble Metals. *Physical Review B*, 6:4370–4379, 1972.

[14] D. Pines and D. Bohm. A collective description of electron interactions: II. Collective vs individual particle aspects of the interactions. *Physical Review*, 85:338–353, 1952.

[15] J. Zenneck. Uber die Fortpflanzung ebener elektromagnetischer Wellen langs einer ebenen Leiterflache und ihre Beziehung zur drahtlosen Telegraphie. *Annalen der Physik*, 328:846–866, 1907.

[16] A. Sommerfeld. Uber die Ausbreitung der Wallen in der drahtlosen Telegraphie. *Annalen der Physik*, 333:665–736, 1909.

[17] R. H. Ritchie. Plasmo Losses of Fast Electrons in Thin Films. *Physical Review*, 106:874–881, 1957.

[18] C. J. Powell and J. B. Swan. Origin of the characteristic electron energy losses in aluminum. *Physical Review*, 115:869–875, 1959.

[19] C. J. Powell and J. B. Swan. Origin of the characteristic electron energy losses in magnesium. *Physical Review*, 116:81–83, 1959.

[20] E. A. Stern and R. A. Ferrell. Surface plasma oscillations of a degenerate electron gas. *Physical Review*, 120:130–136, 1960.

[21] D. Sarid and W. Challener. *Modern Introduction to Surface Plasmons: Theory, Mathematica Modeling, and Applications*. Cambridge, 2010.

[22] J. Aizpurua and R. Hillenbrand. Localized Surface Plasmons: Basics and Applications in Field-Enhanced Spectroscopy. In S. Enoch and N. Bonod, editors, *Plasmonics: From Basics to Advanced Topics*, chapter 5, pages 151–176. Springer, 2012.

[23] J. M. Pitarke, V. M. Silkin, E. V. Chulkov, and P. M. Echenique. Theory of surface plasmons and surface-plasmon polaritons. *Reports on Progress in Physics*, 70:1–87, 2007.

[24] G. Mie. Beitrage zur Optik truber Medien, speziell kolloidaler Metallosungen. *Annalen der Physik*, 330:377–445, 1908.

[25] H. Fröhlih. *Theory of Dielectrics: Dielectric Constant and Dielectric Loss*. Oxford, Clarendon Press, 1949.

[26] S. Hayashi and T. Okamoto. Plasmonics: visit the past to know the future. *Journal of Physics D: Applied Physics*, 45:433001, 2012.

[27] U. Kreibig and M. Vollmer. *Optical Properties of Metal Clusters.* Springer, 1995.

[28] Y. Xia and N. J. Halas. Shape-Controlled Synthesis and Surface Plasmonic Properties of Metallic Nanostructures. *MRS Bulletin*, 30:338–348, 2005.

[29] L. M. Liz-Marzan. Tailoring Surface Plasmons through the Morphology and Assembly of Metal Nanoparticles. *Langmuir*, 22:32–41, 2006.

[30] J. Zhang and L. Zhang. Nanostructures for surface plasmons. *Advances in Optics and Photonics*, 4:157, 2012.

[31] J. Lermé, H. Baida, C. Bonnet, M. Broyer, E. Cottancin, A. Crut, P. Maioli, N. Del Fatti, F. Vallee, and M. Pellarin. Size dependence of the surface plasmon resonance damping in metal nanospheres. *Journal of Physical Chemistry Letters*, 1:2922–2928, 2010.

[32] C. Sonnichsen, S. Geier, N. E. Hecker, G. von Plessen, J. Feldmann, H. Ditlbacher, B. Lamprecht, J. R. Krenn, F. R. Aussenegg, V. Z.H. Chan, J. P. Spatz, and M. Moller. Spectroscopy of single metallic nanoparticles using total internal reflection microscopy. *Applied Physics Letters*, 77:2949–2951, 2000.

[33] S. Berciaud, L. Cognet, P. Tamarat, and B. Lounis. Observation of Intrinsic Size Effects in the Optical Response of Individual Gold Nanoparticles. *Nano Letters*, 5:515, 2005.

[34] A. Sanchez-Iglesias, I. Pastoriza-Santos, J. Perez-Juste, B. Rodriguez-Gonzalez, F. J. Garcia de Abajo, and L. M. Liz-Marzan. Synthesis and Optical Properties of Gold Nanodecahedra with Size Control. *Advanced Materials*, 18:2529–2534, 2006.

[35] Y. Xiong, J. Chen, B. Wiley, Y. Xia, Y. Yin, and Z. Y. Li. Size-dependence of surface plasmon resonance and oxidation for Pd nanocubes synthesized via a seed etching process. *Nano Letters*, 5:1237–1242, 2005.

[36] B. J. Wiley, Y. Chen, J. M. McLellan, Y. Xiong, Z. Y. Li, D. Ginger, and Y. Xia. Synthesis and optical properties of silver nanobars and nanorice. *Nano Letters*, 7: 1032–1036, 2007.

[37] H. Chen, X. Kou, Z. Yang, W. Ni, and J. Wang. Shape- and size-dependent refractive index sensitivity of gold nanoparticles. *Langmuir*, 24(31):5233–5237, 2008.

[38] E. Ringe, J. M. McMahon, K. Sohn, C. Cobley, Y. Xia, J. Huang, G. C. Schatz, L. D. Marks, and R. P. Van Duyne. Unraveling the effects of size, composition, and substrate on the localized surface plasmon resonance frequencies of gold and silver

nanocubes: A systematic single-particle approach. *Journal of Physical Chemistry C*, 114:12511–12516, 2010.

[39] X. Ye, L. Jin, H. Caglayan, J. Chen, G. Xing, C. Zheng, V. Doan-Nguyen, Y. Kang, N. Engheta, C. R. Kagan, and C. B. Murray. Improved Size-Tunable Synthesis of Monodisperse Gold Nanorods through the Use of Aromatic Additives. *ACS Nano*, 6:2804–2817, 2012.

[40] Y. Fang, W. S. Chang, B. Willingham, P. Swanglap, S. Dominguez-Medina, and S. Link. Plasmon emission quantum yield of single gold nanorods as a function of aspect ratio. *ACS Nano*, 6, 2012.

[41] X. Liu, L. Li, Y. Yang, Y. Yin, and C. Gao. One-step growth of triangular silver nanoplates with predictable sizes on a large scale. *Nanoscale*, 6:4513–6, 2014.

[42] M. R. Goncalves. Plasmonic nanoparticles: fabrication, simulation and experiments. *Journal of Physics D: Applied Physics*, 47:213001, 2014.

[43] S. Link and M. A. El-Sayed. Spectral Properties and Relaxation Dynamics of Surface Plasmon Electronic Oscillations in Gold and Silver Nanodots and Nanorods. *Journal of Physical Chemistry B*, 103:8410–8426, 1999.

[44] P. Guo, D. Sikdar, X. Huang, K. J. Si, W. Xiong, S. Gong, L. W. Yap, M. Premaratne, and W. Cheng. Plasmonic coreshell nanoparticles for SERS detection of the pesticide thiram: size- and shape-dependent Raman enhancement. *Nanoscale*, 7:2862–2868, 2015.

[45] L. Vigderman, B. P. Khanal, and E. R. Zubarev. Functional gold nanorods: Synthesis, self-assembly, and sensing applications. *Advanced Materials*, 24:4811–4841, 2012.

[46] J. J. Mock, M. Barbic, D. R. Smith, D. A. Schultz, and S. Schultz. Shape effects in plasmon resonance of individual colloidal silver nanoparticles. *The Journal of Chemical Physics*, 116:6755, 2002.

[47] K. L. Kelly, E. Coronado, L. L. Zhao, and G. C. Schatz. The Optical Properties of Metal Nanoparticles: The Influence of Size, Shape, and Dielectric Environment. *Journal of Physical Chemistry B*, 107:668–677, 2003.

[48] Y. Sun and Y. Xia. Gold and silver nanoparticles: a class of chromophores with colors tunable in the range from 400 to 750 nm. *The Analyst*, 128:686–691, 2003.

[49] B. Wiley, Y. Sun, B. Mayers, and Y. Xia. Shape-controlled synthesis of metal nanostructures: The case of silver. *Chemistry - A European Journal*, 11:454–463, 2005.

[50] B. Wiley, Y. Sun, J. Chen, H. Cang, Z. Y. Li, X. Li, and Y. Xia. Shape-Controlled Synthesis of Silver and Gold Nanostructures. *MRS Bulletin*, 30:356–361, 2005.

[51] B. J. Wiley, S. H. Im, Z. Y. Li, J. McLellen, A. Siekkinen, and Y. Xia. Maneuvering the Surface Plasmon Resonance of Silver Nanostructures through Shape-Controlled Synthesis. *Journal Of Physical Chemistry B*, 110:15666–15675, 2006.

[52] B. Wiley, Y. Sun, and Y. Xia. Synthesis of silver nanostructures with controlled shapes and properties. *Accounts of Chemical Research*, 40:1067–1076, 2007.

[53] C. Noguez. Surface Plasmons on Metal Nanoparticles: The Influence of Shape and Physical Environment. *Journal of Physical Chemistry C*, 111:3806–3819, 2007.

[54] C. L. Nehl and J. H. Hafner. Shape-dependent plasmon resonances of gold nanoparticles. *Journal of Materials Chemistry*, 18:2415, 2008.

[55] A. Gonzalez. Optical properties of elongated noble metal nanoparticles. *The Journal of Physical Chemistry C*, 112:7356–7362, 2008.

[56] H. Chen, L. Shao, K. C. Woo, T. Ming, H. Q. Lin, and J. Wang. Shape-dependent refractive index sensitivities of gold nanocrystals with the same plasmon resonance wavelength. *Journal of Physical Chemistry C*, 113:17691–17697, 2009.

[57] M. Eguchi, D. Mitsui, H. Lun Wu, R. Sato, and T. Teranishi. Simple reductant concentration-dependent shape control of polyhedral gold nanoparticles and their plasmonic properties. *Langmuir*, 28:9021–9026, 2012.

[58] P. M. Tomchuk and D. V. Butenko. The nanoparticle shape's effect on the light scattering cross-section. *Surface Science*, 606:1892–1898, 2012.

[59] J. Qian, C. X. Liu, W. D. Wang, J. Chen, Y. Dong Li, J. J. Xu, and Q. Sun. Effect of Edge Rounding on the Extinction Properties of Hollow Metal Nanoparticles. *Plasmonics*, 8:955–962, 2013.

[60] S. Lal, S. Link, and N. J/ Halas. Nano-optics from sensing to waveguiding. *Nature Photonics*, 1:641–648, 2007.

[61] C. M. Cobley and Y. Xia. Engineering the properties of metal nanostructures via galvanic replacement reactions. *Materials Science and Engineering R: Reports*, 70: 44–62, 2010.

[62] B. K. Juluri, J. Huang, and L. Jensen. Extinction, Scattering and Absorption Efficiencies of Single and Multilayer Nanoparticles. *https://nanohub.org/resources/8228*, 2010.

[63] E. Prodan, C. Radloff, N. J. Halas, and P. Nordlander. A hybridization model for the plasmon response of complex nanostructures. *Science*, 302(2003):419–422, 2003.

[64] V. Amendola, O. M. Bakr, and F. Stellacci. A study of the surface plasmon resonance of silver nanoparticles by the discrete dipole approximation method: Effect of shape, size, structure, and assembly. *Plasmonics*, 5:85–97, 2010.

[65] S. E. Skrabalak, L. Au, X. Li, and Y. Xia. Facile synthesis of Ag nanocubes and Au nanocages. *Nature Protocols*, 2:2182–2190, 2007.

[66] S. E. Skrabalak, J. Chen, Y. Sun, X. Lu, L. Au, C. M. Cobley, and Y. Xia. Gold nanocages: Synthesis, properties, and applications. *Accounts of Chemical Research*, 41:1587–1595, 2008.

[67] M. A. Mahmoud and M. A. El-Sayed. Gold nanoframes: Very high surface plasmon fields and excellent near-infrared sensors. *Journal of the American Chemical Society*, 132:12704–12710, 2010.

[68] Y. Xia, W. Li, C. M. Cobley, J. Chen, X. Xia, Q. Zhang, M. Yang, E. C. Cho, and P. K. Brown. Gold Nanocages: From Synthesis to Theranostic Applications. *Accounts of Chemical Research*, 44:914–924, 2011.

[69] E. Gonzalez, J. Arbiol, and V. F. Puntes. Carving at the Nanoscale: Sequential Galvanic Exchange and Kirkendall Growth at Room Temperature. *Science*, 334: 1377–1380, 2011.

[70] S. Link, Z. L. Wang, and M. A. El-Sayed. Alloy Formation of Gold-Silver Nanoparticles and the Dependence of the Plasmon Absorption on Their Composition. *The Journal of Physical Chemistry B*, 103:3529–3533, 1999.

[71] M. P. Mallin and C. J. Murphy. Solution-Phase Synthesis of Sub-10 nm Au-Ag Alloy Nanoparticles. *Nano Letters*, 11:1235–1237, 2002.

[72] K. S. Lee and M. A. El-sayed. Gold and Silver Nanoparticles in Sensing and Imaging : Sensitivity of Plasmon Response to Size , Shape , and Metal Composition Gold and Silver Nanoparticles in Sensing and Imaging : Sensitivity of Plasmon Response to Size , Shape , and Metal Composition. *Journal of Physical Chemistry B*, 110:19220–19225, 2006.

[73] Q. Zhang, J. Y. Lee, J. Yang, C. Boothroyd, and J. Zhang. Size and composition tunable AgAu alloy nanoparticles by replacement reactions. *Nanotechnology*, 18: 245605, 2007.

[74] R. Kuladeep, L. Jyothi, K. S. Alee, K. L. N. Deepak, and D. N. Rao. Laser-assisted synthesis of Au-Ag alloy nanoparticles with tunable surface plasmon resonance frequency. *Optical Materials Express*, 2:230–234, 2012.

[75] C. J. Desantis, R. G. Weiner, A. Radmilovic, M. M. Bower, and S. E. Skrabalak. Seeding bimetallic nanostructures as a new class of plasmonic colloids. *Journal of Physical Chemistry Letters*, 4:3072–3082, 2013.

[76] J. F. Gomes, A. C. Garcia, C. Pires, E. B. Ferreira, R. Q. Albuquerque, G. Tremiliosi-Filho, and L. H. S. Gasparotto. Impact of the AuAg NPs Composition on Their Structure and Properties: A Theoretical and Experimental Investigation. *The Journal of Physical Chemistry C*, 118:28868–28875, 2014.

[77] O. Peña Rodriguez, M. Caro, A. Rivera, J. Olivares, J. M. Perlado, and A. Caro. Optical properties of Au-Ag alloys: An ellipsometric study. *Optical Materials Express*, 4:403, 2014.

[78] I. Papagiannouli, P. Aloukos, D. Rioux, M. Meunier, and S. Couris. Effect of the Composition on the Nonlinear Optical Response of AuxAg1-x Nano-Alloys. *The Journal of Physical Chemistry C*, 119:6861–6872, 2015.

[79] S. Liu, G. Chen, P. N. Prasad, and M. T. Swihart. Synthesis of Monodisperse Au, Ag, and Au-Ag Alloy Nanoparticles with Tunable Size and Surface Plasmon Resonance Frequency. *Chemistry of Materials*, 23:4098–4101, 2011.

[80] K. Torigoe, Y. Nakajima, and K. Esumi. Preparation and Characterization of Colloidal Silver-Platinum Alloys. *Journal of Physical Chemistry*, 97:8304–8309, 1993.

[81] P. Mulvaney. Surface Plasmon Spectroscopy of Nanosized Metal Particles. *Langmuir*, 12:788–800, 1996.

[82] B. Sepúlveda, P. C. Angelomé, L. M. Lechuga, and L. M. Liz-Marzán. LSPR-based nanobiosensors. *Nano Today*, 4:244–251, 2009.

[83] J. N. Anker, W. P. Hall, O. Lyandres, N. C. Shah, J. Zhao, and R. P. Van Duyne. Biosensing with plasmonic nanosensors. *Nature Materials*, 7:442–453, 2008.

[84] J. Zhao, X. Zhang, C. R. Yonzon, A. J. Haes, and R. P. Van Duyne. Localized surface plasmon resonance biosensors. *Nanomedicine*, 1:219–228, 2006.

[85] M. M. Miller and A. A. Lazarides. Sensitivity of metal nanoparticle plasmon resonance band position to the dielectric environment as observed in scattering. *Journal of Optics A: Pure and Applied Optics*, 8:S239–S249, 2006.

[86] K. C. Vernon, A. M. Funston, C. Novo, D. E. Gómez, P. Mulvaney, and T. J. Davis. Influence of particle-substrate interaction on localized plasmon resonances. *Nano Letters*, 10:2080–2086, 2010.

[87] P. Das and T. K. Chini. Substrate Induced Symmetry Breaking in Penta-twinned Gold Nanorod Probed by Free Electron Impact. *The Journal of Physical Chemistry C*, 118:26284–26291, 2014.

[88] P.o Albella, B. Garcia-Cueto, F. González, F. Moreno, P. C. Wu, T. H. Kim, A. Brown, Y. Yang, H. O. Everitt, and G. Videen. Shape matters: Plasmonic nanoparticle shape enhances interaction with dielectric substrate. *Nano Letters*, 11:3531–3537, 2011.

[89] A. Crut, P. Maioli, N. Del Fatti, and F. Vallee. Optical absorption and scattering spectroscopies of single nano-objects. *Chemical Society Reviews*, 43:3921–56, 2014.

[90] O. Nicoletti, F. de la Peña, R. K. Leary, D. J. Holland, C. Ducati, and P. A. Midgley. Three-dimensional imaging of localized surface plasmon resonances of metal nanoparticles. *Nature*, 502:80–4, 2013.

[91] S. Zhang, K. Bao, N. J. Halas, H. Xu, and P. Nordlander. Substrate-induced Fano resonances of a plasmonic nanocube: A route to increased-sensitivity localized surface plasmon resonance sensors revealed. *Nano Letters*, 11:1657–1663, 2011.

[92] W. Li, I. Kanyo, C. H. Kuo, S. Thanneeru, and J. He. pH-programmable self-assembly of plasmonic nanoparticles: hydrophobic interaction versus electrostatic repulsion. *Nanoscale*, 7:956–964, 2015.

[93] N. J. Halas, S. Lal, W. S. Chang, S. Link, and P. Nordlander. Plasmons in strongly coupled metallic nanostructures. *Chemical Reviews*, 111:3913–3961, 2011.

[94] W. Rechberger, A. Hohenau, A. Leitner, J. R. Krenn, B. Lamprecht, and F. R. Aussenegg. Optical properties of two interacting gold nanoparticles. *Optics Communications*, 220:137–141, 2003.

[95] C. Sonnichsen, B. M. Reinhard, J. Liphardt, and A. P. Alivisatos. A molecular ruler based on plasmon coupling of single gold and silver nanoparticles. *Nature Biotechnology*, 23:741–745, 2005.

[96] P. K. Jain, W. Huang, and M. A. El-Sayed. On the universal scaling behavior of the distance decay of plasmon coupling in metal nanoparticle pairs: A plasmon ruler equation. *Nano Letters*, 7:2080–2088, 2007.

[97] S. K. Ghosh and T. Pal. Interparticle Coupling Effect on the Surface Plasmon Resonance of Gold Nanoparticles: From Theory to Applications. *Chemical Reviews*, 107:4797–4862, 2007.

[98] P. K. Jain and M. A. El-Sayed. Surface plasmon coupling and its universal size scaling in metal nanostructures of complex geometry: Elongated particle pairs and nanosphere trimers. *Journal of Physical Chemistry C*, 112:4954–4960, 2008.

[99] P. K. Jain and M. A. El-Sayed. Noble metal nanoparticle pairs: Effect of medium for enhanced nanosensing. *Nano Letters*, 8:4347–4352, 2008.

[100] F. J. Garcia De Abajo. Nonlocal effects in the plasmons of strongly interacting nanoparticles, dimers, and waveguides. *Journal of Physical Chemistry C*, 112: 17983–17987, 2008.

[101] S. S. Aćimović, M. P. Kreuzer, M. U. González, and R. Quidant. Plasmon near-field coupling in metal dimers as a step toward single-molecule sensing. *ACS Nano*, 3:1231–1237, 2009.

[102] P. K. Jain and M. A. El-Sayed. Plasmonic coupling in noble metal nanostructures. *Chemical Physics Letters*, 487:153–164, 2010.

[103] L. Shao, K. C. Woo, H. Chen, Z. Jin, J. Wang, and H. Q. Lin. Angle- and Energy-Resolved Plasmon Couplings in Gold Nanorod Dimers. *ACS Nano*, 3053:3062, 2010.

[104] N. Grillet, D. Manchon, F. Bertorelle, C. Bonnet, M. Broyer, E. Cottancin, J. Lermé, M. Hillenkamp, and M. Pellarin. Plasmon coupling in silver nanocube dimers: Resonance splitting induced by edge rounding. *ACS Nano*, 5(12):9450–9462, 2011.

[105] S. Dodson, M. Haggui, R. Bachelot, J. Plain, S. Li, and Q. Xiong. Optimizing electromagnetic hotspots in plasmonic bowtie nanoantennae. *Journal of Physical Chemistry Letters*, 4:496–501, 2013.

[106] J. A. Scholl, A. Garcia-Etxarri, A. L. Koh, and J. A. Dionne. Observation of quantum tunneling between two plasmonic nanoparticles. *Nano Letters*, 13:564–569, 2013.

[107] S. F. Tan, L. Wu, J. K. W. Yang, P. Bai, M. Bosman, and C. A. Nijhuis. Quantum Plasmon Resonances Controlled by Molecular Tunnel Junctions. *Science*, 343: 1496–1499, 2014.

[108] E. Prodan and P. Nordlander. Plasmon hybridization in spherical nanoparticles. *Journal of Chemical Physics*, 120:5444–5454, 2004.

[109] P. Nordlander, C. Oubre, E. Prodan, K. Li, and M. I. Stockman. Plasmon hybridization in nanoparticle dimers. *Nano Letters*, 4:899–903, 2004.

[110] P. Nordlander and E. Prodan. Plasmon hybridization in nanoparticles near metallic surfaces. *Nano Letters*, 4:2209–2213, 2004.

[111] S. C. Yang, H. Kobori, C. L. He, M. H. Lin, C. Hung-Ying, C. Li, M. Kanehara, T. Teranishi, and S. Gwo. Plasmon hybridization in individual gold nanocrystal dimers: Direct observation of bright and dark modes. *Nano Letters*, 10:632–637, 2010.

[112] L. S. Slaughter, Y. Wu, B. A Willingham, P. Nordlander, and S. Link. Effects of symmetry breaking and conductive contact on the plasmon coupling in gold nanorod dimers. *ACS Nano*, 4:4657–4666, 2010.

[113] D. W. Brandl, C. Oubre, and P. Nordlander. Plasmon hybridization in nanoshell dimers. *The Journal of Chemical Physics*, 123:24701, 2005.

[114] P. K. Jain and M. A. El-Sayed. Universal Scaling of Plasmon Coupling in Metal Nanostructures : Extension from Particle Pairs to Nanoshells. *Nano Letters*, 7: 2854–2858, 2007.

[115] E. Prodan and P. Nordlander. Structural tunability of the plasmon resonances in metallic nanoshells. *Nano Letters*, 3:543–547, 2003.

[116] N. Halas. Playing with Plasmons: Tuning the Optical Resonant Properties of Metallic Nanoshells. *MRS Bulletin*, 30:362–367, 2005.

[117] E. Prodan, P. Nordlander, and N. J. Halas. Electronic Structure and Optical Properties of Gold Nanoshells. *Nano Letters*, 3:1411–1415, 2003.

[118] C. Oubre and P. Nordlander. Optical Properties of Metallodielectric Nanostructures Calculated Using the Finite Difference Time Domain Method. *Journal of Physical Chemistry B*, 108:17740–17747, 2004.

[119] V. Kulkarni, E. Prodan, and P. Nordlander. Quantum plasmonics: Optical properties of a nanomatryushka. *Nano Letters*, 13:5873–5879, 2013.

[120] P. Bharadwaj, B. Deutsch, and L. Novotny. Optical Antennas. *Advances in Optics and Photonics*, 1:438, 2009.

[121] L. Novotny and N. van Hulst. Antennas for light. *Nature Photonics*, 5:83–90, 2011.

[122] A. I. Denisyuk, G. Adamo, K. F. MacDonald, J. Edgar, M. D. Arnold, V. Myroshnychenko, M. J. Ford, F Javier García De Abajo, and N. I. Zheludev. Transmitting hertzian optical nanoantenna with free-electron feed. *Nano Letters*, 10:3250–3252, 2010.

[123] V. Giannini, A. I. Fernández-Domínguez, S. C. Heck, and S. A. Maier. Plasmonic nanoantennas: Fundamentals and their use in controlling the radiative properties of nanoemitters. *Chemical Reviews*, 111:3888–3912, 2011.

[124] T. Hanke, J. Cesar, V. Knittel, A. Trügler, U. Hohenester, A. Leitenstorfer, and R. Bratschitsch. Tailoring spatiotemporal light confinement in single plasmonic nanoantennas. *Nano Letters*, 12:992–996, 2012.

[125] T. Coenen, E. J. R. Vesseur, and A. Polman. Deep subwavelength spatial characterization of angular emission from single-crystal au plasmonic ridge nanoantennas. *ACS Nano*, 6:1742–1750, 2012.

[126] K. M. Mayer and J. H. Hafner. Localized surface plasmon resonance sensors. *Chemical Reviews*, 111:3828–3857, 2011.

[127] A. J. Haes, C. L. Haynes, A. D. McFarland, G. C. Schatz, R. P. Van Duyne, and S. Zou. Plasmonic Materials for Surface-Enhanced Sensing and Spectroscopy. *MRS Bulletin*, 30:368–375, 2005.

[128] H. A. Atwater and A. Polman. Plasmonics for improved photovoltaic devices. *Nature Materials*, 9:205–213, 2010.

[129] N. Fang, H. Lee, C. Sun, and X. Zhang. Sub-Diffraction-Limited Optical Imaging with a Silver Superlens. *Science*, 308:534–538, 2005.

[130] V. J. Sorger and X. Zhang. Spotlight on plasmon lasers. *Science*, 333:709–710, 2011.

[131] V. M. Shalaev. Optical negative-index metamaterials. *Nature Photonics*, 1:41–48, 2007.

[132] D. E. Chang, A. S. Sø rensen, P. R. Hemmer, and M. D. Lukin. Quantum Optics with Surface Plasmons. *Physical Review Letters*, 97:053002, 2006.

[133] M. E. Stewart, C. R. Anderton, L. B. Thompson, J. Maria, S. K. Gray, J. A. Rogers, and R. G. Nuzzo. Nanostructured plasmonic sensors. *Chemical Reviews*, 108:494–521, 2008.

[134] J. J. Storhoff, A. D. Lucas, V. Garimella, Y. P. Bao, and U. R. Müller. Homogeneous detection of unamplified genomic DNA sequences based on colorimetric scatter of gold nanoparticle probes. *Nature Biotechnology*, 22:883–887, 2004.

[135] J. M. Nam, S. I. Stoeva, and C. A. Mirkin. Bio-Bar-Code-Based DNA Detection with PCR-like Sensitivity. *Journal of the American Chemical Society*, 126:5932–5933, 2004.

[136] P. Alivisatos. The use of nanocrystals in biological detection. *Nature Biotechnology*, 22:47–52, 2004.

[137] S. I. Stoeva, J. S. Lee, J. E. Smith, S. T. Rosen, and C. A. Mirkin. Multiplexed detection of protein cancer markers with biobarcoded nanoparticle probes. *Journal of the American Chemical Society*, 128:8378–8379, 2006.

[138] M. M. C. Cheng, G. Cuda, Y. L. Bunimovich, M. Gaspari, J. R. Heath, H. D. Hill, C. A. Mirkin, a. J. Nijdam, R. Terracciano, T. Thundat, and M. Ferrari. Nanotechnologies for biomolecular detection and medical diagnostics. *Current Opinion in Chemical Biology*, 10:11–19, 2006.

[139] M. A. Mahmoud, B. Snyder, and M. A. El-Sayed. Surface Plasmon Fields and Coupling in the Hollow Gold Nanoparticles and Surface-Enhanced Raman Spectroscopy. Theory and Experiment . *The Journal of Physical Chemistry C*, 114: 7436–7443, 2010.

[140] M. A. Mahmoud, D. O'Neil, and M. A. El-Sayed. Hollow and solid metallic nanoparticles in sensing and in nanocatalysis. *Chemistry of Materials*, 26:44–58, 2014.

[141] Y. Sun and Y. Xia. Increased sensitivity of surface plasmon resonance of gold nanoshells compared to that of gold solid colloids in response to environmental changes. *Analytical Chemistry*, 74:5297–5305, 2002.

[142] M. Fleischmann, P. J. Hendra, and A. J. McQuillan. Raman spectra of pyridine adsorbed at a silver electrode. *Chemical Physics Letters*, 26:163–166, 1974.

[143] D. L. Jeanmaire and R. P. Van Duyne. Surface raman spectroelectrochemistry Part I. Heterocyclic, Aromatic, and Aliphatic Amines Adsorbed on the Anodized Silver Electrode. *Journal of Electroanalytical Chemistry and Interfacial Electrochemistry*, 84:1–20, 1977.

[144] M. G. Albrecht and J. A. Creighton. Anomalously Intense Raman Spectra of Pyridine at a Silver Electrode. *Journal of the American Chemical Society*, 99: 5215–5217, 1977.

[145] P. L. Stiles, J. A. Dieringer, N. C. Shah, and R. P. Van Duyne. Surface-enhanced Raman spectroscopy. *Annual Review of Analytical Chemistry*, 1:601–626, 2008.

[146] S. Nie and S. R. Emory. Probing Single Molecules and Single Nanoparticles by Surface-Enhanced Raman Scattering. *Science*, 275:1102–1106, 1997.

[147] K. Kneipp, Y. Wang, H. Kneipp, L. T. Perelman, I. Itzkan, R. R. Dasari, and M. S. Feld. Single molecule detection using surface-enhanced Raman scattering (SERS). *Physical Review Letters*, 78:1667–1670, 1997.

[148] A. M. Michaels, M. Nirmal, and L. E. Brus. Surface Enhanced Raman Spectroscopy of Individual Rhodamine 6G Molecule on Large Ag Nanocrystals. *Journal of American Chemical Society*, 121:9932–9939, 1999.

[149] H. X. Xu, E. J. Bjerneld, M. Käll, and L. Börjesson. Spectroscopy of single hemoglobin molecules by surface enhanced Raman scattering. *Physical Review Letters*, 83:4357–4360, 1999.

[150] E. J. Blackie, E. C. Le Ru, and P. G. Etchegoin. Single-molecule surface-enhanced raman spectroscopy of nonresonant molecules. *Journal of the American Chemical Society*, 131:14466–14472, 2009.

[151] N. Mirsaleh-Kohan, V. Iberi, P. D. Simmons, N. W. Bigelow, A. Vaschillo, M. M. Rowland, M. D. Best, S. J. Pennycook, D. J. Masiello, B. S. Guiton, and J. P. Camden. Single-Molecule Surface-Enhanced Raman Scattering : Can STEM /. *Journal of Physical Chemistry C*, 3:2303–2309, 2012.

[152] X. Qian, X. H. Peng, D. O. Ansari, Q. Yin-Goen, G. Z. Chen, D. M. Shin, L. Yang, A. N. Young, M. D. Wang, and S. Nie. In vivo tumor targeting and spectroscopic detection with surface-enhanced Raman nanoparticle tags. *Nature Biotechnology*, 26:83–90, 2008.

[153] R. C. Maher, S. A. Maier, L. F. Cohen, L. Koh, A. Laromaine, J. A. G. Dick, and M. M. Stevens. Exploiting SERS hot spots for disease-specific enzyme detection. *Journal of Physical Chemistry C*, 114:7231–7235, 2010.

[154] L. Xu, W. Yan, W. Ma, H. Kuang, X. Wu, L. Liu, Y. Zhao, L. Wang, and C. Xu. SERS Encoded Silver Pyramids for Attomolar Detection of Multiplexed Disease Biomarkers. *Advanced Materials*, 27:1706–1711, 2015.

[155] K. Kneipp, A. S. Haka, H. Kneipp, K. Badizadegan, N. Yoshizawa, C. Boone, K. E. Shafer-Peltier, J. T. Motz, R. R. Dasari, and M. S. Feld. Surface-Enhanced Raman Spectroscopy in Single Living Cells Using Gold Nanoparticles. *Applied Spectroscopy*, 56:150–154, 2002.

[156] R. Zhang, Y. Zhang, Z. C. Dong, S. Jiang, C. Zhang, L. G. Chen, L. Zhang, Y. Liao, J. Aizpurua, Y. Luo, J. L. Yang, and J. G. Hou. Chemical mapping of a single molecule by plasmon-enhanced Raman scattering. *Nature*, 498:82–6, 2013.

[157] S. Pillai and M. A. Green. Plasmonics for photovoltaic applications. *Solar Energy Materials and Solar Cells*, 94:1481–1486, 2010.

[158] K. R. Catchpole and A. Polman. Plasmonic solar cells. *Optics Express*, 16:21793–21800, 2008.

[159] S. Pillai, K. R. Catchpole, T. Trupke, and M. A. Green. Surface plasmon enhanced silicon solar cells. *Journal of Applied Physics*, 101:093105, 2007.

[160] F. J. Beck, A. Polman, and K. R. Catchpole. Tunable light trapping for solar cells using localized surface plasmons. *Journal of Applied Physics*, 105:114310, 2009.

[161] K. Nakayama, K. Tanabe, and H. A. Atwater. Plasmonic nanoparticle enhanced light absorption in GaAs solar cells. *Applied Physics Letters*, 93:121904, 2008.

[162] R. B. Dunbar, H. C. Hesse, D. S. Lembke, and L. Schmidt-Mende. Light-trapping plasmonic nanovoid arrays. *Physical Review B*, 85:035501, 2012.

[163] Q. Gan, F. J. Bartoli, and Z. H. Kafafi. Plasmonic-enhanced organic photovoltaics: Breaking the 10% efficiency barrier. *Advanced Materials*, 25:2385–2396, 2013.

[164] A. J. Morfa, K. L. Rowlen, T. H. Reilly, M. J. Romero, and J. Van De Lagemaat. Plasmon-enhanced solar energy conversion in organic bulk heterojunction photovoltaics. *Applied Physics Letters*, 92:013504, 2008.

[165] C. H. Chou and F. C. Chen. Plasmonic nanostructures for light trapping in organic photovoltaic devices. *Nanoscale*, 6:8444–8458, 2014.

[166] N. Zhou, V. Lopez-Puente, Q. Wang, L. Polavarapu, I. Pastoriza-Santos, and Q. H. Xu. Plasmon-enhanced light harvesting: applications in enhanced photocatalysis, photodynamic therapy and photovoltaics. *RSC Advances*, 5:29076–29097, 2015.

[167] C. E. Petoukhoff, Z. Shen, M. Jain, A. M. Chang, and D. M. O'Carroll. Plasmonic electrodes for bulk- heterojunction organic photovoltaics : a review. *Journal of Photonics for Energy*, 5:057002, 2015.

[168] J. L. Wu, F. C. Chen, Y. S. Hsiao, F. C. Chien, P. Chen, C. H. Kuo, M. H. Huang, and C. S. Hsu. Surface Plasmonic Effects of Metallic Nanoparticles on the Performance of Polymer Bulk Heterojunction Solar Cells. *ACS Nano*, 5:959–967, 2011.

[169] L. Gao, R. Liu, F. Gao, Y. Wang, X. Jiang, and X. Gao. Plasmon-mediated generation of reactive oxygen species from near-infrared light excited gold nanocages for photodynamic therapy in vitro. *ACS Nano*, 8:7260–7271, 2014.

[170] Y. Jin. Engineering plasmonic gold nanostructures and metamaterials for biosensing and nanomedicine. *Advanced Materials*, 24:5153–5165, 2012.

[171] S. E. Skrabalak, J. Chen, L. Au, X. Lu, X. Li, and Y. Xia. Gold nanocages for biomedical applications. *Advanced Materials*, 19:3177–3184, 2007.

[172] L. Au, D. Zheng, F. Zhou, Z. Y. Li, X. Li, and Y. Xia. A quantitative study on the photothermal effect of immuno gold nanocages targeted to breast cancer cells. *ACS Nano*, 2:1645–1652, 2008.

[173] B. N. Khlebtsov, E. V. Panfilova, G. S. Terentyuk, I. L. Maksimova, A. V. Ivanov, and N. G. Khlebtsov. Plasmonic nanopowders for photothermal therapy of tumors. *Langmuir*, 28:8994–9002, 2012.

[174] J. Chen, M. Yang, Q. Zhang, E. C. Cho, C. M. Cobley, C. Kim, C. Glaus, L. V. Wang, M. J. Welch, and Y. Xia. Gold nanocages: A novel class of multifunctional nanomaterials for theranostic applications. *Advanced Functional Materials*, 20: 3684–3694, 2010.

[175] J. Z. Zhang. Biomedical applications of shape-controlled plasmonic nanostructures: A case study of hollow gold nanospheres for photothermal ablation therapy of cancer. *Journal of Physical Chemistry Letters*, 1:686–695, 2010.

[176] J. S. Donner, S. A. Thompson, C. Alonso-Ortega, J. Morales, L. G. Rico, S. I. C. O. Santos, and R. Quidant. Imaging of plasmonic heating in a living organism. *ACS Nano*, 10:8666–8672, 2013.

[177] W. Xiong, R. Mazid, L. W. Yap, X. Li, and W. Cheng. Plasmonic caged gold nanorods for near-infrared light controlled drug delivery. *Nanoscale*, 6:14388–14393, 2014.

[178] T. Patino, U. Mahajan, R. Palankar, N. Medvedev, J. Walowski, M. Münzenberg, J. Mayerle, and M. Delcea. Multifunctional gold nanorods for selective plasmonic photothermal therapy in pancreatic cancer cells using ultra-short pulse near-infrared laser irradiation. *Nanoscale*, 7:5328–5337, 2015.

[179] F. J. García De Abajo. Optical excitations in electron microscopy. *Reviews of Modern Physics*, 82:209–275, 2010.

[180] M. Rycenga, C. M. Cobley, J. Zeng, W. Li, C. H. Moran, Q. Zhang, D. Qin, and Y. Xia. Controlling the synthesis and assembly of silver nanostructures for plasmonic applications. *Chemical Reviews*, 111:3669–3712, 2011.

[181] M. Hu, C. Novo, A. Funston, H. Wang, H. Staleva, S. Zou, P. Mulvaney, Y. Xia, and G. V. Hartland. Dark-field microscopy studies of single metal nanoparticles: understanding the factors that influence the linewidth of the localized surface plasmon resonance. *Journal of Materials Chemistry*, 18:1949–1960, 2008.

[182] J. Rodríguez-Fernández, C. Novo, V. Myroshnychenko, A. M. Funston, A. Sánchez-Iglesias, I. Pastoriza-Santos, J. Pérez-Juste, F. J. García de Abajo, L. M. Liz-Marzán, and P. Mulvaney. Spectroscopy, imaging, and modeling of individual gold decahedra. *Journal of Physical Chemistry C*, 113:18623–18631, 2009.

[183] M. G. Blaber, A. I. Henry, J. M. Bingham, G. C. Schatz, and R. P. Van Duyne. LSPR imaging of silver triangular nanoprisms: Correlating scattering with structure using electrodynamics for plasmon lifetime analysis. *Journal of Physical Chemistry C*, 116:393–403, 2012.

[184] U. C. Fischer and D. W. Pohl. Observation of Single-Particle Plasmons by Near-Field Optical Microscopy. *Physical Review Letters*, 62:458–462, 1989.

[185] K. Imura, T. Nagahara, and H. Okamoto. Near-field optical imaging of plasmon modes in gold nanorods. *The Journal of Chemical Physics*, 122:154701, 2005.

[186] M. Rang, A. C. Jones, Z. Fei, Z. Y. Li, B. J. Wiley, X. Younan, and M. B. Raschke. Optical Near-Field Mapping of Plasmonic Nanoprisms. *Nano Letters*, 8:3357–3363, 2008.

[187] R. Esteban, R. Vogelgesang, J. Dorfmuller, A. Dmitriev, C. Rockstuhl, C. Etrich, and K. Kern. Direct Near-Field Optical Imaging of Higher Order Plasmonic Resonances. *Nano Letters*, 8:3155–3159, 2008.

[188] N. Yamamoto, K. Araya, and F. J. García de Abajo. Photon emission from silver particles induced by a high-energy electron beam. *Physical Review B*, 64:1–9, 2001.

[189] N. Yamamoto, M. Nakano, and T. Suzuki. Light emission by surface plasmons on nanostructures of metal surfaces induced by high-energy electron beams. *Surface and Interface Analysis*, 38:1725–1730, 2006.

[190] K. A. Willets. Probing local electromagnetic field enhancements on the surface of plasmonic nanoparticles. *Progress in Surface Science*, 87:209–220, 2012.

[191] E. J. R. Vesseur, R. De Waele, M. Kuttge, and A. Polman. Direct observation of plasmonic modes in Au nanowires using high-resolution cathodoluminescence spectroscopy. *Nano Letters*, 7:2843–2846, 2007.

[192] P. Chaturvedi, K. H. Hsu, A. Kumar, K. H. Fung, J. C. Mabon, and N. X. Fang. Imaging of Plasmonic Modes of Silver Nanoparticles Using High-Resolution Cathodoluminescence Spectroscopy. *ACS nano*, 3:2965–2974, 2009.

[193] E. J. R. Vesseur, F. J. García de Abajo, and A. Polman. *Nano letters*, pages 3147–3150.

[194] P. Edwards, L. K. Jagadamma, and R. Martin. Cathodoluminescence hyperspectral imaging on the nanometre scale. *HSI*, 2:5–7, 2011.

[195] E. S. Barnard, T. Coenen, E. J. R. Vesseur, A. Polman, and M. L. Brongersma. Imaging the hidden modes of ultrathin plasmonic strip antennas by cathodoluminescence. *Nano Letters*, 11:4265–4269, 2011.

[196] E. J. R. Vesseur, J. Aizpurua, T. Coenen, A. Reyes-Coronado, P. E. Batson, and A. Polman. Plasmonic excitation and manipulation with an electron beam. *MRS Bulletin*, 37:752–760, 2012.

[197] P. Das and T. K. Chini. Spectroscopy and imaging of plasmonic modes over a single decahedron gold nanoparticle: A combined experimental and numerical study. *Journal of Physical Chemistry C*, 116:25969–25976, 2012.

[198] J. B. Lassiter, H. Sobhani, M. W. Knight, W. S. Mielczarek, P. Nordlander, and N. J. Halas. Designing and Deconstructing the Fano Lineshape in Plasmonic Nanoclusters. *Nano Letters*, 12:1058–1062, 2012.

[199] A. C. Atre, B. J. M. Brenny, T. Coenen, A. García-Etxarri, A. Polman, and J. A. Dionne. Nanoscale optical tomography with cathodoluminescence spectroscopy. *Nature Nanotechnology*, 10:429–436, 2015.

[200] R. Gómez-Medina, N. Yamamoto, M. Nakano, and F. J. García de Abajo. Mapping plasmons in nanoantennas via cathodoluminescence. *New Journal of Physics*, 10: 1–13, 2008.

[201] T. Suzuki and N. Yamamoto. Cathodoluminescent spectroscopic imaging of surface plasmon polaritons in a 1-dimensional plasmonic crystal. *Optics Express*, 17: 23664–23671, 2009.

[202] K. Takeuchi and N. Yamamoto. Visualization of surface plasmon polariton waves in two-dimensional plasmonic crystal by cathodoluminescence. *Optics Express*, 19: 12365–12374, 2011.

[203] A. Losquin, L. F. Zagonel, V. Myroshnychenko, B. Rodríguez-González, M. Tencé, L. Scarabelli, J. Förstner, L. M. Liz-Marzán, F. J. García de Abajo, O. Stéphan,

and M. Kociak. Unveiling Nanometer Scale Extinction and Scattering Phenomena through Combined Electron Energy Loss Spectroscopy and Cathodoluminescence Measurements. *Nano Letters*, 15:1229–1237, 2015.

[204] J. Nelayah, M. Kociak, O. Stéphan, F. J. García de Abajo, M. Tencé, L. Henrard, D. Taverna, I. Pastoriza-Santos, L. M. Liz-Marzán, and C. Colliex. Mapping surface plasmons on a single metallic nanoparticle. *Nature Physics*, 3:348–353, 2007.

[205] M. Bosman, V. J. Keast, M. Watanabe, A. I. Maaroof, and M. B. Cortie. Mapping surface plasmons at the nanometre scale with an electron beam. *Nanotechnology*, 18:165505, 2007.

[206] C. Jeanguillaume and C. Colliex. Spectrum-Image: The Next Step in EELS Digital Acquisition and Processing. *Ultramicroscopy*, 28:252–257, 1989.

[207] M. Kociak and F. J. García de Abajo. Nanoscale mapping of plasmons, photons, and excitons. *MRS Bulletin*, 37:39–46, 2012.

[208] A. L. Koh, K. Bao, I. Khan, W. E. Smith, G. Kothleitner, P. Nordlander, S. A. Maier, and D. W. Mccomb. Electron energy-loss spectroscopy (EELS) of surface plasmons in single silver nanoparticles and dimers: Influence of beam damage and mapping of dark modes. *ACS Nano*, 3:3015–3022, 2009.

[209] J. A. Scholl, A. L. Koh, and J. A. Dionne. Quantum plasmon resonances of individual metallic nanoparticles. *Nature*, 483:421–427, 2012.

[210] S. J. Barrow, D. Rossouw, A. M. Funston, G. A. Botton, and P. Mulvaney. Mapping bright and dark modes in gold nanoparticle chains using electron energy loss spectroscopy. *Nano Letters*, 14:3799–3808, 2014.

[211] M. W. Chu, V. Myroshnychenko, C. H. Chen, J. P. Deng, C. Y. Mou, and F. J. García de Abajo. Probing bright and dark surface-plasmon modes in individual and coupled noble metal nanoparticles using an electron beam. *Nano Letters*, 9: 399–404, 2009.

[212] O. Nicoletti, M. Wubs, N. A. Mortensen, W. Sigle, P. A. van Aken, and P. A. Midgley. Surface plasmon modes of a single silver nanorod: an electron energy loss study. *Optics Express*, 19:15371–15379, 2011.

[213] B. S. Guiton, V. Iberi, S. Li, D. N. Leonard, C. M. Parish, P. G. Kotula, M. Varela, G. C. Schatz, S. J. Pennycook, and J. P Camden. Correlated optical measurements and plasmon mapping of silver nanorods. *Nano Letters*, 11:3482–3488, 2011.

[214] D Rossouw, M Couillard, J Vickery, E Kumacheva, and G A Botton. Multipolar plasmonic resonances in silver nanowire antennas imaged with a subnanometer electron probe. *Nano Letters*, 11:1499–1504, 2011. ISSN 15306984. doi: 10.1021/nl200634w.

[215] Nicholas W Bigelow, Alex Vaschillo, Vighter Iberi, Jon P Camden, and David J Masiello. Characterization of the electron- and photon-driven plasmonic excitations of metal nanorods. *ACS Nano*, 6(8):7497–7504, 2012. ISSN 19360851. doi: 10.1021/nn302980u.

[216] Stefano Mazzucco, Nicolas Geuquet, Ye Jian, Odile Stephan, Willem Van Roy, Pol Van Dorpe, Luc Henrard, and Mathieu Kociak. Ultra local modification of surface plasmons properties in silver nanocubes Ultra local modification of surface plasmons properties in silver nanocubes. *Nano Letters*, 12:1288–1294, 2012.

[217] Bart Goris, Giulio Guzzinati, Cristina Fernández-López, Jorge Pérez-Juste, Luis M Liz-Marzán, Andreas Trügler, Ulrich Hohenester, Jo Verbeeck, Sara Bals, and Gustaaf Van Tendeloo. Plasmon mapping in Au@Ag nanocube assemblies. *Journal of Physical Chemistry C*, 118:15356–15362, 2014. ISSN 19327455. doi: 10.1021/jp502584t.

[218] Franz-Philipp Schmidt, Harald Ditlbacher, Ulrich Hohenester, Andreas Hohenau, Ferdinand Hofer, and Joachim R Krenn. Dark plasmonic breathing modes in silver nanodisks. *Nano Letters*, 12:5780–5783, 2012. ISSN 15306984. doi: 10.1021/nl3030938.

[219] Franz P Schmidt, Harald Ditlbacher, Ferdinand Hofer, Joachim R Krenn, and Ulrich Hohenester. Morphing a plasmonic nanodisk into a nanotriangle. *Nano Letters*, 14:4810–4815, 2014. ISSN 15306992. doi: 10.1021/nl502027r.

[220] B. Schaffer, W. Grogger, G. Kothleitner, and F. Hofer. Comparison of EFTEM and STEM EELS plasmon imaging of gold nanoparticles in a monochromated TEM. *Ultramicroscopy*, 110:1087–1093, 2010.

[221] Huigao Duan, Antonio Fernandez, Michel Bosman, Stefan a Maier, and Joel K W Yang. Nanoplasmonics : Classical down to the Nanometer Scale. *Nano Letters*, 12:1683–1689, 2012.

[222] S Mazzucco, O Stéphan, C Colliex, I Pastoriza-Santos, L M Liz-Marzan, F J Garcia de Abajo, and M Kociak. Spatially resolved measurements of plasmonic eigenstates in complex-shaped, asymmetric nanoparticles: gold nanostars. *The European Physical Journal Applied Physics*, 54:33512, 2011.

[223] V. Myroshnychenko, J. Nelayah, G. Adamo, N. Geuquet, J. Rodríguez-Fernández, I. Pastoriza-Santos, K. F. MacDonald, L. Henrard, L. M. Liz-Marzán, N. I. Zheludev, M. Kociak, and F. J. García De Abajo. Plasmon spectroscopy and imaging of individual gold nanodecahedra: A combined optical microscopy, cathodoluminescence, and electron energy-loss spectroscopy study. *Nano Letters*, 12:4172–4180, 2012.

[224] Ai Leen Koh, Antonio I Fernández-Domínguez, David W McComb, Stefan A Maier, and Joel K W Yang. High-resolution mapping of electron-beam-excited plasmon modes in lithographically defined gold nanostructures. *Nano Letters*, 11: 1323–1330, 2011. ISSN 15306984. doi: 10.1021/nl104410t.

[225] Kevin J Savage, Matthew M Hawkeye, Rubén Esteban, Andrei G Borisov, Javier Aizpurua, and Jeremy J Baumberg. Revealing the quantum regime in tunnelling plasmonics. *Nature*, 491:574–7, 2012.

[226] Yugang Sun, Brian T Mayers, and Younan Xia. Template-Engaged Replacement Reaction: A One-Step Approach to the Large-Scale Synthesis of Metal Nanostructures with Hollow Interiors. *Nano Letters*, 2:481–485, 2002. ISSN 15306984. doi: 10.1021/nl025531v.

[227] Y. Sun, B. Mayers, and Y. Xia. Metal Nanostructures with Hollow Interiors. *Advanced Materials*, 15:641–646, 2003.

[228] Qiang Zhang, Weiyang Li, Long Ping Wen, Jingyi Chen, and Younan Xia. Facile synthesis of Ag nanocubes of 30 to 70 nm in edge length with CF3COOAg as a precursor. *Chemistry - A European Journal*, 16:10234–10239, 2010. ISSN 09476539. doi: 10.1002/chem.201000341.

[229] Y. Sun, Y. Yin, B. T. Mayers, T. Herricks, and Y. Xia. Uniform Silver Nanowires Synthesis by Reducing AgNO3 with Ethylene Glycol in the Presence of Seeds and Poly (Vinyl Pyrrolidone). *Chemistry of Materials*, 14:4736–4745, 2002.

[230] B Fultz and J M Howe. *Transmission Electron Microscopy and Diffractometry of Materials*. Springer, 3rd edition edition, 2008.

[231] D B Williams and C B Carter. *Transmission Electron Microscopy: A Textbook for Materials Science*. Springer, 2nd edition edition, 2009.

[232] A I Kirkland and J L Hutchison, editors. *Nanocharacterization*. The Royal Society of Chemistry Publishing, 2007. ISBN 9780854042418.

[233] S J Pennycook and P D Nellist, editors. *Scanning Transmission Electron Microscopy: Imaging and Analysis*. Springer, 2011.

[234] R F Egerton. *Electron Energy-Loss Spectroscopy in the Electron Microscope.* Spgringer, 3rd edition edition, 2011.

[235] P D Nellist. The Principles of STEM Imaging. In S J Pennycook and P D Nellist, editors, *Scanning Transmission Electron Microscopy: Imaging and Analysis*, pages 91–115. Springer, 2011.

[236] A V Crewe. The physics of the high-resolution scanning microscope. *Reports on Progress in Physics*, 43:621–639, 1980.

[237] A V Crewe, J Wall, and J Langmore. Visibility of Single Atoms. *Science*, 168: 1338–1340, 1970.

[238] M M J Treacy, A Howie, and C J Wilson. Z contrast of platinum and palladium catalysts. *Philosophical Magazine A*, 38:569–585, 1978.

[239] A Howie. Image Contrast and Localized Signal Selection Techniques. *Journal of Microscopy*, 117:11–23, 1979.

[240] R Ishikawa, E Okunishi, H Sawada, Y Kondo, F Hosokawa, and E Abe. Direct imaging of hydrogen-atom columns in a crystal by annular bright-field electron microscopy. *Nature Materials*, 10:278–281, 2011.

[241] M de la Mata, C Magen, J Gazquez, M I B Utama, M Heiss, S Lopatin, F Furtmayr, C J Fernandez-Rojas, B Peng, J R Morante, R Rurali, M Eickhoff, A Fontcuberta i Morral, Q Xiong, and J Arbiol. Polarity Assignment in ZnTe, GaAs, ZnO, and GaN-AlN Nanowires from Direct Dumbbell Analysis. *Nano Letters*, 12:2579–2586, 2012.

[242] M Kociak, O Stephan, M G Walls, M Tence, and C Colliex. Spatially Resolved EELS: The Spectrum-Imaging Technique and Its Applications. In S J Pennycook and P D Nellist, editors, *Scanning Transmission Electron Microscopy: Imaging and Analysis*, pages 163–205. Springer, 2011.

[243] J A Hunt and D B Williams. Electron energy-loss spectrum-imaging. *Ultramicroscopy*, 38:47–73, 1991.

[244] Konrad Jarausch, Paul Thomas, Donovan N Leonard, Ray Twesten, and Christopher R Booth. Four-dimensional STEM-EELS: Enabling nano-scale chemical tomography. *Ultramicroscopy*, 109:326–337, 2009. ISSN 03043991. doi: 10.1016/j.ultramic.2008.12.012.

[245] Bart Goris, Stuart Turner, Sara Bals, and Gustaaf Van Tendeloo. Three-Dimensional Valency Mapping in Ceria Nanocrystals. *ACS Nano*, pages 10878–10884, 2014.

[246] Georg Haberfehlner, Angelina Orthacker, Mihaela Albu, Jiehua Li, and Gerald Kothleitner. Nanoscale voxel spectroscopy by simultaneous EELS and EDS tomography. *Nanoscale*, 6:14563–14569, 2014. ISSN 2040-3364. doi: 10.1039/C4NR04553J.

[247] Lluis Yedra, Alberto Eljarrat, Jose Manuel Rebled, Lluis Lopez-Conesa, Nico Dix, Florencio Sanchez, Sonia Estrade, and Francesca Peiro. EELS tomography in multiferroic nanocomposites: from spectrum images to the spectrum volume. *Nanoscale*, 6:6646–6650, 2014. ISSN 18426573. doi: 10.1039/b000000x.

[248] B. Schaffer, K. Riegler, G. Kothleitner, W. Grogger, and F. Hofer. Monochromated, spatially resolved electron energy-loss spectroscopic measurements of gold nanoparticles in the plasmon range. *Micron*, 40:269–273, 2009.

[249] K Kimoto, G Kothleitner, W Grogger, Y Matsui, and F Hofer. Advantages of a monochromator for bandgap measurements using electron energy-loss spectroscopy. *Micron*, 36:185–189, January 2005. URL `http://www.ncbi.nlm.nih.gov/pubmed/15629650`.

[250] R Erni and N D Browning. Valence electron energy-loss spectroscopy in monochromated scanning transmission electron microscopy. *Ultramicroscopy*, 104:176–192, 2005.

[251] D A Muller, T Sorsch, S Moccio, F H Baumann, and G Timp. The electronic structure at the atomic scale of ultrathin gate oxides. *Nature*, 399:758–761, 1999.

[252] C Mitterbauer, G Kothleitner, W Grogger, H Zandbergen, B Freitag, P Tiemeijer, and F Hofer. Electron energy-loss near-edge structures of 3d transition metal oxides recorded at high-energy resolution. *Ultramicroscopy*, 96:469–480, September 2003. ISSN 0304-3991.

[253] W. Grogger, F. Hofer, G. Kothleitner, and B. Schaffer. An introduction to high-resolution EELS in transmission electron microscopy. *Topics in Catalysis*, 50: 200–207, 2008.

[254] M. Bosman, E. Ye, S. F. Tan, C. A. Nijhuis, J. K. W. Yang, R. Marty, A. Mlayah, A. Arbouet, C. Girard, and M. Y. Han. Surface plasmon damping quantified with an electron nanoprobe. *Scientific Reports*, 3:1312, 2013.

[255] A Gloter, A Douiri, M Tencé, and C Colliex. Improving energy resolution of EELS spectra: An alternative to the monochromator solution. *Ultramicroscopy*, 96:385–400, 2003. ISSN 03043991. doi: 10.1016/S0304-3991(03)00103-7.

[256] S Lazar, G A Botton, and H W Zandbergen. Enhancement of resolution in core-loss and low-loss spectroscopy in a monochromated microscope. *Ultramicroscopy*, 106:1091–1103, 2006.

[257] Edson P Bellido, David Rossouw, and Gianluigi A Botton. Toward 10 meV Electron Energy-Loss Spectroscopy Resolution for Plasmonics. *Microscopy and Microanalysis*, 20:767–78, 2014.

[258] O L Krivanek, J P Ursin, N J Bacon, G J Corbin, N Dellby, P Hrncirik, M F Murfitt, C S Own, and Z S Szilagyi. High-energy-resolution monochromator for aberration-corrected scanning transmission electron microscopy/electron energy-loss spectroscopy. *Philosophical Transactions of the Royal Society A*, 367:3683–3697, 2009. ISSN 1364-503X. doi: 10.1098/rsta.2009.0087.

[259] O. L. Krivanek, T. C. Lovejoy, N. Dellby, T. Aoki, R. W. Carpenter, P. Rez, E. Soignard, J. Zhu, P. E. Batson, M. J. Lagos, R. F. Egerton, and P. A. Crozier. Vibrational spectroscopy in the electron microscope. *Nature*, 514:209–212, 2014.

[260] P. A. Midgley, E. P. W. Ward, A. B. Hungria, and J. M. Thomas. Nanotomography in the chemical, biological and materials sciences. *Chemical Society Reviews*, 36: 1477–1494, 2007.

[261] Paul A Midgley and Rafal E Dunin-Borkowski. Electron tomography and holography in materials science. *Nature materials*, 8:271–280, April 2009. doi: 10.1038/nmat2406.

[262] Z. Saghi and P. A. Midgley. Electron Tomography in the (S)TEM: From Nanoscale Morphological Analysis to 3D Atomic Imaging. *Annual Review of Materials Research*, 42:59–79, 2012.

[263] Bart Goris, Lakshminarayana Polavarapu, Sara Bals, Gustaaf Van Tendeloo, and Luis M Liz-Marzán. Monitoring galvanic replacement through three-dimensional morphological and chemical mapping. *Nano Letters*, 14:3220–3226, 2014. ISSN 15306992. doi: 10.1021/nl500593j.

[264] M H Gass, K K K Koziol, A H Windle, and P A Midgley. Four-Dimensional Spectral Tomography of Carbonaceous Nanocomposites. *Nano Letters*, 6:376–379, 2006.

[265] L. Yedra, A. Eljarrat, R. Arenal, E. Pellicer, M. Cabo, A. López-Ortega, M. Estrader, J. Sort, M. D. Baró, S. Estradé, and F. Peiró. EEL spectroscopic tomography: towards a new dimension in nanomaterials analysis. *Ultramicroscopy*, 122:12–18, 2012.

[266] Lluís Yedra Cardona. *Towards a new dimension in analytical TEM : EELS , Tomography and the Spectrum Volume.* PhD thesis, Universitat de Barcelona, 2013.

[267] Anton Hörl, Andreas Trügler, and Ulrich Hohenester. Tomography of particle plasmon fields from electron energy loss spectroscopy. *Physical Review Letters*, 111(August):1–5, 2013. ISSN 00319007. doi: 10.1103/PhysRevLett.111.076801.

[268] F. de la Peña, P. Burdet, M. Sarahan, M. Nord, T. Ostasevicius, J. Taillon, A. Eljarrat, S. Mazzucco, V. T. Fauske, G. Donval, L. F. Zagonel, I. Iyengar, and M. Walls. Hyperspy 0.8, April 2015.

[269] P. Trebbia and N. Bonnet. EELS elemental mapping with unconventional methods I . Theoretical basis: image analysis with multivariate statistics and entropy concepts. *Ultramicroscopy*, 34:165–178, 1990.

[270] M Bosman, M Watanabe, D T L Alexander, and V J Keast. Mapping chemical and bonding information using multivariate analysis of electron energy-loss spectrum images. *Ultramicroscopy*, 106:1024–1032, 2006. ISSN 03043991. doi: 10.1016/j.ultramic.2006.04.016.

[271] Noël Bonnet and Danielle Nuzillard. Independent component analysis: A new possibility for analysing series of electron energy loss spectra. *Ultramicroscopy*, 102:327–337, 2005. ISSN 03043991. doi: 10.1016/j.ultramic.2004.11.003.

[272] F De La Peña, N Barrett, L F Zagonel, M Walls, and O Renault. Full field chemical imaging of buried native sub-oxide layers on doped silicon patterns. *Surface Science*, 604(19-20):1628–1636, 2010. ISSN 00396028. doi: 10.1016/j.susc.2010.06.006.

[273] F de la Peña, M H Berger, J F Hochepied, F Dynys, O Stephan, and M Walls. Mapping titanium and tin oxide phases using EELS: An application of independent component analysis. *Ultramicroscopy*, 111:169–176, 2011. ISSN 03043991. doi: 10.1016/j.ultramic.2010.10.001.

[274] Nicolas Dobigeon and Nathalie Brun. Spectral mixture analysis of EELS spectrum-images. *Ultramicroscopy*, 120:25–34, 2012. ISSN 03043991. doi: 10.1016/j.ultramic.2012.05.006.

[275] José M P Nascimento and J. Bioucas-Dias. Vertex component analysis: a fast algorithm to unmix hyperspectral data. *IEEE Transactions on Geoscience and Remote Sensing*, 43:898–910, 2005.

[276] N. Dobigeon, S. Moussaoui, M. Coulon, J. Y. Tourneret, and A. O. Hero. Joint Bayesian Endmember Extraction and Linear Unmixing for Hyperspectral Imagery. *IEEE Transactions on Signal Processing*, 57:4355–4368, 2009.

[277] M Duchamp, M Lachmann, C B Boothroyd, A Kovács, F J Haug, C Ballif, and R E Dunin-Borkowski. Compositional study of defects in microcrystalline silicon solar cells using spectral decomposition in the scanning transmission electron microscope. *Applied Physics Letters*, 102:2013–2016, 2013. ISSN 00036951. doi: 10.1063/1.4800569.

[278] C. B. Boothroyd, M. S. Moreno, M. Duchamp, A. Kovács, N. Monge, G. M. Morales, C. A. Barbero, and R. E. Dunin-Borkowski. Ultramicroscopy Atomic resolution imaging and spectroscopy of barium atoms and functional groups on graphene oxide. *Ultramicroscopy*, 145:66–73, 2014.

[279] J. M. P. Nascimento and J. M. B. Dias. Does independent component analysis play a role in unmixing hyperspectral data? *IEEE Transactions on Geoscience and Remote Sensing*, 43:175–187, 2005.

[280] F. J. Garcia de Abajo and A. Howie. Relativistic Electron Energy Loss and Electron-Induced Photon Emission in Inhomogeneous Dielectrics. *Physical Review Letters*, 80:5180–5183, 1998.

[281] F Javier García de Abajo and A Howie. Retarded field calculation of electron energy loss in inhomogeneous dielectrics. *Physical Review B*, 65(11):1–17, 2002. ISSN 0163-1829.

[282] U. Hohenester and A. Trügler. MNPBEM - A Matlab toolbox for the simulation of plasmonic nanoparticles. *Computer Physics Communications*, 183:370–381, 2012.

[283] B. T. Draine and P. J. Flatau. Discrete-dipole approximation for scattering calculations. *Journal of Optical Society of America A*, 11:1491–1499, 1994.

[284] Nicolas Geuquet and Luc Henrard. EELS and optical response of a noble metal nanoparticle in the frame of a discrete dipole approximation. *Ultramicroscopy*, 110 (8):1075–1080, 2010. ISSN 03043991. doi: 10.1016/j.ultramic.2010.01.013.

[285] A. J. Ward and J. B. Pendry. A program for calculating photonic band structures , Greens functions and transmission/reflection coefficients using a non-orthogonal FDTD method. *Computer Physics Communications*, 128:590–621, 2000.

[286] Ulrich Hohenester, Harald Ditlbacher, and Joachim R Krenn. Electron-energy-loss spectra of plasmonic nanoparticles. *Physical Review Letters*, 103(September):1–4, 2009. ISSN 00319007. doi: 10.1103/PhysRevLett.103.106801.

[287] Benito Rodriguez-Gonzalez, Farah Attouchi, M Fernanda Cardinal, Victor Myroshnychenko, Odile Stephan, F Javier Garcia de Abajo, Luis M Liz-Marzan, and Mathieu Kociak. Surface Plasmon Mapping of Dumbbell-Shaped Gold Nanorods: The Effect of Silver Coating. *Langmuir*, 28:9063–9070, 2012.

[288] M. K. Krug, M. Reisecker, A. Hohenau, H. Ditlbacher, A. Trügler, U. Hohenester, and J. R. Krenn. Probing plasmonic breathing modes optically. *Applied Physics Letters*, 105:171103, 2014.

[289] M. Kociak and O. Stéphan. Mapping plasmons at the nanometer scale in an electron microscope. *Chemical Society Reviews*, 43:3865–83, 2014.

[290] William L Barnes, Alain Dereux, and Thomas W Ebbesen. Surface plasmon subwavelength optics. *Nature*, 424(August):824–830, 2003. ISSN 0028-0836. doi: 10.1038/nature01937.

[291] J. A. Schuller, E. S. Barnard, W. Cai, Y. C. Jun, J. S. White, and M. L. Brongersma. Plasmonics for extreme light concentration and manipulation. *Nature Materials*, 9:193–204, 2010.

[292] Jeffrey M McMahon, Yingmin Wang, Leif J Sherry, Richard P Van Duyne, Laurence D Marks, Stephen K Gray, and George C Schatz. Correlating the Structure, Optical Spectra, and Electrodynamics of Single Silver Nanocubes. *Journal of Physical Chemistry C*, 113(1):2731–2735, 2009. ISSN 19327447. doi: 10.1021/jp8098736.

[293] M A Mahmoud and M A El-Sayed. Metallic double shell hollow nanocages: The challenges of their synthetic techniques. *Langmuir*, 28:4051–4059, 2012. ISSN 07437463. doi: 10.1021/la203982h.

[294] M Kociak, O Stéphan, L Henrard, V Charbois, A Rothschild, R Tenne, and C Colliex. Experimental evidence of surface-plasmon coupling in anisotropic hollow nanoparticles. *Physical review letters*, 87:075501, 2001. ISSN 0031-9007. doi: 10.1103/PhysRevLett.87.075501.

[295] Eudald Casals, Tobias Pfaller, Albert Duschl, Gertie Janneke Oostingh, and Victor Puntes. Time evolution of the nanoparticle protein corona. *ACS Nano*, 4:3623–3632, 2010. ISSN 19360851. doi: 10.1021/nn901372t.

[296] Eudald Casals, Tobias Pfaller, Albert Duschl, Gertie J Oostingh, and Víctor F Puntes. Hardening of the nanoparticle-protein corona in metal (Au, Ag) and oxide (Fe3O4, CoO, and CeO2) nanoparticles. *Small*, 7:3479–3486, 2011. ISSN 1613-6829. doi: 10.1002/smll.201101511.

[297] Marco P Monopoli, Christoffer Aberg, Anna Salvati, and Kenneth A Dawson. Biomolecular coronas provide the biological identity of nanosized materials. *Nature nanotechnology*, 7:779–786, 2012. ISSN 1748-3395. doi: 10.1038/nnano.2012.207.

[298] Fan Xia, Xiaolei Zuo, Renqiang Yang, Yi Xiao, Di Kang, Alexis Vallée-Bélisle, Xiong Gong, Jonathan D Yuen, Ben B Y Hsu, Alan J Heeger, and Kevin W Plaxco. Colorimetric detection of DNA, small molecules, proteins, and ions using unmodified gold nanoparticles and conjugated polyelectrolytes. *Proceedings of the National Academy of Sciences of the United States of America*, 107:10837–10841, 2010. ISSN 0027-8424. doi: 10.1073/pnas.1005632107.

[299] J. Patarroyo, N. G. Bastus, A. Genc, J. Arbiol, and V. Puntes. A General Strategy for the Production of (Ag/Au) Multidomain Bimetallic and (Ag/Au/Pt or Pd) Trimetallic Noble Metal Nanotubes. *Submitted*, 2015.

[300] Ina Alber, Wilfried Sigle, Sven Müller, Reinhard Neumann, Oliver Picht, Markus Rauber, Peter A Van Aken, and Maria Eugenia Toimil-Molares. Visualization of multipolar longitudinal and transversal surface plasmon modes in nanowire dimers. *ACS Nano*, 5(12):9845–9853, 2011. ISSN 19360851. doi: 10.1021/nn2035044.

[301] Mark W Knight, Heidar Sobhani, Peter Nordlander, and Naomi J Halas. Photodetection with active optical nanoantennas. *Science*, 332:702–704, 2011.

[302] A. Alu and N. Engheta. Tuning the scattering response of optical nanoantennas with nanocircuit loads. *Nature Photonics*, 2:307–310, 2008.

[303] A. L. Falk, F. H. L. Koppens, C. L. Yu, K. Kang, N. de Leon Snapp, A. V. Akimov, M. H. Jo, M. D. Lukin, and H. Park. Near-field electrical detection of optical plasmons and single-plasmon sources. *Nature Physics*, 5:475–479, 2009.

[304] Kevin C Y Huang, Min-Kyo Seo, Tomas Sarmiento, Yijie Huo, James S Harris, and Mark L Brongersma. Electrically driven subwavelength optical nanocircuits. *Nature Photonics*, 8:244–249, February 2014. ISSN 1749-4885.

[305] Jens Dorfmüller, Ralf Vogelgesang, Worawut Khunsin, Carsten Rockstuhl, Christoph Etrich, and Klaus Kern. Plasmonic nanowire antennas: Experiment, simulation, and theory. *Nano Letters*, 10:3596–3603, 2010. ISSN 15306984. doi: 10.1021/nl101921y.

[306] Ning Lu, Jinguo Wang, Shuifen Xie, Jacob Brink, Kevin Mcilwrath, Younan Xia, and Moon J Kim. Aberration Corrected Electron Microscopy Study of Bimetallic Pd Pt Nanocrystal: Core Shell Cubic and Core Frame Concave Structures. *The Journal of Physical Chemistry C*, 118:28876–28882, 2014.

[307] Kyle D Osberg, Nadine Harris, Tuncay Ozel, Jessie C Ku, George C Schatz, and Chad A Mirkin. Systematic Study of Antibonding Modes in Gold Nanorod Dimers and Trimers. *Nano Letters*, 12:6949–6954, 2014.